Setup of a Drift Tube Muon Tracker and Calibration of Muon Tracking in Borexino

Dissertation

zur Erlangung des Doktorgrades

des Department Physik

der Universität Hamburg

vorgelegt von

Daniel Bick

aus Hannover

Hamburg

2011

Gutachter der Dissertation:	Prof. Dr. Caren Hagner Prof. Dr. Walter Schmidt-Parzefall
Gutachter der Dispuation:	Prof. Dr. Caren Hagner JProf. Dr. Alessandro Mirizzi
Datum der Disputation:	6. April 2011
Vorsitzender des Prüfungsausschusses:	Dr. Georg Steinbrück
Vorsitzender des Promotionsausschusses:	Prof. Dr. Joachim Bartels
Dekan der MIN Fakultät:	Prof. Dr. Heinrich Graener

Abstract

In this work the setup and commissioning of a drift tube based 3D muon tracking detector are described and its use for the solar neutrino experiment Borexino is presented. After a brief introduction to neutrino physics, the general layout of the detector is presented. It is followed by the description of the reconstruction and calibration algorithms. The performance of the muon tracker is presented and results from the commissioning in Hamburg are shown. The detector is currently operated in the LNGS underground laboratory in Italy at the Borexino experiment. After an introduction to Borexino, the modifications of the muon tracker for its setup at LNGS are described. The setup is used as a reference system to determine the resolution of the Borexino muon tracking which is essential for the tagging of cosmogenic induced ^{11}C background. Finally, first results are presented.

Zusammenfassung

Diese Arbeit beschreibt den Aufbau und die Inbetriebnahme eines driftröhrenbasierten 3D Myonenspurdetektors sowie seinen Einsatz beim solaren Neutrino Experiment Borexino. Nach einer kurzen Einführung in die Neutrinophysik wird der Aufbau des Detektors präsentiert. Anschließend werden die Rekonstruktions- und Kalibrationsalgorithmen vorgestellt. Die wesentlichen Eigenschaften des Myonendetektors, sowie Ergebnisse der Inbetriebnahme in Hamburg werden gezeigt. Der Detektor wird zur Zeit am LNGS Untergrundlabor in Italien beim Borexino Experiment eingesetzt. Nach einer kurzen Einführung in das Borexino Experiment werden die Änderungen am Detektor für den Einsatz am LNGS gezeigt. Der Aufbau wird als Referenzsystem zur Bestimmung der Auflösung der Borexino Myonenspurrekonstruktion verwendet, die zur Identifizierung des kosmogen induzierten ^{11}C Untergrundes essentiell ist. Abschließend werden erste Ergebnisse präsentiert.

Contents

Chapter 1

Introduction

During the last decades exciting discoveries concerning neutrinos have been made. With the experimental evidence of neutrino oscillations, the solar neutrino puzzle could finally be solved. This proved at the same time, that neutrinos have mass. A precise determination of the neutrino mixing parameters is currently being approached by several experiments.

Spectroscopic measurements of solar neutrino fluxes allow for an energy dependent study of the neutrino survival probability. Furthermore, a spectral analysis of solar neutrinos helps to understand the processes in the Sun and the effect of matter on neutrino oscillations. Neutrino detection in water Čerenkov detectors has so far limited spectroscopic measurements of neutrino fluxes to energies above approximately 3 to 5 MeV, and radio chemical experiments can only perform an energy integrated measurement. During the last years, physicists succeeded in the spectral measurement of neutrinos using liquid scintillator detectors. Given a high radio purity, neutrinos can in principle be observed without an energy threshold through elastic scattering processes on electrons within the scintillator. In reality however, the detection is limited to energies above 156 keV, the end point energy of decays of ^{14}C intrinsic to organic scintillators. Events from the decay of radioactive contaminants have to be limited by a high radio purity. One particular challenge are background events induced by cosmic muons. High energy cosmic muons can produce long living radioactive isotopes through nuclear spallation in the scintillator. The decay of such an isotope cannot be related to the incident muon and is thus often referred to as uncorrelated cosmogenic background. Among other cosmogenic induced isotopes, ^{11}C is the most prominent example. It has a half-life of approximately 20 minutes and decays via a β^+ with a decay energy of 1982.2 keV. Unfortunately, these events can mimic neutrino interactions. Decays from ^{11}C cover the energy region where the transition from vacuum to matter dominated oscillation occurs. The determination of the oscillation survival probability in this regime allows to discriminate different models for matter enhanced oscillations and is thus very sensitive to test physics beyond the standard model. Therefore it is essential to understand well the impact of cosmic muons on the experiment.

The liquid scintillator experiment Borexino recently succeeded in a spectroscopic measurement of solar ^{7}Be and ^{8}B neutrinos. The goal to observe also CNO and *pep* neutrinos is hindered mainly by the ^{11}C cosmogenic induced background. A successful identification and tracking of cosmic muons producing ^{11}C isotopes is

essential for vetoing these events.

Cosmic muons created in the atmosphere have the ability to penetrate the Earth to significant depths. They are hard to shield and a disturbance to measurements with most particle detectors. Placing the experiment underground helps to reduce the muon flux. However, even at a depth of a few thousand meters water equivalent cosmic muons still cannot be neglected. It is thus of importance to effectively tag these muons to be able to veto their induced signals.

To veto events from cosmogenic induced nuclei, the intersection of a cylinder around the incident muon track and a sphere around the position of the capture of the knocked out neutron are taken off the fiducial volume for a few half-lives of the ^{11}C. A good resolution of the muon tracking thus is a key feature to prevent large fractions of the detector being blinded by this method. In Borexino, muon tracks are reconstructed by investigating the arrival time patterns at the PMTs. For a precise determination of the tracking resolution, the true muon track coordinates have to be known.

The compact muon tracker (CMT) presented in this work is capable of a three dimensional reconstruction of muon tracks with a spatial resolution of better than 300 µm and an angular resolution of approximately 5 mrad. It is based on the drift tube technology developed for the Precision Tracker (PT) of the OPERA experiment. Whereas the PT only reconstructs 2D projections of muon tracks, the CMT has been modified so that a three dimensional tracking is possible. After a commissioning in Hamburg it is now operated at the Borexino experiment at the LNGS underground laboratory in the Abruzzo region in Italy. Although the CMT only covers a small fraction of the Borexino detector, muon tracks reconstructed in the detector can be used as a reference sample for the internal Borexino muon tracking. Thus, the CMT data can be used to determine the resolution of the internal Borexino muon tracking. Comparing the tracks as reconstructed by the CMT with high precision to the Borexino reconstruction can help to identify possible systematic errors of the latter, and to improve its performance and hence the ^{11}C tagging.

Within this thesis, the setup and commissioning of the CMT were performed and are described here. Its application to the Borexino experiment is presented and the resolution of the Borexino muon tracking is determined.

Following the introduction, Chapter 2 of this work deals with the physics of neutrinos. After a brief overview of the history of neutrino physics in Section 2.1, the basics of neutrino oscillations are presented. An emphasis on solar neutrinos in particular is given in Section 2.3, followed by a look at other neutrino sources and open questions in neutrino physics.

The general setup of the CMT is described in Chapter 3. After an introduction to the working principle of drift tubes, the setup of the individual components such as the drift tube modules, the gas supply, and the electronics is described. This is followed by a description of the data taking procedure. The CMT data are processed with the software package `cmtrack` which was developed within this thesis and is then introduced. The reconstruction algorithms are described in detail. Finally, the calibration and alignment of the detector is introduced and the first commissioning of the detector in Hamburg is presented.

Chapter 4 gives an overview of the Borexino experiment. The detection method for neutrinos in liquid scintillators is described and the general setup of the Borexino

detector is introduced. This is followed by a look at the most relevant background sources in Borexino. Finally, the results obtained recently are presented.

The application of the CMT at the Borexino experiment is then presented in Chapter 5. First, the modifications done for a setup at Gran Sasso are described. The results of the commissioning phase are then reported. It is followed by a look at muon tracks that have passed both the CMT and Borexino. A combined analysis of these events is done yielding a measure for the resolution of the Borexino muon tracking. A similar analysis is then introduced, using tracks from rock muons reconstructed by the neighboring OPERA experiment that have also crossed Borexino.

Finally, a summary and outlook are given in Chapter 6.

Chapter 2

Neutrinos

The standard model of particle physics comprises only a few elementary particles: six quarks and six leptons as well as their anti particles plus the gauge bosons mediating the forces between them. Out of these particles, the neutrinos are of a most interesting kind. They account for three of the leptons (ν_e, ν_μ, ν_τ), they are uncharged, each being a partner of one of the remaining—charged—leptons (e^-, μ^-, τ^-). Originally assumed to be massless, it has recently been shown that neutrinos have a tiny mass indeed. Although the standard model assumes a strict lepton number conservation within each family, neutrinos have the ability to change into one another when traveling distances. This already shows that neutrinos offer a large potential for physics beyond the standard model. Neutrinos hardly interact with matter, making it hard to detect them on the one hand, but on the other hand also offering a great opportunity to use them as messenger particles. Their ability to reach us from any source without any significant disturbance on their way makes it possible to use them as a probe of whatever they originate from.

The first section of this chapter will give a brief introduction to the history of neutrino physics. This will be followed by a look at neutrino oscillations and the influence of matter on this effect. A particular look on solar neutrinos is then presented, followed by an overview of other neutrinos sources.

2.1 A Brief History of Neutrino Physics

The neutrino was first postulated by Wolfgang Pauli in 1930 [1]. To explain the continuous energy spectrum of electrons in β decays as well as to maintain angular momentum conservation, he assumed a neutral, invisible particle nowadays known as the electron neutrino ν_e to take part in the process.

It was not until 1956 that the neutrino could actually be observed by Frederick Reines and Clyde L. Cowan in an experiment called "Project Poltergeist" [2]. At the Savannah River reactor in the US state of South Carolina, they succeeded to observe the inverse beta decay:

$$\bar{\nu}_e + p \rightarrow e^+ + n.$$

Reines and Cowan arranged to detect the γ-emission following the capture of the neutron in a nucleus, which together with two photons from the annihilation of the positron with an electron gives a distinct signature for the process.

In 1962 Leon M. Lederman, Melvin Schwartz and Jack Steinberger showed that more than one type of neutrino exists. By studying the decay of pions, they observed that the emitted neutrinos only react with muons but not with electrons. Hence the neutrino involved had to be different from the one known from β decays—the muon-neutrino ν_μ was discovered [3]. After the discovery of a third charged lepton (the τ) in 1975 at SLAC[1] [4], it was also expected to have an associated neutrino. The ν_τ was experimentally discovered by the DONUT[2] experiment at Fermilab in 2000 [5].

Today, the standard model knows these three kinds of neutrinos and their corresponding anti particles. They are all fermions and have no charge. Each neutrino can be paired with its corresponding charged lepton, leading to three families:

$$\begin{pmatrix}\nu_e\\ e^-\end{pmatrix} \qquad \begin{pmatrix}\nu_\mu\\ \mu^-\end{pmatrix} \qquad \begin{pmatrix}\nu_\tau\\ \tau^-\end{pmatrix}.$$

The standard model assumes the neutrinos to be of no mass and electrical charge. They only interact in weak processes and are left handed[3].

The number of light[4] neutrino types[5] N_ν has been determined by various experiments. The most precise measurements come from studies of Z production in e^+e^- collisions at LEP[6] at CERN[7]. In the reaction $e^+e^- \to Z^0 \to f\bar{f}$, where f is an elementary fermion, the total decay width as well as the partial widths for charged leptonic and hadronic events can be measured, hence the width for the *invisible* neutrinos can be determined. By comparing this to the theoretical expected decay width of neutrinos, one can calculate N_ν. The process has been measured by the LEP experiments ALEPH, DELPHI, L3 and OPAL which have obtained a combined result of $N_\nu = 2.984 \pm 0.008$ [6], being in good agreement with the predictions.

The most intense source for neutrinos on Earth is our Sun. The flux of neutrinos originating from the thermonuclear processes in the Sun's core is of the order of $6 \times 10^{10}\,\mathrm{cm^{-2}s^{-1}}$. The Sun as a neutrino source will be discussed in more detail in Section 2.3. Attempts to measure the flux of solar neutrinos started with the Homestake experiment in 1968 [7]. The experiment could perform an energy integrated measurement of the solar neutrino spectrum by using a radio chemical based setup. Neutrino detection was done via the capture of the neutrino in the process $^{37}\mathrm{Cl} + \nu_e \to {}^{37}\mathrm{Ar} + e^-$. The Argon was then removed from the target and its decays were observed in a small proportional counter. The measured flux, however, was only about one third of what was expected from the standard solar model. Gallium based experiments like Gallex [8], GNO [9] and SAGE [10] confirmed this discrepancy in the solar neutrino flux referred to as the solar neutrino puzzle. In 1989, the Kamiokande experiment succeeded in a real time solar neutrino observation detecting electrons from $\nu_e - e^-$ scattering in a large water Čerenkov detector [11]. Being able to determine also the directional information of the incoming neutrino allowed to significantly improve the separation of solar neutrinos from background.

[1] SLAC - Stanford Linear Accelerator Center

[2] DONUT - Direct Observation of Nu Tau

[3] In the case of anti neutrinos right handed.

[4] Neutrinos with a mass smaller than half the Z^0-mass $m_Z = 91.187\,\mathrm{GeV}$

[5] Disregarding the possibility of *sterile* neutrinos

[6] LEP - Large Electron-Positron Collider

[7] CERN - Conseil Européen pour la Recherche Nucléaire - European Organization for Nuclear Research

However, it did not yet deliver an answer to the solar neutrino puzzle but rather confirmed the lower than expected ν_e flux.

With the experimental observation of neutrino oscillations (cf. Section 2.2) in 1998 by the Super-Kamiokande experiment [12] and the confirmation for solar neutrinos in particular by the SNO experiment in 2001 [13], the solar neutrino puzzle could finally be resolved. The latter experiment succeeded in measuring both the solar ν_e flux in CC reactions as well as the fluxes from all neutrino types through NC processes. Whereas the ν_e flux was again only about one third of the expected, the total flux was in agreement with the predictions. The answer to the solar neutrino puzzle was found: some of the originally electron type neutrinos change their flavor on the way from the Sun to Earth and are thus not detected by experiments mereley sensitive to ν_e.

The evidence of neutrino oscillations also showed that neutrinos have a non vanishing mass after all. However, it does not give an answer to the absolute neutrinos masses—only the squared mass splittings can be determined, leaving also the question of the mass hierarchy mostly unanswered. The determination of the absolute (electron type) neutrino mass has been addressed by several experiments, e.g. by investigating the endpoint energy of the β decay of tritium. Both the Mainz [14] and the Troitsk [15] experiments found an upper limit slightly above 2 eV. Currently, the KATRIN [16] experiment is being built aiming at a sensitivity of 0.2 eV.

Neutrinos are the only leptons with no charge. This leaves the possibility for the neutrino to be its own anti particle. This scenario was first suggested by E. Majorana in 1937 [17] and such a neutrino would be called a Majorana particle. If neutrinos are different from their anti particles they are called Dirac particles. The assumption of neutrinos being their own anti particles leads to some interesting consequences like the neutrinoless double-beta decay ($0\nu\beta\beta$). In an ordinary (two neutrino) double-beta decay, two electrons and two neutrinos are emitted. If the neutrino is indeed a Majorana particle, the two neutrinos could annihilate, thus only two electrons would be emitted. Several experiments now search for the neutrinoless double-beta decay (e.g. [18–20]).

2.2 Neutrino Mixing and Oscillations

Neutrino oscillations have been experimentally verified by various experiments during the last decade. The existence of neutrino oscillations proofs that neutrinos have a mass, after all. Also, lepton number conservation within each lepton generation is broken. This section gives a short introduction to neutrino oscillations. First, the general case in vacuum is considered. It is followed by a look at the influence of matter to neutrino oscillations.

2.2.1 Oscillations in Vacuum

In case of a non vanishing neutrino mass, the neutrino's mass eigenstates $|\nu_i\rangle$ do not necessarily have to be the same as the weak eigenstates $|\nu_\alpha\rangle$. A neutrino $|\nu_\alpha\rangle$ of flavor α, where $\alpha = e, \mu$ or τ can then be described by a superposition of the mass

eigenstates $|\nu_i\rangle$:

$$|\nu_\alpha\rangle = \sum_i U^*_{\alpha i} |\nu_i\rangle, \tag{2.1}$$

where U is the unitary leptonic mixing matrix, often called the Maki-Nakagawa-Sakata or Pontecorvo-Maki-Nakagawa-Sakata Matrix after the physicists who first introduced the idea of neutrino mixing in the late 1950s and early 1960s [21–23]. If the neutrino mass eigenstates are different from each other, quantum mechanics leads to the possibility of flavor changes for neutrinos traveling in vacuum or matter. A neutrino only interacts through the weak force, thus it is always created as a weak or flavor eigenstate. For the evolution of the neutrino, the superposition of its mass eigenstates has to be considered. If the neutrino then interacts with matter again the flavor eigenstate determines the type of reaction. The probability of a change of flavor α into β for a neutrino withe energy E_ν traveling a distance L in vacuum can be calculated by:

$$P_{\nu_\alpha \to \nu_\beta} = \left| \left\langle \nu_\beta \left| e^{-i \frac{m_i^2}{2E_\nu} L} \right| \nu_\alpha \right\rangle \right|^2,$$

where m_i is the mass of the eigenstate $|\nu_i\rangle$. While there are three known flavor eigenstates of the neutrino, the number of different mass eigenstates can in principle exceed this number (leading to the possibility of *sterile* neutrinos). In the case of just three mass eigenstates, the mixing matrix can be parametrized as a 3×3 matrix with three mixing angles θ_{ij} and one phase δ. In the case of neutrinos being their own anti particles, two additional Majorana phases α_1 and α_2 have to be included in the mixing matrix. The mixing matrix U can thus be parametrized as follows:

$$\begin{aligned} U = &\begin{pmatrix} 1 & 0 & 0 \\ 0 & \cos\theta_{23} & \sin\theta_{23} \\ 0 & -\sin\theta_{23} & \cos\theta_{23} \end{pmatrix} \times \begin{pmatrix} \cos\theta_{13} & 0 & \sin\theta_{13} e^{-i\delta} \\ 0 & 1 & 0 \\ -\sin\theta_{13} e^{i\delta} & 0 & \cos\theta_{13} \end{pmatrix} \\ &\times \begin{pmatrix} \cos\theta_{12} & \sin\theta_{12} & 0 \\ -\sin\theta_{12} & \cos\theta_{12} & 0 \\ 0 & 0 & 1 \end{pmatrix} \times \begin{pmatrix} e^{i\alpha_1/2} & 0 & 0 \\ 0 & e^{i\alpha_2/2} & 0 \\ 0 & 0 & 1 \end{pmatrix}. \end{aligned}$$

The mixing angles θ_{23} [24–28] and θ_{12} [29–31] have been measured by various experiments. For the remaining mixing angle θ_{13}, an upper limit only could be determined so far [32]. The complex phase δ can be responsible for CP violation in the lepton sector. Using the notation above implies that CP violation in the lepton sector will only have an effect in neutrino oscillations when θ_{13} is non vanishing. An overview of the oscillation parameters determined so far is presented in Tab. 2.1.

In most cases, it is sufficient to consider the oscillation of only two neutrino flavors. This simplification can be done because two of the squared mass splittings are quite different from each other. In the case of two flavor oscillations, the mixing matrix simplifies to:

$$U = \begin{pmatrix} \cos\theta & \sin\theta \\ -\sin\theta & \cos\theta \end{pmatrix}, \tag{2.2}$$

Table 2.1: Neutrino oscillation parameters determined by recent oscillation experiments. Values taken from the Lepton Particle Listings in [33].

Oscillation	Δm^2[eV ^{2}]	$\sin^2(2\theta)$
21 (sol)	$7.59^{+0.19}_{-0.21} \times 10^{-5}$	0.87 ± 0.03
32 (atm)	$(2.43 \pm 0.13) \times 10^{-3}$	> 0.92
31	-	< 0.15

with just one mixing angle θ. Defining the squared mass splitting $\Delta m^2 = m_1^2 - m_2^2$, the oscillation probability can then be expressed as:

$$P_{\nu_\alpha \to \nu_\beta} = \sin^2(2\theta) \sin^2 \left(\frac{1.27 \Delta m^2 L}{E_\nu} \right), \tag{2.3}$$

where E_ν is given in GeV and L in km.

2.2.2 Oscillations in Matter - MSW Effect

The oscillation formalism described above describes the flavor change of neutrinos traveling in vacuum. The presence of matter influences this effect through coherent forward scattering of the neutrinos by the particles along their way. The influence of matter to neutrino oscillations was first suggested by L. Wolfenstein in 1977 [34].

There are two possibilities for scattering of neutrinos: the first is through the exchange of a Z^0 boson with an ambient electron, proton or neutron and the second through a CC interaction between a ν_e and an electron by exchange of a W boson. It is noteworthy that the latter process is only possible for electron type neutrinos in ordinary matter whereas the NC channel is open to all neutrino types alike. The CC channel leads to an extra interaction potential energy V_W for electron neutrinos in matter:

$$V_W = +\sqrt{2} G_F N_e, \tag{2.4}$$

with the Fermi coupling constant G_F and the number of electrons per unit volume N_e [35]. For anti electron neutrinos, the sign of Eq. 2.4 changes.

Analogously, the NC reaction contributes to an extra interaction potential energy V_Z. However, affecting all neutrino flavors equally it does not show any effect in matter enhanced oscillations and is not further regarded here.

The interaction potential energy from Eq. 2.4 has to be considered during the evolution of the neutrino. For simplicity, only two flavor $\nu_\alpha \to \nu_\beta$ oscillations are considered here. It can be shown (see e.g. [35]) that defining

$$\Delta m_m^2 \equiv \Delta m^2 \sqrt{\sin^2 2\theta + (\cos 2\theta - x)^2}, \tag{2.5}$$

and

$$\sin^2 2\theta_m \equiv \frac{\sin^2 2\theta}{\sin^2 2\theta + (\cos 2\theta - x)^2} \tag{2.6}$$

with

$$x \equiv \frac{V_W/2}{\Delta m^2/4E_\nu} = \frac{2\sqrt{2}G_F N_e E_\nu}{\Delta m^2}, \tag{2.7}$$

the oscillation probability for a $\nu_\alpha \to \nu_\beta$ transition in matter is simply expressed by:

$$P_{m,\nu_\alpha \to \nu_\beta} = \sin^2(2\theta_m) \sin^2\left(\frac{1.27\Delta m_m^2 L}{E_\nu}\right). \tag{2.8}$$

The oscillation probability in matter now has the same outline as in the vacuum case presented in Eq. 2.3, with a different effective mixing angle θ_m and squared mass splitting Δm_m^2. As can be seen from Eq. 2.7, these effective values depend on the neutrinos energy. Hence, the influence of matter effects on the oscillation probability is energy dependent. As will be shown in Section 2.3, matter effects play an important role in the oscillation of solar neutrinos. The change of flavor for solar neutrinos inside the Sun is described by the Mikheyev-Smirnov-Wolfenstein (MSW) effect.

Different scenarios have been suggested for matter enhanced oscillations. The most popular mechanism is the large mixing angle solution of the MSW effect (MSW-LMA). In this scenario, a strong energy dependence of the matter effect is limitid to a small energy regime. From Eq. 2.5 and 2.6 one can see that the effective squared mass splitting and mixing angle are close to those of vacuum oscillations in case $x < \cos 2\theta$. On the other hand, for values of $x > 1$, the oscillation probability $P_{m,\nu_\alpha \to \nu_\beta}$ is dominated by matter effects. The region between these limits is called the transition region.

Other theories include an extension of the MSW effect by non standard interaction (MSW-LMA-NSI) [36, 37] or the so called mass-varying neutrino oscillations (MaVaN) [38]. Non standard interactions would result from processes exceeding the standard model and would allow for neutrinos to interact by other means than just the exchange of W or Z gauge bosons. This would add an additional potential to be considered in the neutrino's evolution in matter, leading to deviations in the energy dependent oscillation probability. Very interestingly, only the transition region of matter enhanced oscillations is notably affected by this effect, whereas the vacuum-like and matter-dominated regions are left unchanged [39].

2.3 Solar Neutrinos

The Sun is the most prominent source for neutrinos reaching the Earth. Solar neutrinos originate from fusion processes in the Sun's core. In this section the main processes of energy production in the Sun are described. The impact of matter enhanced neutrino oscillations for solar neutrinos is presented. Finally it is shown that investigating solar neutrinos can give answers to open questions in both oscillation and solar physics.

2.3.1 Fusion Processes in the Sun

The energy production in stars has been first described by Hans Bethe in 1939 [40]. He assumed nuclear fusion to be the source of energy radiated by the Sun. Based on

this assumption, the Standard Solar Model (SSM) was developed which describes the physical processes of our Sun. The Sun consists mainly of hydrogen being held together by gravitation. Towards the core of the Sun, pressure and temperature get high enough to allow for thermonuclear processes. These include mainly fusion of four protons to one helium atom. The two main cycles for this process are the proton proton (pp) chain and the CNO (carbon - nitrogen - oxygen) cycle:

pp chain:

The pp chain starts with one of the two processes

$$\begin{aligned} p + p &\rightarrow d + e^+ + \nu_e \qquad (pp : 99.77\%) \\ p + e^- + p &\rightarrow d + \nu_e \qquad (pep : 0.23\%) \end{aligned}$$

followed by

$$d + p \rightarrow {}^3\mathrm{He} + \gamma.$$

The pp chain then splits up into four branches, mainly depending on the ambient temperature:

pp I (85%):

$$\begin{aligned} {}^3\mathrm{He} + {}^3\mathrm{He} &\rightarrow {}^4\mathrm{He} + p + p \end{aligned}$$

pp II (15%):

$$\begin{aligned} {}^3\mathrm{He} + {}^4\mathrm{He} &\rightarrow {}^7\mathrm{Be} + \gamma \\ {}^7\mathrm{Be} + e^- &\rightarrow {}^7\mathrm{Li} + \nu_e \\ {}^7\mathrm{Li} + p &\rightarrow {}^4\mathrm{He} + {}^4\mathrm{He} \end{aligned}$$

pp III (0.016%):

$$\begin{aligned} {}^3\mathrm{He} + {}^4\mathrm{He} &\rightarrow {}^7\mathrm{Be} + \gamma \\ {}^7\mathrm{Be} + {}^1\mathrm{H} &\rightarrow {}^8\mathrm{B} + \gamma \\ {}^8\mathrm{B} &\rightarrow {}^8\mathrm{Be} + e^+ + \nu_e \\ {}^8\mathrm{Be} &\leftrightarrow {}^4\mathrm{He} + {}^4\mathrm{He} \end{aligned}$$

pp IV /*hep* (10^{-6}%):

$$\begin{aligned} {}^3\mathrm{He} + {}^1\mathrm{H} &\rightarrow {}^4\mathrm{He} + \nu_e + e^+ \end{aligned}$$

CNO-cycle:

CNO I: (99.96%)

$$\begin{aligned} {}^{12}\mathrm{C} + {}^1\mathrm{H} &\rightarrow {}^{13}\mathrm{N} + \gamma \\ {}^{13}\mathrm{N} &\rightarrow {}^{13}\mathrm{C} + e^+ + \nu_e \\ {}^{13}\mathrm{C} + {}^1\mathrm{H} &\rightarrow {}^{14}\mathrm{N} + \gamma \\ {}^{14}\mathrm{N} + {}^1\mathrm{H} &\rightarrow {}^{15}\mathrm{O} + \gamma \\ {}^{15}\mathrm{O} &\rightarrow {}^{15}\mathrm{N} + e^+ + \nu_e \\ {}^{15}\mathrm{N} + {}^1\mathrm{H} &\rightarrow {}^{12}\mathrm{C} + {}^4\mathrm{He} \end{aligned}$$

CNO II: (0.04%)

$$\begin{aligned} {}^{15}\mathrm{N} + {}^1\mathrm{H} &\rightarrow {}^{16}\mathrm{O} + \gamma \\ {}^{16}\mathrm{O} + {}^1\mathrm{H} &\rightarrow {}^{17}\mathrm{F} + \gamma \\ {}^{17}\mathrm{F} &\rightarrow {}^{17}\mathrm{O} + e^+ + \nu_e \\ {}^{17}\mathrm{O} + {}^1\mathrm{H} &\rightarrow {}^{14}\mathrm{N} + {}^4\mathrm{He} \\ {}^{14}\mathrm{N} + {}^1\mathrm{H} &\rightarrow {}^{15}\mathrm{O} + \gamma \\ {}^{15}\mathrm{O} &\rightarrow {}^{15}\mathrm{N} + e^+ + \nu_e \end{aligned}$$

The pp cycle is the dominating process in our Sun. The contribution of the CNO cycle to the Sun's luminosity depends mainly on the core temperature. The SSM currently predicts $\simeq 1.6\%$ of the solar luminosity to be generated by the CNO cycle.

Name	Reaction	Flux [$\mathrm{cm}^{-2}\mathrm{s}^{-1}$]	$E_{\nu,\max}$ [MeV]
pp	$p + p \rightarrow d + e^+ + \nu_e$	5.97×10^{10}	0.422
pep	$p + e^- + p \rightarrow d + \nu_e$	1.41×10^8	$1.442^\dagger$
hep	$^3\mathrm{He} + p \rightarrow {}^4\mathrm{He} + e^+ + \nu_e$	7.90×10^3	18.8
^{7}Be	$^7\mathrm{Be} + e^- \rightarrow {}^7\mathrm{Li} + \nu_e$	5.07×10^9	$0.861^\dagger/0.384^\dagger$
^{8}B	$^8\mathrm{B} \rightarrow {}^8\mathrm{Be} + e^+ + \nu_e$	5.94×10^6	16.34
^{13}N	$^{13}\mathrm{N} \rightarrow {}^{13}\mathrm{C} + e^+ + \nu_e$	2.88×10^8	1.199
^{15}O	$^{15}\mathrm{O} \rightarrow {}^{15}\mathrm{N} + e^+ + \nu_e$	2.15×10^8	1.732

Table 2.2: Solar neutrino fluxes on Earth and energies. The fluxes are predicted by the BPS08(GS) SSM [41]. Neutrinos marked † are mono energetic, for all other neutrinos the maximum energy is given.

Solar neutrino experiments set an upper limit of 2.9% to the fraction of energy that the Sun produces via the CNO fusion cycle [41]. In principle, reactions including also heavier elements are possible. They highly depend on the temperature and the abundances of elements in the star and do not yet contribute to the energy production in our Sun. To be able to predict the neutrino fluxes from the different processes a variety of input parameters is needed for the solar models. One key parameter is the Sun's metallicity Z, being the fraction of heavy elements (> He) in the star. The most elaborate calculations have been developed by the late John N Bahcall [42] and are continued by Peña-Garay and Serenelli [41]. There are significant differences between models assuming a high metallicity (GS) or low heavy metal abundances (AGS). High metallicity models are more consistent with helioseismological data and the predicted neutrino fluxes from this model are presented in Tab. 2.2.

For the pp chain and the CNO I cycle, the net process for fusion is always

$$4p \rightarrow {}^4\mathrm{He} + 2e^+ + 2\nu_e + 26.73\,\mathrm{MeV}.$$

About 2% of the released energy is carried off by the neutrinos. Flux and energy for neutrinos originating from the different processes are shown in Figure 2.1. Neutrinos originating from the *pep* process as well as the fusion of ^{7}Be and a proton are mono energetic because the end state only contains two particles thus resembling a two body decay. Neutrinos from the *pp* reaction have the highest abundance, but are with an energy $< 422\,\mathrm{keV}$ hard to detect.

2.3.2 Solar Physics – Solar Neutrinos as Messengers

Unlike other particles, neutrinos are the only fusion products in the center of the Sun that have the ability to penetrate to the surface and escape into space immediately. Studying the properties of solar neutrinos thus makes it possible to study the processes in the core of our Sun. Measuring the individual fluxes of solar neutrinos from the different fusion process allows to constrain the abundances of different elements as well as temperature and pressure conditions inside the Sun.

Comparing the measured solar neutrino flux to the observed photon luminosity of the Sun allows to test the fundamental idea that the Sun shines by nuclear fusion. It takes a few thousands of years for visible light produced in the Sun's core to reach the Sun's surface, whereas neutrinos are emitted immediately. Neutrino flux

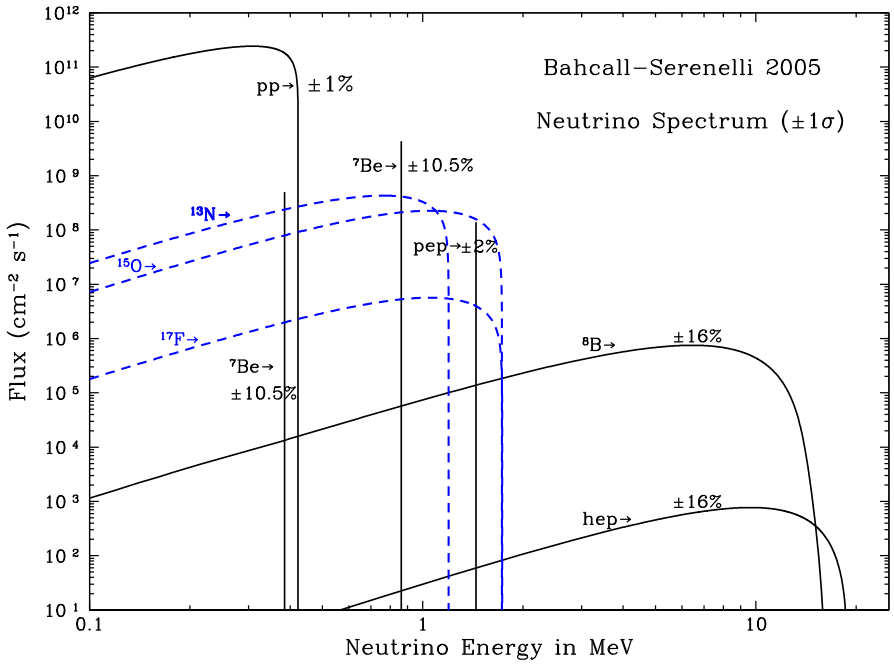

Figure 2.1: Neutrino flux at Earth predicted by the Standard Solar Model. Solid lines: neutrinos produced in the pp-chain, dashed lines: neutrinos produced in the CNO cycle. Figure taken from [43]. For neutrinos with a continuous energy spectrum, the flux is given per MeV bin.

measurements can therefore be used to test the prediction of the SSM that the Sun is in a quasi-steady state in which the energy rate released in the fusion processes equals the surface radiation rate.

2.3.3 Oscillations of Solar Neutrinos

Determining parameters of solar oscillation allows to improve the measurements of Δm_{12} and θ_{12}. Especially the MSW effect presented in Section 2.2.2 offers a large physics potential regarding solar neutrinos. Solar neutrino oscillations would be negligible without matter enhancement. Solar ν_es are mixtures of ν_1 and ν_2 with a negligible component of ν_3. It is thus possible to regard their propagation as a two neutrino phenomenon with the two flavor states ν_e and ν_x, the latter being a combination[8] of ν_μ and ν_τ. From Eq. 2.7 one can see, that the matter effects on a neutrino's oscillation grows with the particle's energy. In the solar neutrino spectrum, the ^{8}B neutrinos have (next to *hep* neutrinos) the highest energy, so the influence of the Sun's matter should be most significant for them. Assuming, solar neutrinos are created in the Sun's core, the particle travels through regions with adiabatic decreasing electron densities N_e on its way to Earth. N_e reduces slowly on the way outside the Sun, leading to a radius r dependent potential V_W. It can be shown that due to the MSW effect, a ^{8}B ν_e produced in the core as a superposition

[8]The exact ν_μ ν_τ composition depends on the atmospheric mixing angle θ_{atm} and is of no importance here

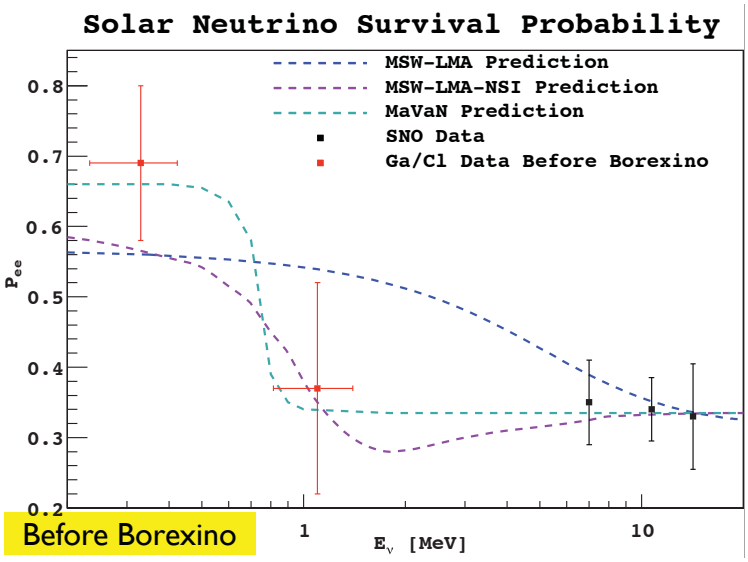

Figure 2.2: Energy dependent survival probability of solar neutrinos for different matter effect mechanisms. The predictions of the MSW-LMA, MSW-LMA-NSI, and MaVaN matter enhanced oscillation models are presented. The data points show the results of various solar neutrino experiments. Figure taken form [44].

of ν_1 and ν_2 will always leave the Suns as a ν_2 mass eigenstate [35]. For the low energetic *pp* neutrinos, the MSW effect shows less influence and their propagation is mainly described by vacuum oscillations. Very interestingly, the transition region between matter and vacuum dominated oscillations is covered by the other different solar neutrinos. Performing a spectroscopic measurement of the solar neutrino flux hence allows to test the MSW predictions. Fig. 2.2 shows the prediction for the different models introduced in Section 2.2.2. On can clearly see the deviations in the transition between vacuum and matter dominated oscillations in the energy region between approximately 1 and 10 MeV. Until recently, with data from solar neutrino oscillation experiments and KamLAND it was not possible to clearly distinguish between the different matter enhanced oscillation models. This has now changed as the Borexino experiment provided a precise spectral measurement of the low energy ^{7}Be neutrino flux, giving further constraints on the allowed oscillation probability in the transition region. The results are presented in Section 4.4.1.

Matter effects can possibly also occur in the Earth. Neutrinos from the Sun arriving at night have traveled some extra distance through the Earth. Matter enhanced oscillations could e.g. reconvert ν_μs and ν_τs formerly produced in the Sun by flavor change back into ν_es, a process wich is called regeneration. The distance which a neutrino travels through the earth before interacting in an experiment depends on the position of the Sun towards the detector, hence on the day time. The resulting difference of the ν_e flux at day and night would thus be observable as an energy dependent day-night asymmetry in the solar ν_e event rates.

The sign of x in Eq. 2.7 is determined by the sign of $\Delta m^2 = m_2^2 - m_1^2$ and therefore depends on whether ν_1 is heavier or lighter than ν_2. The sign of x also changes when considering $\bar{\nu}_e$ instead of ν_e, leading to the interesting fact, that there is an

asymmetry between neutrino and antineutrino oscillations in matter. Determining the matter enhanced oscillation parameters Δm^2_m and $\sin 2\theta_m$ from solar neutrino experiments and combining them with measurements of the reactor $\bar{\nu}_e$ therefore offers an opportunity to probe the mass hierarchy in the solar sector and has provided that fact that ν_2 is heavier than ν_1.

2.4 Other Neutrino Sources

Besides the Sun, neutrinos originate from many sources, both natural and man made. They are involved in nuclear processes as the β decay, fusion and fission. Next to our Sun, all stars emit neutrinos, especially when they come to an end: vast amounts of neutrinos are released in supernova explosions. Neutrinos are also constantly produced in the Earth's atmosphere. The interaction of protons and other particles with the molecules in the atmosphere produces hadronic showers accompanied by neutrinos. But there are not only extra terrestrial neutrino sources. Nuclear power plants as well as natural radionuclides present inside the Earth emit $\bar{\nu}_e$. Last but not least, using particles accelerators allows to create high energy neutrino beams that can be focused on any given experiment. The large variety of neutrino sources is discussed in this section.

2.4.1 Atmospheric Neutrinos

Atmospheric neutrinos are produced from the decays of particles in hadronic showers resulting from interactions of cosmic rays with the Earth's atmosphere. In those interactions, mainly pions and kaons are produced of which then decay ending up with either photons or a μ-ν_μ pair. The muon itself will decay further into an electron, its corresponding neutrino and another muon neutrino. Therefore one would expect an electron type / muon type neutrino ratio R of about

$$R = \frac{N(\nu_e + \bar{\nu}_e)}{N(\nu_\mu + \bar{\nu}_\mu)} \simeq \frac{1}{2}. \tag{2.9}$$

These processes mainly take place in the upper troposphere at heights around 15 km. Neutrinos originating from the Earth's atmosphere have much higher energies than solar neutrinos ranging from about 100 MeV up to 10 TeV. The expression *atmospheric* neutrino suggests that this kind of neutrino predominately comes from the sky in a downward direction towards Earth. This is obviously not true when one considers that neutrinos hardly interact. Atmospheric neutrinos simply penetrate the Earth and are thus coming from all directions. However, this means that a neutrino at the Earth's surface has traveled a distance ranging from ~ 15 to ~ 12800 km, depending on its direction, leading to different ν_μ neutrino survival probabilities. Although the absolute atmospheric neutrino fluxes are hard to predict, these oscillations can be observed in disappearance experiments comparing measurements of R introduced in Eq. 2.9 with expectations. These measurements can even be enhanced by including directional information as well as the energy of the particle and were successfully performed in the 50 kt water Čerenkov detector Super-Kamiokande in 1998 [12] that lead to the first experimental evidence of neutrino oscillations.

2.4.2 Cosmic Neutrinos

The sources of the cosmic radiation causing the atmospheric neutrinos described in the previous section are still not fully explored. Apart from particles associated with solar flares, the cosmic radiation comes from outside the solar system [33]. It reaches energies exceeding $10^{20}\,\mathrm{eV}$, leading to the expectation of also finding ultra high energy neutrinos among it. Neutrinos are not affected by absorption or electromagnetic forces, so they reach the Earth on a direct path from their source. This makes them unique and offers a great opportunity to use them as messenger particles, helping to find any point sources that could be identified as an origin of cosmic rays. Experiments like Antares [45] or IceCube [46] detect these neutrinos using the Earth as a target. Placed deep inside the water (ice), they look for the Čerenkov light produced by high energetic muons or electrons produced in neutrino interaction with the Earth. Ultra high energetic neutrinos are even capable of producing τs with energies high enough to propagate over a distance of the order of 100 m, before decaying and thus leaving a signature of two Čerenkov cones. Hence these neutrino telescopes are sensitive to all neutrino flavors.

2.4.3 Supernova Neutrinos

The hydrogen burning as a source of the energy released by starts as described in Section 2.3 has a limited lifetime, depending mainly on the size of the star. During hydrogen burning, stars are in a hydrostatic equilibrium, meaning that its gravitational forces are counterparted by its radiative pressure. Once the hydrogen is mostly burned up, the core of the star becomes more dense and the temperature rises thus allowing fusion processes of heavier elements, again creating a hydrostatic equilibrium. This process continues for more and more heavy elements, leading to concentric shells that are relics of the previous burning phases. However it has an end once the core contains mainly iron (Fe burning), since at this point no energy can be gained from fusion anymore.

If, at this point, the core of the star exceeds the Chandrasekhar mass limit of approximately $1.4\,M_\odot$, the core collapses due to the gravitational pressure to a neutron star. This is the case for stars more massive than $8M_\odot$ and results in an optically very bright so-called core-collapse supernova. During the collapse, the so-called neutronization or deleptonization takes place converting large amounts of protons into neutrons by electron capture, thus emitting a vast number of ν_e. The collapse is stopped when the core reaches densities $\rho > 3 \times 10^{14}\,\mathrm{g\,cm^{-3}}$, a value normally found for atomic nuclei. The nuclear forces now start to become repulsive, the core is no further compressible and matter bounces back. $\nu\bar{\nu}$ pairs of all flavors are produced and the core cools down by their emission. This simplified picture shows that a supernova leaves a distinct signature in the neutrino spectrum: First the emission of ν_e lasting a few milliseconds followed by the emission of all neutrino types for about 10 s. In these processes, neutrinos carry away 99% of the energy released in the supernova with typical energies of 10 MeV per neutrino. Again, the neutrinos involved can be used as messenger particles giving an early warning of an upcoming (visible) supernova in the electromagnetic spectrum. Most current neutrino experiments capable of detecting supernova neutrinos are therefore connected to the socalled SuperNova Early Warning System SNEWS. In the event

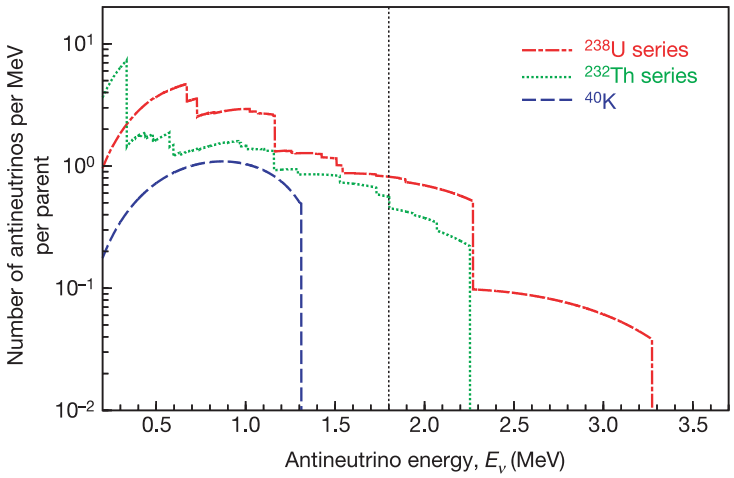

Figure 2.3: Expected $\bar{\nu}_e$ energy distribution for geo-neutrinos from the ^{238}U, ^{232}Th and ^{40}K chain. The dashed line indicated the sensitivity limit for detection via inverse β decay. Figure from [49].

of a galactic supernova at a distance of approximately 8 kpc, about 100 neutrino interaction within a few seconds would be expected in the Borexino experiment.

2.4.4 Geo-Neutrinos

Geo-neutrinos ($\bar{\nu}_e$) are produced in β decays of radionuclides inside the Earth. They were originally proposed bye G. Eder [47] and G. Marx [48] in the 1960s.

The processes inside the Earth are to a large extent still unknown. Seismologists are able to reconstruct the density profile of the Earth but not its composition. And samples taken from holes dig in the upper crust of the Earth's outer mantle can only tell about the geochemical properties up to depth in the order of a few kilometers. Questions about the influence of radionuclides to the terrestrial heat production or the composition of the Earth's core remain unanswered. The investigation of geo-neutrinos can give an answer to the abundance of radioactive elements inside the Earth. The hypothesis of a natural fission reactor in the Earth's core can be addressed.

Neutrino sources inside the Earth are radioactive nuclear isotopes with half-lives of the order of the Earth's age or longer. These are mainly ^{238}U, ^{232}Th and ^{40}K. The resulting energy spectrum from their decay chains is depicted in Fig. 2.3. The picture also marks the sensitivity limit for the detection of geo-neutrinos via the inverse β decay, which has a threshold energy of 1.806 MeV. This way only selected geo-neutrinos from the ^{238}U and ^{232}Th chains can be detected. The relative abundances of the different sources can then be identified by comparing the measurements to the different distinct energy spectra. The existence of geo-neutrinos was first shown by KamLAND in 2005 [49] and recently confirmed by the Borexino experiment [50].

Measurements in different locations can give new constraints on the thorium and uranium abundances in the Earth's crust and mantle. The study of geo-neutrinos can also help to understand the terrestrial heat production, that is a tiny heat flux of approximately 60 to 90 mW/m^2 emitted by the Earth. Although this is a

comparably small value, integrating this over the Earth's surface leads to a value of 30 to 45 TW, an equivalent of ten thousand nuclear reactors [51]. The source of this heat is still unknown. One hypothetical explanation was the existence of a natural thermonuclear reactor in the Earth's core. However, recent geo-neutrino measurements by the Borexino experiment disfavor this hypothesis [50].

2.4.5 Nuclear Reactors

Nuclear reactors produce electricity from the thermal power of nuclear fission. Nuclear power plants are usually fueled with ^{235}U, ^{238}U, ^{239}Pu and ^{241}Pu. The daughters of the fission process are mostly unstable nuclei thus emitting $\bar{\nu}_e$ in β^- decays. Altogether, an average of $\sim 6\,\bar{\nu}_e$ per fission are produced. The energy spectrum of these neutrinos is still not known without uncertainties and covers a range up to 12 MeV with a mean energy between 2 and 3 MeV. Fig. 2.4 shows the predicted neutrino fluxes of neutrinos from the main fuel components of typical nuclear reactors as presented in [52].

Reactor neutrinos can be used in various kinds of experiments. As mentioned before, the very first neutrinos were observed at the Savannah River reactor. Reactor neutrinos have been used in many short and intermediate baseline experiments and the KamLAND detector investigates neutrino oscillations over long baselines in Japan [30]. Because of the different sign in Eq. 2.4 for neutrinos and anti neutrinos, a distortion between solar ν_e and reactor $\bar{\nu}_e$ oscillations is expected for matter enhanced oscillations. The sign of x in Eq. 2.7 depends on the squared mass splitting Δm^2. In the case of ν_2 being heavier than ν_1, x is positive for neutrinos and negative for anti neutrinos. In the case of ν_2 being lighter than ν_1 it would be the other way around. Comparing solar and reactor oscillation data hence offers an opportunity of determining the sign of $\Delta m^2_{\odot}$. Monitoring $\bar{\nu}_e$ fluxes from nuclear sites might also be used as a tool for the verification of the Non-Proliferation Treaty of Nuclear Weapons.

Reactor neutrinos are not only a welcome source for neutrino experiments, their flux also is a background for any $\bar{\nu}_e$ search from other sources like geo-neutrinos.

2.4.6 Neutrino Beams

The second man made neutrino source are neutrino beams. Neutrino beams can be produced at particle accelerators from the decay of π and K mesons. These are generated by shooting high energy protons on a target (e.g. graphite). The charged mesons can be focused by magnetic lenses before they then decay mainly into muons and their corresponding neutrinos. If energies are high enough, the decay particles will fly straight in the forward direction, where the muon is then absorbed by a muon dump before it decays further. The neutrino however travels on in the beam direction. The magnetic lensing system allows to focus the parent particles and hence the neutrino beam on any given experiment. It is also sensitive to the energy of the parent meson so that the mean energy of the neutrinos can be controlled. By selecting only parents of a distinct charge, either neutrinos or anti neutrinos are chosen for the beam. Beams produced this way thus consist either of ν_μ or $\bar{\nu}_\mu$ and are used for various short and long baseline experiments.

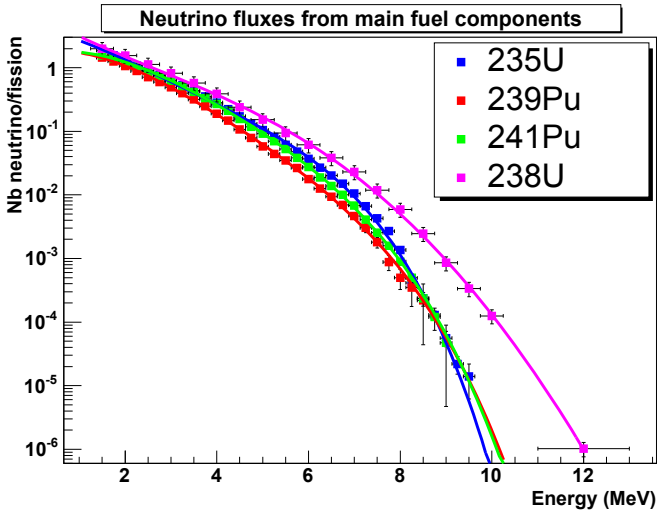

Figure 2.4: Typical $\bar{\nu}_e$ energy spectrum from neutrinos emitted by the decay of the daughters of ^{235}U, ^{238}U, ^{239}Pu and ^{241}Pu after fission in a nuclear reactor. Figure from [52].

Currently, three noteworthy neutrino beams are in operation: the CNGS[9] beam in Europe [53], the NuMI[10] beam in the USA [54] and the T2K[11] beam in Japan [55]. The CNGS beam is focused on the LNGS underground laboratory, where the OPERA experiment is looking for ν_τ appearance in the ν_μ beam.

In the context of this thesis, neutrino beams are of interest mainly for two reasons. First of all, the CNGS beam mentioned above crosses the Borexino detector before it hits OPERA. It's impact thus has to be taken into account when analyzing Borexino data. As will be shown in Section 5.5 it can even be used for a calibration of the Borexino muon tracking. However, it should also be noted that one of the primary goals of neutrino beam experiments will be the measurement of θ_{13} and δ_{cp}. To determine these parameters, a three flavor oscillation analysis is necessary which relies strongly of a precise knowledge of Δm_{12} and θ_{12}. Whereas the most precise values of Δm_{12} come from reactor experiments, solar neutrino experiments like Borexino will provide the measurements of the solar mixing angle with the needed precision.

[9] CNGS CERN Neutrinos to Gran Sasso
[10] NuMI Neutrinos at Main Injector
[11] T2K Tokai to Kamioka

Chapter 3

The Compact Muon Tracker CMT

Cosmic muons are a major source of background in all neutrino experiments. As they penetrate deep into all kinds of matter, a complete shielding against cosmic muons is virtually impossible. Even in an underground laboratory as deep as the LNGS the muon rate still cannot be neglected. Thus it is utterly important to understand well both the effects of muons interacting within the experiment and with the surrounding matter, and also to effectively track these muons to be able to reduce the background induced in the detector. The compact muon tracker CMT is a device which has been designed to perform this task. It is a compact detector which can track muons with a precision of a few 100 µm. The design is based on the drift tube technology used for the Precision Tracker (PT) of the OPERA experiment. Whereas the PT can reconstruct only 2D muon tracks, former test modules have been modified in the CMT setup so that a 3D track reconstruction is possible. This chapter gives a short overview of the detection principle of drift tubes. Then the CMT setup and its performance are described. Finally, results from CMT measurements in Hamburg are presented and compared to Monte Carlo studies.

3.1 Drift Tubes

Drift tubes are devices to detect charged particles and to reconstruct their tracks with a high precision. When a charged particle travels through a medium—in this case a gas—it loses energy through ionization and thus leaves a trace of ions and electrons in the gas. Applying an electrical field inside the drift tube the electrons can be detected in form of small electrical currents at the anode. Taking into account the position of the anode wires and the drift times of the electrons allows a spatial reconstruction of the track. This section describes the working principle of drift tubes and gives an overview of the track reconstruction methods.

3.1.1 Detection Principle

When a charged particle traverses through matter it loses kinetic energy through atomic excitation and ionization. The loss of energy in matter is described by the

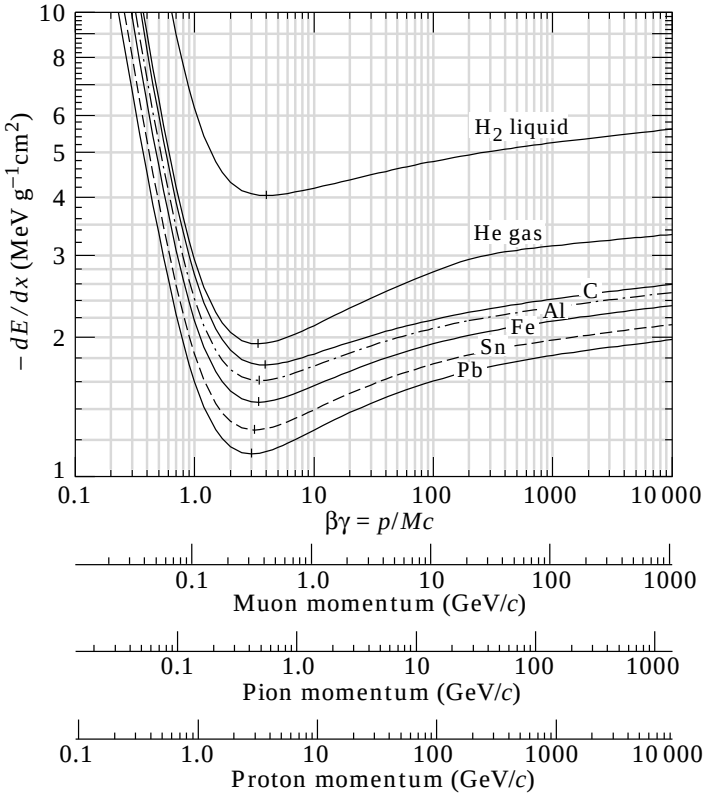

Figure 3.1: Mean energy loss in different mediums for protons, pions and muons [56].

Bethe-Bloch Equation:

$$-\frac{dE}{dx} = Kz^2\frac{Z}{A}\frac{1}{\beta^2}\left[\frac{1}{2}\ln\left(\frac{2m_e c^2\beta^2\gamma^2 T_{\max}}{I^2}\right) - \beta^2 - \frac{\delta(\beta\gamma)}{2}\right] \tag{3.1}$$

with $K = 4\pi N_A r_e^2 m_e$, ze the charge of the incident particle, Z and A the atomic number and mass of the absorber, respectively, m_e the electron mass, β the particle's velocity in units of the speed of light, γ the relativistic gamma factor, $T_{\max} = \frac{2m_e\beta^2\gamma^2}{1+2\gamma m_e/M+(m_e/M)^2}$ the maximum kinetic energy which can be imparted to a free electron in a single collision by a particle of mass M, I is the mean excitation potential of the target, N_A Avogadro's constant and $\delta(\beta\gamma)$ a density effect correction to ionization energy loss [56]. Hence the specific energy loss depends mainly on the particle's energy and the properties of the traversed medium. Figure 3.1 shows $-\frac{dE}{dx}$ distributions for different particles.

Drift chambers use the ionization of gases by charged particles to detect and reconstruct particle tracks. When a charged particle traverses a gas, it can interact with its molecules and knock out electrons leaving ionization pairs of a positive charged ion and the knocked out electron. Along the particles track, ionization pairs are typically created in clusters. Applying an electric field to the gas, electrons and ions will start drifting to the anode and cathode according to their charge. The lighter electron will travel much faster to the anode than the heavier positively

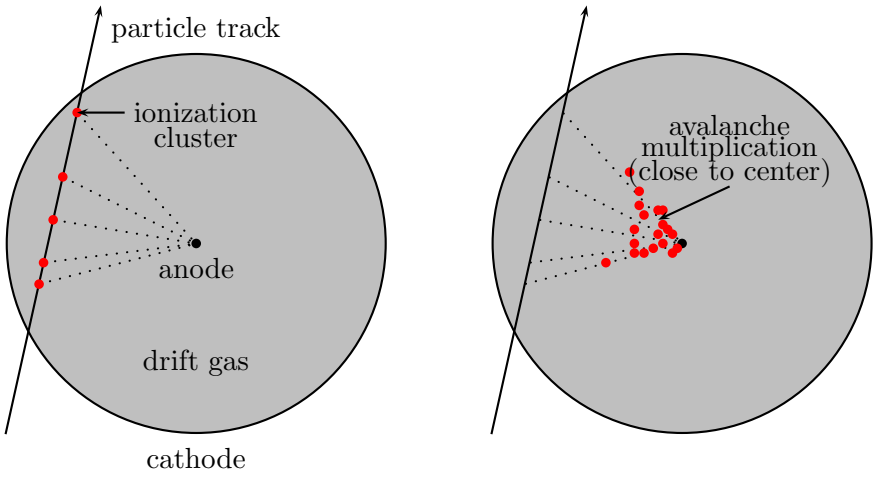

Figure 3.2: A drift tube with a particle track. A charged particle leaves ionization clusters along its trajectory. These charges will be collected at the electrodes (tube and anode wire). If a strong electric field is applied between the electrodes, avalanche multiplication will occur—mainly in the vicinity of the anode wire. The red dots show electrons from the ionization pairs. The drifting electrons leave a tail of positively charged ions which slowly drift to the cathode and are not shown here.

charged ions towards the cathode. The electrons energy loss due to scattering in the drift gas will be counterparted by the acceleration in the electric field. Arranging the field with a centered anode and a surrounding cathode as shown in Figure 3.2 results in an electric field

$$E(r) = \frac{U}{\ln(r_c/r_a)} \cdot \frac{1}{r}$$

where r_c and r_a are the radii of the cathode and anode wire respectively. U denotes the applied voltage. This field is weak on the outside, getting significantly stronger towards the center. This radial symmetry is realized in drift tubes. The wire in the center is connected to a high voltage acting as the anode while the tube itself functions as the cathode. Electrons from ionization clusters are attracted by the anode in the center. While traveling through the gas they excite and ionize more atoms and molecules thus more and more free electrons start drifting towards the anode. This avalanche multiplication mainly occurs close to the wire where the electric field is strongest. It results in a measurable electric signal [57].

To determine the position of a track within a tube, the measurement of drift times t_d is necessary. In addition to the arrival time of a signal on an anode wire an external trigger has to provide a time signal of the passing primary particle. The time difference between the undelayed trigger and the drift tube signal is the drift time. The distance of the track from the anode wire can then be determined by a drift-time-to-distance relation (cf. Section 3.5.3). This relation has to be obtained by calibration measurements. Comparing single drift-times with the drift-time-to-distance relation allows to reconstruct only the distance r of a track from the center of a tube which can be any point on a circle with radius r around the anode wire. Hence measurements from different tubes are required to reconstruct a particle track. Since the track is given by the common tangent to all drift circles, at least three

Figure 3.3: Setup of the muon tracker in the laboratory in Hamburg. The photograph shows the four drift tube modules placed on top of each other. Two of the modules are rotated by 90°. The HV and preamp boards are placed at the front end of the modules (cf. Section 3.2.4 for details). The read out and control electronics as well as the power supplies are located in the rack behind the detector. On top and underneath the detectors, layers of plastic scintillators are placed for triggering. To reduce triggers from low energetic cosmic showers, a layer of lead is placed above the lowest scintillator.

drift tube hits are needed to find an unambiguous solution.

3.2 Setup

The muon tracker is built out of four identical modules formerly used as a prototype of the OPERA PT [58]. This section describes the layout of these modules as well as their setup for a 3D reconstruction. A photograph of the setup is shown in Fig. 3.3.

3.2.1 Drift Tube Modules

Each module consists of 48 aluminum drift tubes. The tubes are arranged in four layers. Each tube has an outer diameter of 38 mm and an inner diameter of 36.3 mm. In the center of each tube, a gold plated tungsten wire of 45 µm diameter is strung serving as an anode. The modules are 1.05 m long (1.10 m including end plates). The end plates have a cross section of $19.4 \times 55\,\mathrm{cm}^2$.

Each layer of 12 drift tubes within a module is shifted against the neighboring layer. The staggering has been optimized for a maximum number of hits for tracks perpendicular to the drift tube plane. A cross section of the drift tube modules is presented in Fig. 3.5. In each layer the tubes are arranged at a distance $\Delta x = 42\,\mathrm{mm}$. The following layer is shifted by $-21\,\mathrm{mm}$ in the x-direction, so that the center of a tube is at a distance of again 42 mm to both neighboring tubes in the first layer. The shift in y is thus given as $\Delta y = \sqrt{42^2 - 21^2}\,\mathrm{mm} \simeq 36.4\,\mathrm{mm}$. The next layer is then shifted by 40.6 mm in the y-direction whereas the x-coordinate is shifted asymmetrically by 11 mm. The fourth layer is then again shifted symmetrically by

Table 3.1: Reference coordinates for the anode wires of the n^{th} tube of a layer. Counting starts at 0.

Layer	x [mm]	y [mm]
3	$(n-5)\cdot 42+11$	113.4
2	$(n-5)\cdot 42-10$	77
1	$(n-5)\cdot 42-21$	36.4
0	$(n-5)\cdot 42$	0

Table 3.2: Module setup of the muon tracker. The name of the module refers to the description in Fig 3.4.

Module	TDC	Channels	Plane	z-Position
a.0	1	0-47	$x-z$	-182 mm
a.1	1	48-95	$x-z$	-559 mm
b.0	0	0-47	$y-z$	0 mm
b.1	0	48-95	$y-z$	-377 mm

$x = 21\,\text{mm}$. An overview of the resulting coordinates of the anode wires can be found in Tab. 3.1. For historical reasons, the center of the module is defined as the position of the anode wire in the 6^{th} tube of the first layer.

3.2.2 Module Setup

In a first setup for 3D track reconstruction the four modules where placed on top of each other, where every second module was rotated by an angle of 90°. Two layers of plastic scintillators were placed on top and underneath the detector for triggering. To maintain a right-handed coordinate system, the front end of the second and fourth module from the top were placed in the $x-z$ plane whereas the remaining modules are hence associated to the $y-z$ plane. The reference system is shown in Fig. 3.4. The topmost module is placed at $z = 0\,\text{mm}$. The following modules are placed at $z = -182\,\text{mm}$, $z = -377\,\text{mm}$ and $z = -559\,\text{mm}$, respectively. All relevant parameters of the setup are summarized in Tab. 3.2. A cross section of the modules is shown in Fig. 3.5, due to the cabling of the detector (cf. Section 3.2.4), the origin of the coordinate system lies in the tube mapped with channel 42 of TDC 0.

3.2.3 Drift Gas

The tracker is operated with a gas mixture of Ar/CO_2 at a ratio of 80/20. The gas is provided by a pre-mixed gas bottle. During operation, the gas is exchanged permanently. A flow meter controls the gas flow. A bubbler is used at the exhaust end of the last module. Hence, air is prevented from entering the module. The resulting pressure inside the modules is thus set slightly above the ambient pressure.

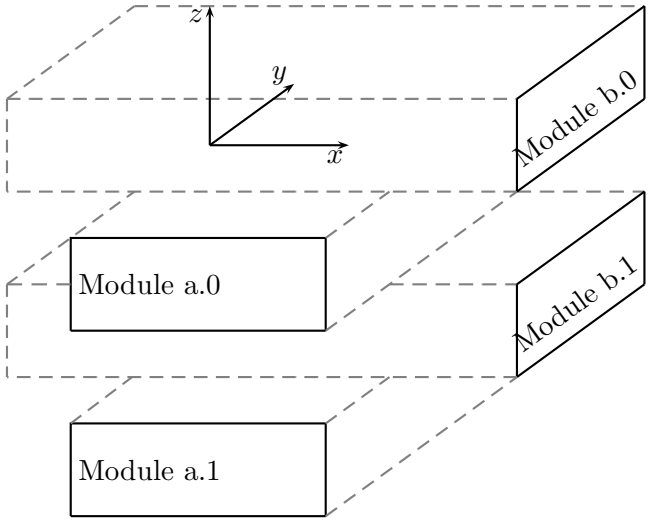

Figure 3.4: Reference system of the prototype. Solid lines denote the front (electronics) end of each module. Modules with the same letter (a or b) are connected to the same TDC. The exact coordinates of the modules are presented in Tab. 3.2.

3.2.4 Electronics

The electronics for data readout and slow control are mounted at one end of a module. High voltage is distributed to the anode wires via a high voltage (HV) board. One board per layer is used. The end of each anode wire is lead through the end cap of the tube and directly soldered to the HV board. The board also has connectors for the read out electronics, where the so-called preamp boards are plugged in. As the name suggests, the preamp boards contain the electronics for the amplification of the drift tube signals. The amplification is done by the *L3 chip set* [59], a preamp board contains three of these chips, each connected to four channels. Besides pre-amplification, the board also contains a discriminator for each channel which is used to set the signal threshold. Through the preamp board it is also possible to send test pulses on each channel. Both the discriminators and the test pulse function are controlled via a special slow control support board described in the next section. Each preamp board is connected to the read out and control boards by a ribbon cable. The orientation of the HV board and the order in which the ribbon cables are connected to the TDC (top to bottom or vice versa) determine the channel mapping. The CMT has been cabled from top to bottom. The HV board was mounted in a way, that smaller numbered channels start on the right side of the module. This leads to the channel map depicted in Fig. 3.5.

Time measurement, trigger and slow control electronics are all located in one crate. Two modules at a time are connected to both a support board and and a TDC board. A trigger board provides the trigger for all modules.

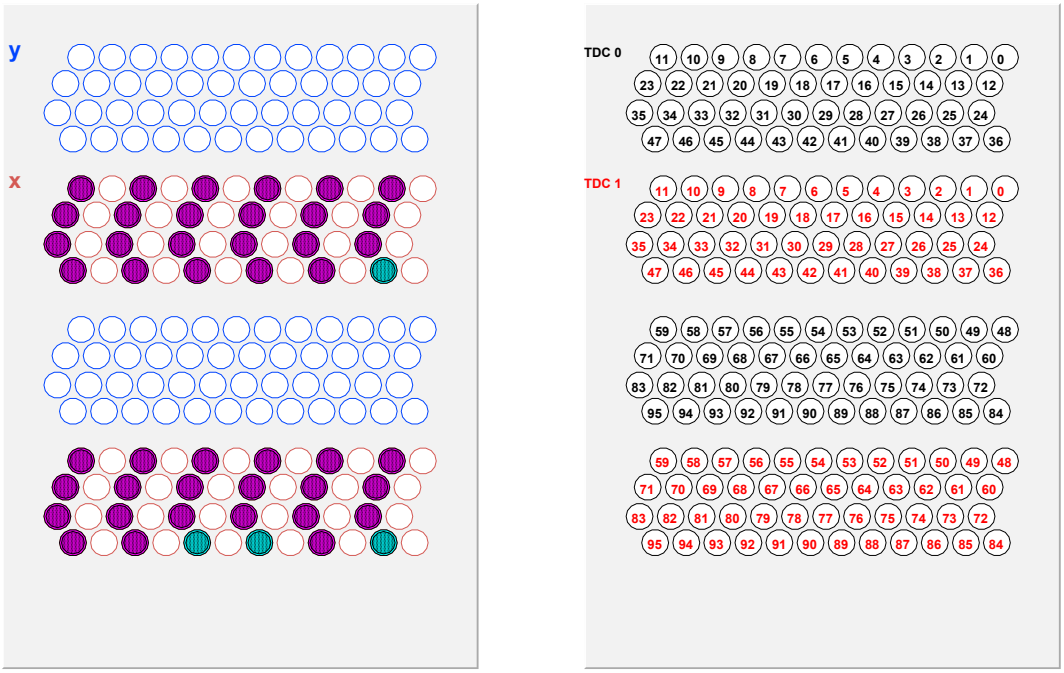

Figure 3.5: Left: Online display of test pulse events. The event shows test pulses for all odd channels on TDC 1. Right: Channel assignment of the Compact Muon Tracker. Different colors indicate the different TDCs and hence different planes. The origin of the coordinate system lies in the tube mapped with channel 42 of TDC 0. The picture shows an overlay of the $x-z$ and $y-z$ plane.

3.2.5 Slow Control

The slow control of the preamp boards is mainly done through the OPERA Support Board (OSUB). It is used to set all relevant parameters on the preamp boards. The OSUB can be addressed via CAN[1] bus. For the operation of the muon tracker, a new control software has been developed within this thesis. Unlike the OPERA OSUB software it is based on Linux and has a simple console output in form of dialogs. This has the advantage that only one computer is needed for the whole operation of the detector including the DAQ. Also, remote control is easier without the need of a graphical display. The same software is used to control the trigger board. The user interface of the slow control software is depicted in Fig. 3.6. A list of variables which can be set by the program can be found in Tab. A.1. Most important is the setting of the discriminator threshold. It can be set for either a single channel or for all channels at a time. Furthermore, test pulses can be generated to test the functionality of the preamps and data acquisition. For a complete overview of the OSUB see [60].

The slow control software is also capable of communicating with the OPERA Trigger Board (OTB). It is used to distribute the external trigger signal to all TDCs. The OTB has five input channels of which only two are used in this setup, one each for the scintillators above and below the detector. With the slow control, the coincidence requirement can be set (both scintillator layers have to have a coincident

[1] CAN Controller Area Network

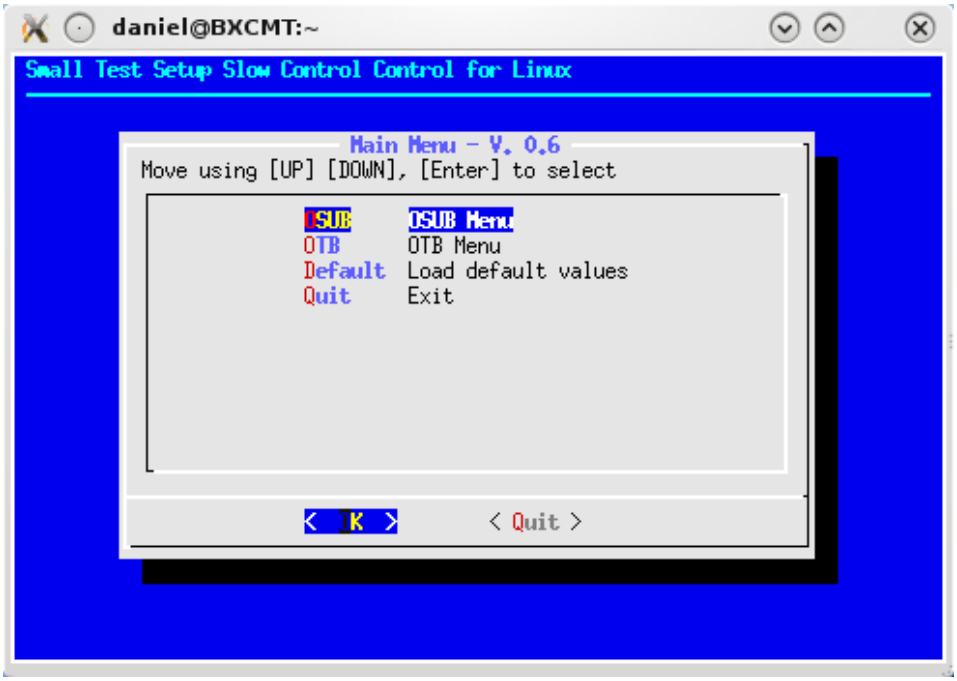

Figure 3.6: Display of the slow control software. In the main menu, one can choose the kind of control board to be addressed (OSUB or OTB). The following sub menus allow to set thresholds, delays, etc. The slow control software is text based, so that it can be easily controlled via non graphical terminals.

signal in this case) and the delay Δ of the trigger signal can be modified. Also random trigger test pulses can be generated which are used to test the noise behavior of the detector. A detailed description of the OTB can be found in [61].

For the CAN bus communication a PEAK PCAN-USB CAN to USB interface has been used. A Linux kernel module was provided by the manufacturer. Once it is loaded and the adapter is connected via USB, it can be addressed from the controller PC as `/dev/pcan32` by simply sending text messages to the device [62].

Test Pulses To test the functionality of the preamp electronics as well as the data acquisition, test pulses can be sent from the OSUB boards. A test pulse for a certain tube mimics a hit. Test pulses can either be sent to a single tube or to all odd or even channels of one OSUB board. The test pulse itself serves as a start signal; a stop signal is also generated by the OSUB and distributed to all TDCs via the back plane of the crate.

3.2.6 High Voltage

The HV is provided by a CAEN SY 127 Power Supply. It is equipped with a 6 kV, 1 mA positive HV module containing four channels. Each HV channel is connected to four layers of drift tubes, always one layer per module. This way it is ensured that three layers per module remain active if one HV channel trips. The cosmic muon tracker is operated with a voltage of 2350 V. The Power Supply can be controlled

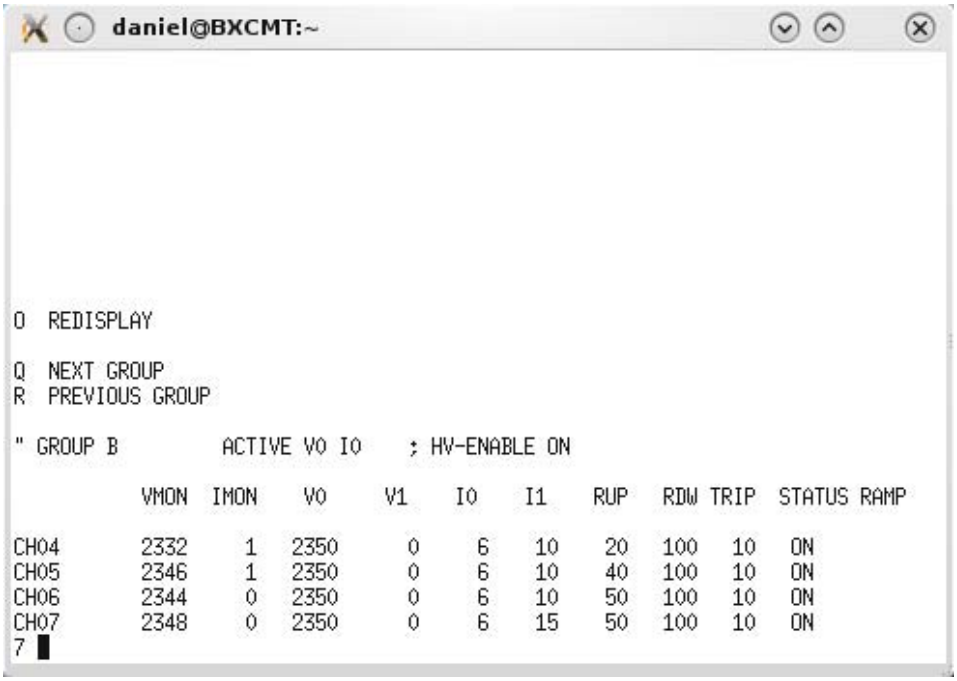

Figure 3.7: Remote control for the anode HV. The actual control software runs on the SY 127 HV supply itself and is controlled via a RS232 serial connection. This is accessed via a terminal emulator running on the control PC.

from the controller PC via a RS232 interface (cf. Fig. 3.7).

3.3 Data Acquisition

The data acquisition is done with the same TDC boards as used for the OPERA detector. One TDC board has 96 channels and can thus take data from two modules. The TDC boards are read out via Ethernet. They are connected to the crate via Harting back plane connectors.

3.3.1 TDC board

The task of the TDC board is the measurement of the drift times. Each TDC board contains twelve TDC chips with eight measuring channels each. Each channel uses a differential GTL[2] input as a start signal. A common stop signal is used for all channels. The TDC has a measuring range of 3.2 µs, its resolution is quoted as approximately 1.5 ns. [63]

Trigger, Start and Stop For the track reconstruction the distance r of the muon track to the anode wire is of interest. It can be determined from the drift time t_d as described in Section 3.5.3. For measuring the drift times, an external trigger is needed at the time when the muon passes the detector. This is provided by the

[2]GTL Gunning Transceiver Logic

plastic scintillators. To avoid all TDC channels from counting for each event, only those channels which receive a signal from a drift tube hit start time counting at the time the signal arrives. This is referred to as the start signal. The counting stops when the trigger board sends a stop signal to all TDCs at a fixed time period Δ after the trigger. The stop signal is distributed via the crate's back plane to all TDCs. With t_c being the time counted by a TDC channel, the drift time is hence given by

$$t_d = \Delta - t_c \tag{3.2}$$

meaning that larger values of t_c mean smaller drift distances. The maximum measurable TDC value hence arises from tracks hitting the anode wire directly and is expected to be at $t_c = \Delta$.

The TDC uses a 12 bit register for the time measurement. The resulting 4096 channels are used over the measuring range of 3200 ns, leading to a channel width of $\frac{25}{32}$ ns. However, neither the knowledge of the absolute drift times in seconds nor the exact value of Δ are important for the determination of the drift distance since r can be directly correlated to the TDC channel. This will be described in Section 3.5.3.

When the TDC receives a trigger signal, measurements are stopped for all channels. A 2 bit hit classification is now done. For a normal drift time measurement this is simply set to 0. If the channel did not receive a start signal earlier, it is set to 1, meaning no hit. If the TDC channel starts counting independently of any event (e.g. because of an untriggered particle penetrating a tube), an overflow is registered. If a real event occurs shortly after this - before the channel was reset, the hit bits are set to 2 (called OV ROZ). Finally, hit type 3 (OV ALU) indicates an overflow of the internal arithmetic logic unit during the drift time determination. For the drift time measurement, only events with hit type = 0 are of interest.

Besides the drift times and hit information, the TDC also measures the pulse width. Pulse widths Δ_p are classified into four types:

0: NO WIDTH; no pulse width could be determined (e.g. when the stop signal arrives before the actual signal which is a sign for a too small delay Δ)

1: SMALL; $\Delta_p <\sim 13\,\text{ns}$

2: MEDIUM; $\sim 13\,\text{ns} \leq \Delta_p <\sim 82\,\text{ns}$

3: LARGE; $\sim 82\,\text{ns} \leq \Delta_p$.

The pulse width information is also added as a 2 bit segment to the measurement. Hence the result register of each channel contains a 16 bit value altogether:

$$\overbrace{\mathtt{b}_{15}\mathtt{b}_{14}}^{\text{hit}}\overbrace{\mathtt{b}_{13}\mathtt{b}_{12}}^{\text{width}}\overbrace{\mathtt{b}_{11}\mathtt{b}_{10}\mathtt{b}_{9}\mathtt{b}_{8}\mathtt{b}_{7}\mathtt{b}_{6}\mathtt{b}_{5}\mathtt{b}_{4}\mathtt{b}_{3}\mathtt{b}_{2}\mathtt{b}_{1}\mathtt{b}_{0}}^{\text{drift time (TDC count)}}.$$

Each TDC board is read out via Ethernet. The IP address of each TDC is set by three rotation switches on the board starting at `172.16.4.2`. Data readout is done via a mezzanine board which is attached to the TDC board. The mezzanine runs a simple Linux and can be accessed via `telnet`. It accesses the raw data from the TDC and combines it with the time information from the clock.

The controller PC communicates with the mezzanine through a dedicated Ethernet controller card. The IP address `172.16.4.1` is assigned to this card. For data taking, an NFS[3] server is running on this machine. The actual DAQ application is provided on the NFS server. The NFS share is mounted by each mezzanine and the DAQ application is obtained during boot up. Upon request from the controller PC, data is written into the NFS share.

For the data acquisition, a set of *Test Acquisition tools* is used [64]. For each run a directory in the NFS share is created. Each TDC then writes its data into a subdirectory named after its IP address. The data is written in binary format in files called `tdcdata.n` where `n` is the number of the file. Once a file reaches a given size (typically 10 MB) it is closed and a new file is used. The binary data has a 32 bit structure which is described in Appendix B

Event Time Information The TDCs need a clock signal for running. In the OPERA experiment, a high precision clock distribution is needed and provided. For the compact muon tracker the clock is emulated by a clock emulation board. This board sends fake clock signals to the boards which cannot be used as real time information. To get at least a rough time estimation, the DAQ software has been modified to include the computer time as a time stamp. Therefore the 32 bit segment of the time stamp is filtered in the data stream and exchanged with the computer time. Since the TDC boards are read out only once per second, the timestamp has an accuracy of less than one second. The computer itself is synchronized via ntp[4].

3.4 Operation

The operation of the muon tracker requires two TDC boards and OSUBs as well as one trigger board which were fitted into the same crate. Each two modules within one 2D plane were connected to the same boards.

Two layers of plastic scintillator were used for triggering. Two crossed scintillators with an area of $90 \times 60\,\mathrm{cm}^2$ each built the upper layer whereas only one scintillator with the same area was used for the layer underneath the modules. A fourth scintillator with the same dimensions was placed yet underneath the whole setup, with a 10 cm lead overburden to shield low energetic particles from cosmic showers.

The functionality of the data taking was verified using test pulses. To be able to obtain a quick overview of working and non-working channels, a quasi online event display was developed. As described in Section 3.3, data is recorded in 32 bit chunks and read out from the TDC once per second. The online display permanently watches the read out file and visualizes any hit. A typical test pulse pattern for one module is shown in Fig. 3.5; multiple test pulses can be sent to either all even or all odd channels. Fig. 3.8 shows a hit map after 3000 test pulses for one TDC. As expected almost all tubes have been hit 3000 times. Only channel zero shows a noisy behavior. This occurs mostly due to a non set threshold but can also be an indication for a malfunction of the preamp board.

[3] NFS Network File System
[4] ntp network time protocol

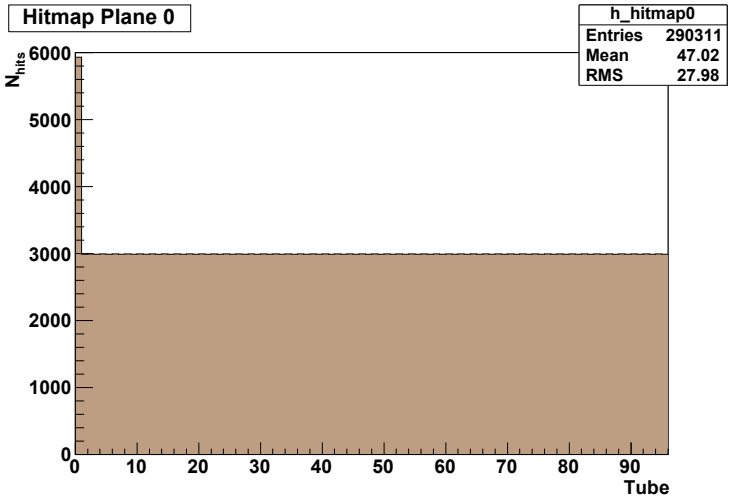

Figure 3.8: Test pulse hit map of TDC 0. 3000 testpulses have been generated, channel 0 shows noisy behavior.

3.5 Data Processing

All data processing is done with the software `cmtrack` written in `C` and `C++` within this thesis. This section describes the functionality of the software package. A detailed look at track reconstruction, calibration and alignment is then presented.

3.5.1 Software Package `cmtrack`

The analysis software is started by calling `cmtrack`. A full list of options is given calling `cmtrack -h`. The program uses the `ROOT` analysis software[5]. Data processing always starts with reading the binary data. It is converted into a `ROOT` tree saved in the file `tdcdata.root`. A list of used files and the information stored within is shown in Tab. 3.3.

The analysis software needs some basic facts on the setup of the detector as input paramteres. The following information has to be stored before using the program in a textfile in the working directory under `./dat/modules.dat` for each module:

- The TDC it is connected to [`0,1,...`]
- Whether the first or second 48 channels are used [`0,1`]
- x- or y-offset of the module (depending on the plane) [`float` in mm]
- z-offset of the module [`float` in mm]
- Plane of the module [`0,1`] for $x-z$-plane or $y-z$-plane respectively
- The order in which the layers are connected to the TDC [`0,1`] (top to bottom or vice versa)

[5] `ROOT` is a powerful analysis software developed at CERN.

Table 3.3: Data structure for raw and reconstructed data.

File	Tree name	Description	Branch	Content
tdcdata.root	TData	Raw TDC data, one entry per event	int tdcvalue⟨i⟩[96]	Raw TDC data of TDC number i (96 channels)
			int tdchit⟨i⟩[96]	TDC hit info of TDC number i (96 channels)
			int tdcwidth⟨i⟩[96]	TDC width info of TDC number i (96 channels)
			int nhit⟨i⟩	Number of hits in event in TDC number i
			int eventnr	Event number
			int cycle	Cycle number
			uint timestamp	Timestamp in UNIX time
reco.root	TRecoData	Tree with reco data, one entry per reconstructed event	double alpha<n>	Hesse parameter α in plane n
			double p<n>	Hesse parameter p in plane n
			double phi	Azimuth angle of track
			double theta	Polar angle of track
			+ all data from TData	
	TAnaData	Single info for each hit used by a reconstructed track	int tdcbin	TDC value of hit
			double dist	Calculated distance of track
			double delta	Residual
			double radius	Drift radius
			double sigma	Resolution
			int tube	Tube number within TDC
			int tdcn	TDC number
			int eventnr	Event number
			int n_used_hits	Number of hits used for reco
			int n_hits	Number of hits in event
			double alpha	Hesse parameter α
			double p	Hesse parameter p
single_reco.root	TSRecoData	Similar to TRecoData for single reco	double alpha<n>m<m>	Hesse parameter α for TDC n, module m
			double p<n>m<m>	Hesse parameter p for TDC n, module m
	TAnaData	Same as in reco.root		

Table 3.4: Data structure for calibration, position and alignment data.

File	Tree name	Description	Branch	Content
`calib.root`	`TCalib`	Tree with 4096 entries, one for each TDC bin	`int tdcbin`	TDC value
			`double radius`	Drift radius
			`double sigma`	Resolution
	`TBound`	Tree with only one entry	`int min`	Lower boundary
			`int max`	Upper boundary
`geo.root`	`TPlane<n>`	Tree with all modules within a plane (0,1)	`int tdc`	TDC number
			`int subtdc`	module number
			`int igeo`	Reference to entry in `TGeo`
	`TGeo`	Basic information for each module	`int tdc`	TDC number
			`int subtdc`	module number
			`float x`	absolute x/y coordinate of module center
			`float y`	absolute z coordinate of module center
			`int plane`	Plane information [0,1]
			`int plug`	Order in which TDC cables are attached [0,1]
			`float orient`	rotation of module
			`int iwire`	Entry in `TGeo` of first wire within module
			`int back`	Orientation of HV board [0,1]
	`TWire`	96 Entries per TDC, one for each wire	`int tdc`	TDC number
			`int subtdc`	Module number
			`float x`	x/y coordinate within module
			`float y`	z coordinate within module
			`int mask`	Information, whether the channel is masked (`1`=masked)
`align.root`	`TAlign`	Alignment data	`float dx`	x/y shift for each wire
			`float dy`	z shift for each wire

- Rotation of the module (front side, [0-360] in °)
- The orientation of the HV Board [0,1]

For each module, one line is added to the file. Furthermore it is possible to mask channels. This is useful to get rid of noisy channels. Also, it is advisable to mask dead channels, so that the pattern recognition ignores the according tube when checking for missed hits. Masked channels simply have to be listed in the file `./dat/mask.dat` For each channel to be masked, a line with two integers has to be added, first the TDC number followed by the channel number.

Once the raw data has been read, the geometry can be initialized with `cmtrack -i`. This creates a file `geo.root` where all wire positions as well as the module assignment to the different planes are stored. Raw data has to be read beforehand, because an initial calibration is also done during this step (cf. Section 3.5.3). The calibration data is stored in `calib.root`. For a list of variables stored during initialization and calibration refer to Tab. 3.4. Once initialized, the software can perform different tasks. The main functions are:

- Reconstruct 3D tracks
- Reconstruct 2D tracks in every single module
- Display events
- Perform a calibration based on reconstructed data
- Perform angular and translational module alignment
- Perform wire alignment
- Create plots to visualize data quality

The main functions as well as the algorithms on which they are based are described in detail in the next sections.

3.5.2 TDC Spectrum

The distribution of all TDC counts t_c is called TDC spectrum and is derived from cosmic data. Figure 3.9 shows a typical distribution of TDC values. To get a clean TDC spectrum, some cuts are applied to the raw data[6]:

- `3 < nhit < 10`
- `tdchit=0`
- `tdcwidth=3`

Drift time measurements from real hits only occur in a certain range of TDC channels. The upper boundary is influenced by the delay of the trigger signal as well as cable delays. The lower boundary then depends on the drift gas and the ambient conditions. The TDC boundaries are determined automatically from the data.

[6] For the meaning of the variables see Tab. 3.3.

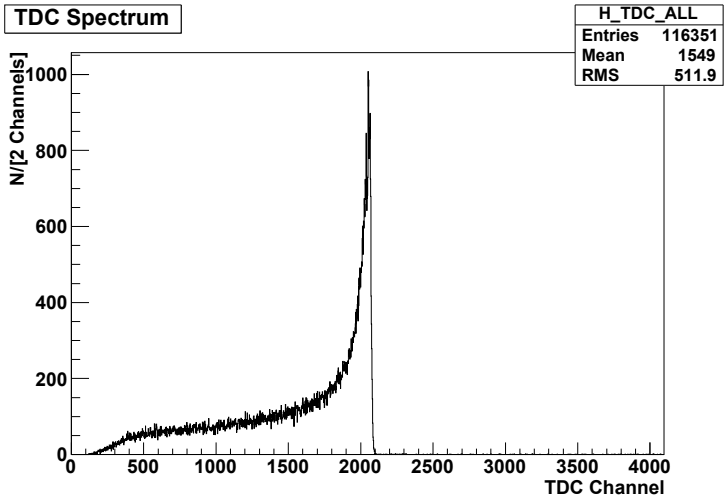

Figure 3.9: Initial TDC spectrum from raw data. Large TDC channels mean small drift distances. The steep edge around channel 2100 hence corresponds to hits near the anode wire.

First, the peak of the spectrum is located and its value n_m determined. For the upper boundary $t_{c,\max}$, all following channels are investigated. As soon as the average from three consecutive channels is below a certain number of entries n_l, the smallest channel is taken as the upper boundary. In an ideal case, n_l would just be zero. Since remaining noise cannot be excluded this limit has to be raised, especially for large data samples. For the determination of $t_{c,\max}$ it has been found useful to use $n_l = \frac{n_m}{900}$. The lower boundary is determined in a similar way, with the exception that four consecutive bins are considered. The boundaries are written to a root tree called `TBound`, which has two branches `min` and `max` and only one entry. The tree is saved in the file `calib.root`.

3.5.3 Initial Calibration

An initial calibration can be derived directly from the raw data. It can be assumed that random cosmic muon tracks are distributed homogeneously in space, i.e. taking into account a reasonable large number of tracks in a given drift tube all possible drift distances occur equally often. Thus, from the TDC spectrum, the TDC count to distance relation can be derived. TDC counts can be directly associated to drift distances. It is hence not necessary to convert TDC counts to *real* times. As described in Section 3.3, large TDC values mean small drift distances.

For a given TDC channel t_c with N_i entries, the distance r is hence given by

$$r(t_c) = r_{\max} \times \frac{\sum_{i=t_c}^{4095} N_i}{\sum_{i=0}^{4095} N_i} = r_{\max} \times \frac{\sum_{i=t_c}^{4095} N_i}{N_{\text{Entries}}}, \tag{3.3}$$

with $r_{\max} = 18.15\,\text{mm}$ being the inner tube radius. Fig. 3.10 shows the initial TDC count to distance relation.

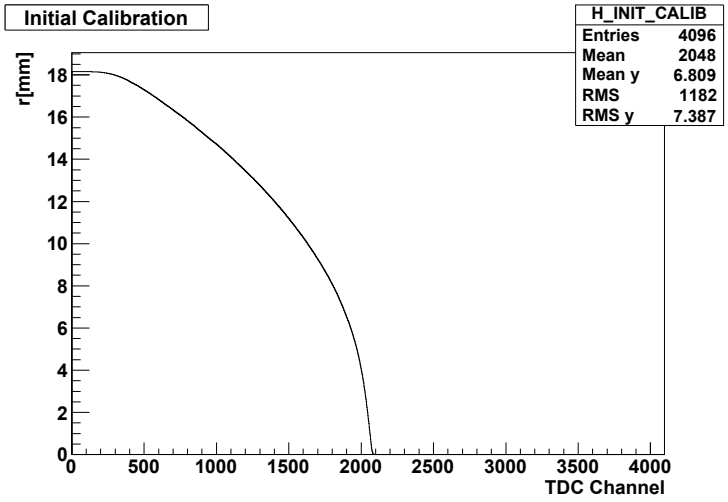

Figure 3.10: TDC count to distance relation after initial calibration.

During the initialization, the resolution function is set to 1 for all TDC bins, having the effect that all drift circles are treated equally during the first reconstruction.

The software `cmtrack` generates this initial calibration by calling `cmtrack -i`. The output is written to the file `calib.root`.

3.5.4 Track Parametrization

For the parametrization of muon tracks, the Hesse form

$$\xi \cos\alpha + \zeta \sin\alpha - p = 0 \tag{3.4}$$

is used [65]. The variables ξ and ζ are the coordinates of the according 2D plane, for the CMT setup these are either x and z or y and z. The parameter p describes the distance of the track to the origin and is always positive. α is the angle between the ξ axis and the tracks normal vector and can obtain values between 0 and 2π.

3.5.5 Pattern Recognition

Pattern recognition is done for each 2D-plane separately. All hits in the plane are taken into account. For an ideal event without any noise and just one particle crossing the detector, the track is described by a common tangent to all drift circles. Assume there are n_h hits in a plane. This results in

$$N_t = 4 \cdot \frac{n_h^2 - n_h}{2}$$

possible tangents, given by the number of possible combinations of two different drift circles times four possible tangents per pair of drift circles. The tangents are then investigated to find the one most probable to be the muon track. Tangents from drift circles in adjacent tubes are omitted to reduce the number of calculations. To

Table 3.5: List of variables calculated for each tangent

variable	definition
n_c	Number of common hits
n_m	Number of missing hits
n_r	Number of hits with residual below a certain threshold
n_t	Number of tubes passed by tangent
χ_p^2	Sum of quadratic residuals
l	The lever arm between the reference tubes
α	1^{st} Hesse parameter of track
p	2^{nd} Hesse parameter of track

find the muon track, a list of variables shown in Tab. 3.5 is determined for each investigated tangent. To be identified as a track, the tangent has to fulfill the following constraints:

- $n_r \geq 3$
- $n_t \geq 3$
- $\frac{n_r}{n_t} \geq 0.75$.

If more than one tangent fulfills these requirements, the one with the smallest $\chi_p^2/(n_r - 2)$ and the smallest n_m is chosen. Once the pattern has been recognized, the track is fitted, if n_c reaches a minimal number of hits which is set to $n_{c,\min} = 4$ by default.

3.5.6 Track Fit

The track fit is done via a χ^2 minimization. The χ^2 of a track is given by the sum of its quadratic residuals δ, which are given for each hit by the difference between the measured drift radius r and the calculated track distance to the wire d: $\delta = r(t_c) - d(\alpha, p)$, weighted by the resolution σ:

$$\chi^2 = \sum_{i=1}^{N} \frac{\delta_i^2}{\sigma_i^2} = \sum_{i=1}^{N} \frac{(r_i - |\xi_i \cos\alpha + \zeta_i \sin\alpha - p|)^2}{\sigma_i^2}. \tag{3.5}$$

ξ_i and ζ_i are the corresponding wire coordinates in the 2D-plane of each hit. All N hits identified by the pattern recognition are taken into account. To determine the minimal χ^2, the parameters α and p are combined to a vector $\vec{q}$:

$$\vec{q} = \begin{pmatrix} \alpha \\ p \end{pmatrix}.$$

For a minimum, one can thus demand:

$$\frac{\partial \chi^2}{\partial \vec{q}} = 0. \tag{3.6}$$

Defining

$$\vec{r} = \begin{pmatrix} r_1 \\ r_2 \\ \vdots \\ r_N \end{pmatrix}, \qquad \vec{d}(\vec{q}) = \begin{pmatrix} d_1 \\ d_2 \\ \vdots \\ d_N \end{pmatrix}, \qquad \text{and} \qquad V = \begin{pmatrix} \sigma_1^2 & 0 & \cdots & 0 \\ 0 & \sigma_2^2 & & \vdots \\ \vdots & & \ddots & 0 \\ 0 & \cdots & 0 & \sigma_N^2 \end{pmatrix},$$

χ^2 can be written as

$$\chi^2 = \left[\vec{r} - \vec{d}(\vec{q})\right]^T V^{-1} \left[\vec{r} - \vec{d}(\vec{q})\right]. \tag{3.7}$$

Since $\vec{d}(\vec{q})$ is not linear, an analytical minimization of χ^2 cannot be done. Instead, a Taylor expansion of $\vec{d}(\vec{q})$ is used:

$$\vec{d}(\vec{q}) \simeq \vec{d}(\vec{q}_0) + \sum_{i=1}^{2} \left(\left.\frac{\partial \vec{d}}{\partial q_i}\right|_{\vec{q}=\vec{q}_0} \cdot (q_i - q_{0,i}) \right) = \vec{d}(\vec{q}_0) + J(\vec{q} - \vec{q}_0)$$

with J being the $N \times 2$ Jacobian matrix of $\vec{d}(\vec{q})$ with

$$J_{\nu\mu} = \frac{\partial d_\mu}{\partial q_\nu}.$$

Eq. 3.7 can now be written as:

$$\begin{aligned} \chi^2 &= \left[\vec{r} - J\left(\vec{q} - \vec{q}_0\right) - \vec{d}(\vec{q}_0)\right]^T V^{-1} \left[\vec{r} - J\left(\vec{q} - \vec{q}_0\right) - \vec{d}(\vec{q}_0)\right] \\ &= \sum_{i=1}^{N} \frac{1}{\sigma_i^2} \left(r_i - \sum_{j=1}^{2} J_{ij}\left(q_j - q_{0,j}\right) - d_i(\vec{q}_0) \right)^2, \end{aligned}$$

and hence the derivative is given by

$$\begin{aligned} \frac{\partial \chi^2}{\partial q_\mu} &= -2 \sum_{i=1}^{N} \frac{1}{\sigma_i^2} J_{i\mu} \left(r_i - \sum_{j=1}^{2} J_{ij}\left(q_j - q_{0,j}\right) - d_i(\vec{q}_0) \right) \\ &= -2 \left[J^T V^{-1} \left[\vec{r} - J\left(\vec{q} - \vec{q}_0\right) - \vec{d}(\vec{q}_0)\right] \right]_\mu. \end{aligned}$$

Eq. 3.6 can now be written as

$$\frac{\partial \chi^2}{\partial \vec{q}} = -2 J^T V^{-1} \left[\vec{r} - J\left(\vec{q} - \vec{q}_0\right) - \vec{d}(\vec{q}_0)\right] = 0 \tag{3.8}$$

$$\Leftrightarrow J^T V^{-1} J(\vec{q} - \vec{q}_0) = J^T V^{-1} [\vec{r} - \vec{d}(\vec{q}_0)]. \tag{3.9}$$

Substituting $\vec{q} = \vec{q}_n$ and $\vec{q}_0 = \vec{q}_{n-1}$ one can now approximate the true parameter $\vec{q}$ through the iteration

$$\vec{q}_n = \vec{q}_{n-1} + \Delta\vec{q}$$

with $\Delta\vec{q} = \vec{q}_n - \vec{q}_{n-1}$. $\Delta\vec{q}$ can be derived from Eq. 3.9 as:

$$\Delta\vec{q} = \left(J^T V^{-1} J\right)^{-1} \left(J^T V^{-1} (\vec{r} - \vec{d}(\vec{q}_{n-1}))\right).$$

The Hesse parameters α and p from the pattern recognition are used as start parameters $\vec{q}_0$. Once the $\Delta\chi^2$ between two iterations drops below a certain limit, the fit is stopped. The error of the track parameters can be derived from the covariance matrix C which is given by [66]:

$$C(\vec{q}) = \left(J^T V^{-1} J\right)^{-1}.$$

After the fit was successful, a test is performed whether the residuals of all hits are below 3σ. Any hit exceeding this constraint is removed from the hit list and the fit procedure is redone. If less than 4 hits remain, the fit is aborted.

3.5.7 3D info

For each 2D-plane P_i, the track is reconstructed and its parameters in the planes reference system (ξ_i, ζ_i) are given in the Hesse Form:

$$\xi_i \cos\alpha_i + \zeta_i \sin\alpha_i - p_i = 0. \tag{3.10}$$

To obtain 3D track information, one has to transform this to the global reference system:

$$x\cos\alpha_0 + z\sin\alpha_0 - p_0 = 0 \tag{3.11}$$

$$y\cos\alpha_1 + z\sin\alpha_1 - p_1 = 0. \tag{3.12}$$

Each point of the track can thus be expressed in dependence of z as:

$$\begin{pmatrix} \frac{p_0 - z\sin\alpha_0}{\cos\alpha_0} \\ \frac{p_1 - z\sin\alpha_1}{\cos\alpha_1} \\ z \end{pmatrix} = \begin{pmatrix} \frac{p_0}{\cos\alpha_0} \\ \frac{p_1}{\cos\alpha_1} \\ 0 \end{pmatrix} + z \begin{pmatrix} -\tan\alpha_0 \\ -\tan\alpha_1 \\ 1 \end{pmatrix} \tag{3.13}$$

It is assumed that all muons come from above, that is traveling in the $(-z)$-direction. A direction vector $\vec{d}$ can thus be expressed as

$$\vec{d} = \begin{pmatrix} \tan\alpha_0 \\ \tan\alpha_1 \\ -1 \end{pmatrix}. \tag{3.14}$$

To obtain the polar angle θ, one can use the following correlation:

$$\vec{d} \cdot (-\vec{z}) = |\vec{d}| \cdot |\vec{z}| \cdot \cos\theta \tag{3.15}$$

where $\vec{z}$ is any vector pointing in z-direction. This leads to

$$z = \sqrt{\tan^2\alpha_0 + \tan^2\alpha_1 + 1} \cdot z \cdot \cos\theta \tag{3.16}$$

$$\theta = \cos^{-1}\left(\frac{1}{\sqrt{\tan^2\alpha_0 + \tan^2\alpha_1 + 1}}\right). \tag{3.17}$$

The azimuth angle φ is determined in a similar fashion. The projection of $\vec{d}$ in the (x, y)-plane is used:

$$\vec{d} \cdot \vec{x} = |\vec{d}| \cdot |\vec{x}| \cdot \cos\varphi \tag{3.18}$$

$$x \tan\alpha_0 = \sqrt{\tan^2\alpha_0 + \tan^2\alpha_1} \cdot x \cdot \cos\varphi \tag{3.19}$$

$$\varphi = \cos^{-1}\left(\frac{\tan\alpha_0}{\sqrt{\tan^2\alpha_0 + \tan^2\alpha_1}}\right). \tag{3.20}$$

The result for φ is ambiguous since $\cos^{-1}$ is only defined between 0 and π. This can be resolved by looking at the y-component of the direction vector $\vec{d}$:

$$\varphi = \begin{cases} \cos^{-1}\left(\dfrac{\tan\alpha_0}{\sqrt{\tan^2\alpha_0 + \tan^2\alpha_1}}\right) & \text{for } \tan\alpha_1 \geq 0 \\ 2\pi - \cos^{-1}\left(\dfrac{\tan\alpha_0}{\sqrt{\tan^2\alpha_0 + \tan^2\alpha_1}}\right) & \text{for } \tan\alpha_1 < 0. \end{cases} \tag{3.21}$$

Once the track could be successfully reconstructed, all relevant parameters are saved in the tree `TRecoData` in `reco.root`. For later calibration and wire alignment, most information is also stored for each hit separately. That way, certain parameters can be analyzed e.g. in dependence of the TDC value or a single wire. For a complete list of stored variables refer again to Tab. 3.3.

3.6 Alignment

Although the drift tube modules are manufactured with a high precision, the exact wire position still has an uncertainty in the order of 100 µm. Also, the relative position between two different modules is only measured with a limited precision. To obtain an even better track resolution, a software alignment is done. For this tracks that can be reconstructed in each module separately are used. For each module i, the parameters α_i and p_i from Eq. 3.4 are determined. Parameters from modules within the same plane are then compared. The alignment requires several steps. For each step, a new single module reconstruction has to be done, using already the alignment data from the previous steps.

3.6.1 Module Alignment

In a first step, the rotation between two modules is checked. The angular difference $\Delta\alpha = \alpha_1 - \alpha_0$ is calculated and its mean value $\overline{\Delta\alpha}$ is determined from a Gaussian fit as shown in Fig. 3.11. The position of the reference module 0 is left unchanged, whereas all wire positions of module 1 are now rotated by $\overline{\Delta\alpha}$ around its center:

$$\xi = \xi' \cos(\overline{\Delta\alpha}) - \zeta' \sin(\overline{\Delta\alpha})$$
$$\zeta = \xi' \sin(\overline{\Delta\alpha}) + \zeta' \cos(\overline{\Delta\alpha})$$

where ξ and ζ are the corrected coordinates within the module. The shifts for each wire are stored in `TAlign` in `align.root`.

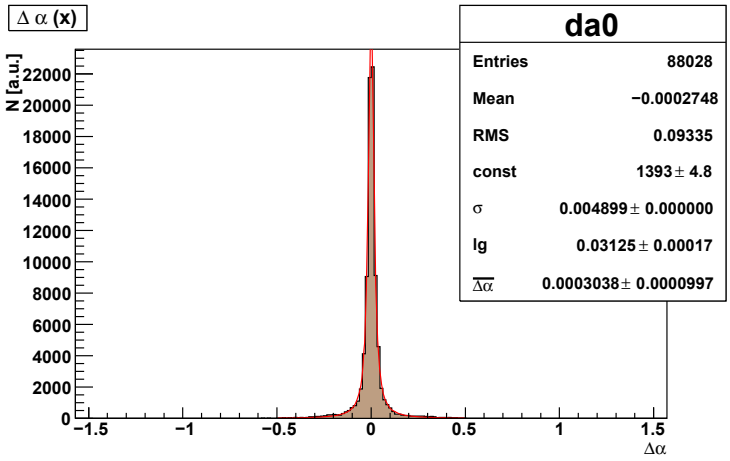

Figure 3.11: Angular alignment of the CMT. The plot shows the comparison of the Hesse parameter α for a single reconstruction of tracks in each of the two modules in the $x-z$-plane without any prior calibration. The distribution is fitted with a Voigtian (red). The mean value as well as the mean from the fit show a good angular alignment of the order of 0.3 mrad.

After the angular correction has been implemented, a possible translation of the modules is investigated. It is assumed that the position of module 1 is shifted by $\Delta\xi$ in ξ and $\Delta\zeta$ in ζ with respect to the true position. This shift is thus described as a shift of the assumed coordinate system $\xi' - \zeta'$ of module 1 with:

$$\xi' = \xi + \Delta\xi$$
$$\zeta' = \zeta + \Delta\zeta.$$

Comparing the same muon track in both modules leads to

$$\xi \cos\alpha_0 + \zeta \sin\alpha_0 - p_0 = \xi' \cos\alpha_1 + \zeta' \sin\alpha_1 - p_1,$$

and thus, assuming that α_0 and α_1 are equal, to

$$\Delta p = \Delta\xi \cos\alpha + \Delta\zeta \sin\alpha. \tag{3.22}$$

In reality α_0 and α_1 do not obtain the same value from the single fit. To obtain comparable tracks, the reconstruction is redone for the second plane with a fixed parameter $\alpha = \alpha_0$, leaving only one free parameter p_1.

$\Delta p = p_1 - p_0$ can now be determined from the single module reconstruction. Obtaining enough statistics allows to do a fit with free parameters $\Delta\xi$ and $\Delta\zeta$. The offset values found using this method are subtracted from the initial wire coordinates and the new positions are again stored in `TAlign`. An exemplary fit for real data is shown in Fig. 3.15 in Section 3.8.2.

3.6.2 Wire Alignment

Once the relative position of the modules is determined, the alignment is continued for the single anode wires. The reconstructed data from the full 2D-planes of the

detector is now used. Also, at least one calibration iteration should be done beforehand (cf. Section 3.7). For each wire the residuals δ as well as the information of the corresponding track α and p is considered. A possible systematic shift is investigated for all wires. For a wire at the coordinates ξ_w, ζ_w it is first checked, whether the track passed the tube above or below the wire. Therefore the ζ-coordinate of the track at ξ_w is calculated:

$$\zeta(\xi_w) = \frac{p - \xi_w \cos\alpha}{\sin\alpha}.$$

Now the ξ and ζ projections of the residual δ need to be determined. Due to the definition of the Hesse form, the angle α cannot be used directly for this task, but is transformed to an angle β between the $\zeta_w = 0$ axis and the normal vector of the track through the wire coordinates. For $\zeta(\xi_w) - \zeta_w \geq 0$, β simply reduces to α if $\alpha \leq \pi$ and $\alpha - \pi$ if $\alpha > \pi$. In the case of $\zeta(\xi_w) - \zeta_w < 0$, β is given by α if $\alpha > \pi$ and $\alpha + \pi$ if $\alpha \leq \pi$. A possible shift $\Delta\xi$ and $\Delta\zeta$ of the wire is then given by:

$$\Delta\xi = -\delta\cos\beta$$
$$\Delta\zeta = -\delta\sin\beta.$$

This procedure is done for all wires and all hits of the alignment run, conveniently stored in `TAnaData`. Finally, one obtains distributions of $\Delta\xi$ and $\Delta\zeta$ for each wire which have a peak around the true shift of the coordinates. These are fitted by a Gaussian and the wire positions are corrected by the mean value.

3.7 Calibration

Although a fairly good reconstruction is already possible after the initial calibration described in Section 3.5.3, the TDC count to distance relation can still be improved through further calibration steps. The initial calibration is based on the assumption that the electron avalanche causing the signal starts at the point of the track where the distance to the anode wire is shortest. This idealization is not correct. When the particle crosses the tube, clusters of ionized molecules build up. These clusters are not homogeneously distributed along the track. Therefore the nearest ionization cluster does not necessarily lie closest to the anode wire, the measured drift circle can thus be overestimated by this effect. The drift times are also effected by diffusion of the drifting electrons. Multiple scattering within the drift gas can deflect the electrons from the direct track to the anode wire thus prolonging the drift time. These effects, together with uncertainties in both the exact wire positions and the drift time measurement, are the reason why the initial calibration needs to be corrected. This is done using the reconstructed data itself. Also, the resolution function can be determined from this. It is assumed that the reconstructed tracks are indeed the true muon tracks. Hence, the TDC count to distance relation can be derived for each hit of a wire at the position (ξ_i, ζ_i) by the reconstructed distance $d = \xi_i\cos\alpha + \zeta_i\sin\alpha - p$ for the corresponding TDC count t_c. The distribution of all calculated distances in dependence of the TDC value can be directly obtained form `TAnaData`.

To calculate the new TDC count to distance relation, all pairs of TDC value and distance are drawn in a scatter plot as depicted in Fig. 3.12. The mean value

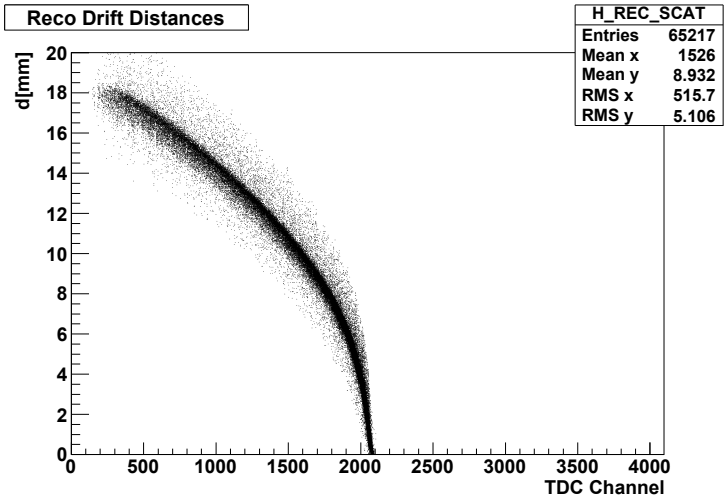

Figure 3.12: Scatter plot of calculated drift distances d. During calibration the mean value of d in a given tdc bin gives the corrected drift radius r for that tdc count.

of the calculated distances in each TDC value bin gives the corrected TDC count to distance relation value. However, for large drift circles, this method suffers from relatively low statistics per bin. To obtain better results, both a time and space based binning is used. For each bin, both histograms are then fitted by a 3^{rd} degree polynomial in the region around the bin. For small TDC values, the result from the space binned fit is used as the new TDC count to distance relation value, whereas for large TDC values the parameter obtained from the time binned histogram is used.

For each TDC bin, the distribution of residuals can be taken into account to obtain the resolution function. However, one has to take into account, that the reconstructed track might still have some errors and represents merely an approximation of the true track. This is resolved by correcting each residual by a factor $\sqrt{\frac{n_{\text{hits}}}{n_{\text{dof}}}}$. The fit has two free parameters, hence n_{dof} is simply given by $n_{\text{hits}} - 2$. All corrected values are filled into a histogram which is then fitted by a Gaussian. The resolution for the corresponding bin can then be derived from the σ of the fit.

3.8 Commissioning: Muons in Hamburg

The original purpose of the CMT was a three dimensional tracking of cosmic muons. After commissioning, the tracker was used to investigate cosmic muons in the laboratory in Hamburg. The location of the laboratory is slightly above sea level. To test the functionality of the detector, reconstructed tracks have been compared to a Monte Carlo simulation based on the muon distribution at sea level. The results are presented in the next sections, followed by a brief look at the overall quality of the data analysis and the resolution achieved by the detector.

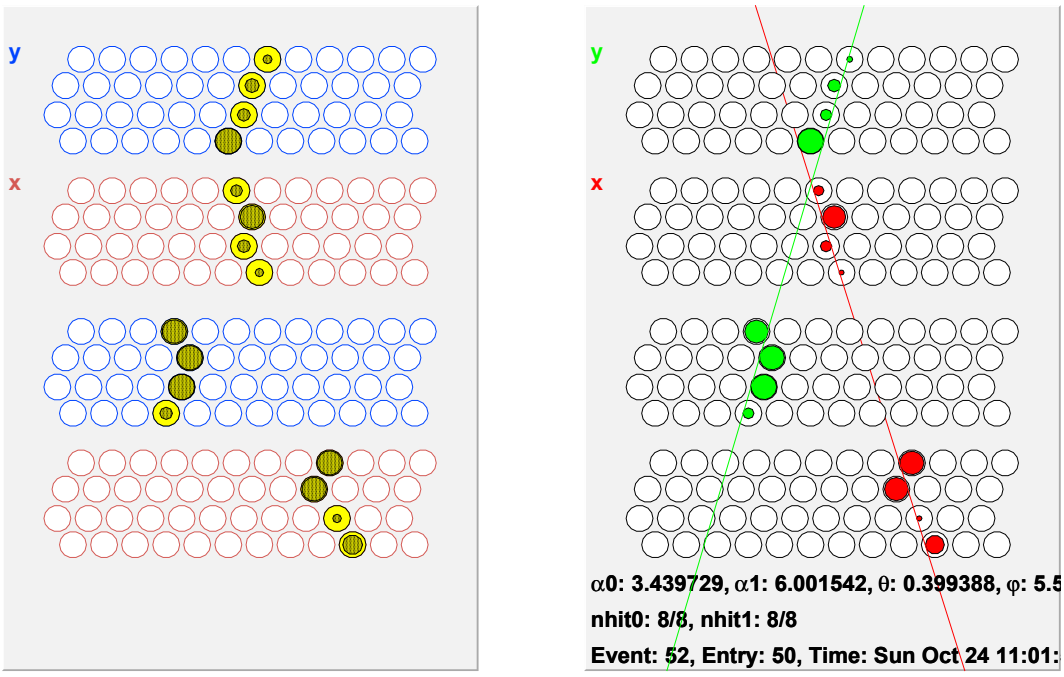

Figure 3.13: Left: quasi online display of a muon event (Event 52 from RUN_063_18-33-59). A hit tube is filled with a color indicating the signal width, yellow meaning width=3. The solid circles correspond to the drift times. Right: the same event after reconstruction. Different colors indicate the different 2D-planes. The event time in the display is not correct since the data was taken before the modification of the clock emulation data to UNIX time (cf. Section 3.3).

3.8.1 Monte Carlo Studies

At sea level, the angular distribution of muons is proportional to $\cos^2\theta$, where θ is the polar angle [33]. However, the muon tracker only has a limited angular acceptance. To be able to compare measurements to the expectations a Monte Carlo study has been performed. Muons are generated at a fixed height $z = 220\,\text{mm}$. This is where the top scintillators are located. For each event four values are randomly generated:

- x linear between -500 mm and 500 mm
- y linear between -500 mm and 500 mm
- φ linear between 0 and 2π
- θ according to a $\cos^2$ distribution between 0 and $\frac{\pi}{2}$.

The generation of θ is not straightforward since the random number generator only returns homogeneously distributed values between 0 and 1. Therefore, θ has to be derived from this distribution. One also has to take into account that due to the solid angle each value θ has to be weighted by $\sin\theta$. A random number r has to

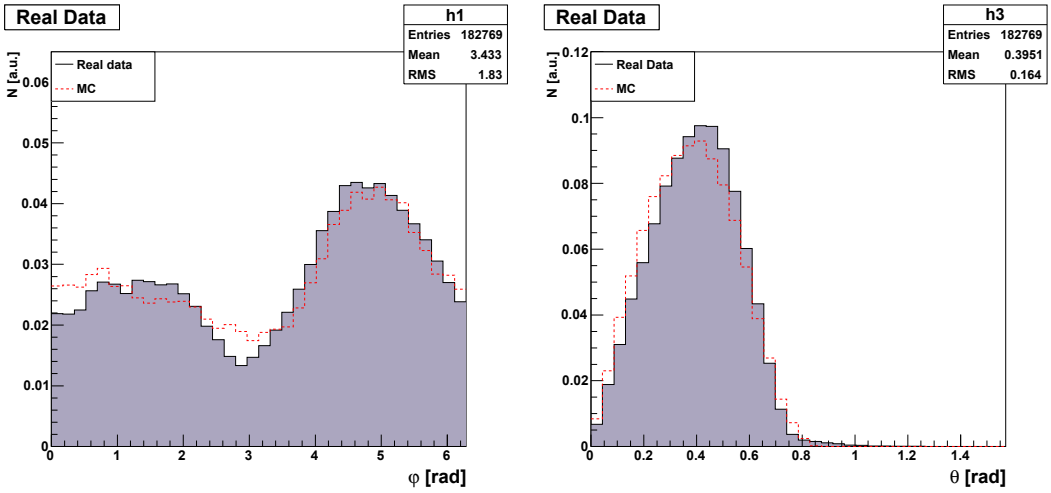

Figure 3.14: Comparison of reconstructed and Monte Carlo (MC) cosmic data. The left figure shows the azimuth angular distribution. The two distinct peaks arise form the non symmetrical setup of the trigger scintillators, the difference in their height from a parallel shift. The right picture shows the polar distribution. The data is in good agreement with the simulation. However, small discrepancies remain, arising from small uncertainties in the exact trigger positions and the fit.

fulfill the following condition:

$$r(\theta) = \frac{\int_0^{\theta} d\vartheta \sin\vartheta \cos^2\vartheta}{\int_0^{\frac{\pi}{2}} d\vartheta \sin\vartheta \cos^2\vartheta} = 1 - \cos^3\theta.$$

Therefore θ is given by

$$\theta = \cos^{-1} \sqrt[3]{1-r}.$$

Once all parameters have been generated, it is checked whether the resulting track would go through at least one scintillator layer above and below the detector. If this is the case, the event is considered *triggered*. Now the number of hit tubes is calculated. The event is saved to a tree with the same data structure as `TData`, extended by the simulated coordinates of the track.

Fig. 3.14 shows a comparison of both the azimuth and zenith angular distributions of reconstructed real data with the Monte Carlo simulation. In general, the data is in good agreement with the simulation. However, some small discrepancies can be noted. In the azimuth distribution, two distinct peaks can be observed. They result mainly from the trigger scintillator setup. Whereas the scintillators were crossed on top of the detector, they were placed parallel underneath, thus leaving a preferred direction for tracks along the y axis. This corresponds to values of φ around π and $\frac{3\pi}{2}$. This alone still does not explain why one of the peaks is slightly larger than the other. The relative heights of the peaks are very sensitive to the exact positions of the trigger scintillators. When the upper scintillators get shifted

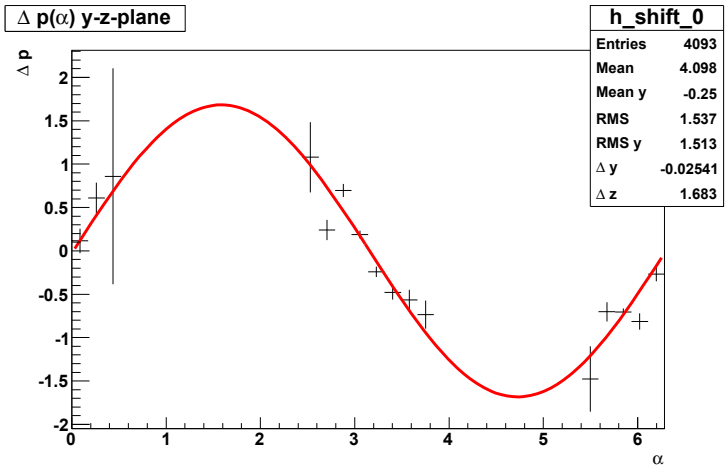

Figure 3.15: The difference Δp from the single module reconstruction in the $y-z$ plane in dependence of α. The red line is a fit to Eq. 3.22 with $\xi = y$ and $\zeta = z$. The data was obtained performing only the initial calibration. Hence the data shows still some uncertainties. However, a systematic shift, mainly in z, can already be observed. This is expected, because the mechanical alignment could be done with a much higher precision in x using a plumb.

in y, muons coming from the direction the scintillator was shifted to are favored with respect to tracks in the reverse direction. The same is true for shifts in x. This also explains the small disagreements between the Monte Carlo simulation and the real data: Unfortunately, the scintillator positions have not been measured precisely enough. The uncertainties in their position accounts for the offset between the data and the simulation.

3.8.2 Cosmic Data

Cosmic muons have been tracked and reconstructed with the CMT in the laboratory in Hamburg. Fig. 3.13 shows the event display of an event before and after reconstruction. The results presented in this chapter are based on a data sample with 284605 events taken on March 4^{th} 2009. The data has been processed as described in the previous section. First, a reconstruction for every single module was performed. Based on this data an angular alignment could be done. Fig. 3.11 shows the angular differences exemplary for the two modules in the $x-z$-plane. Without any prior alignment, the angular differences are quite small which shows the precise mechanical angular alignment of the modules.

In the next step, a possible shift of the modules was investigated. Fig. 3.15 shows $\Delta p(\alpha)$ for the two modules in the $y-z$-plane. A fit to Eq. 3.22 as described in Section 3.6.1 shows a negligible offset in the horizontal direction. However, an offset of $\Delta z = 1.683\,\text{mm}$ is found. This does not surprise, since the modules were aligned merely using a level and a plumb. This method is fairly precise for the angular as well as the horizontal alignment. The vertical position was measured with a simple folding rule, hence higher uncertainties are expected.

The module positions have been corrected as described in Section 3.6 and the

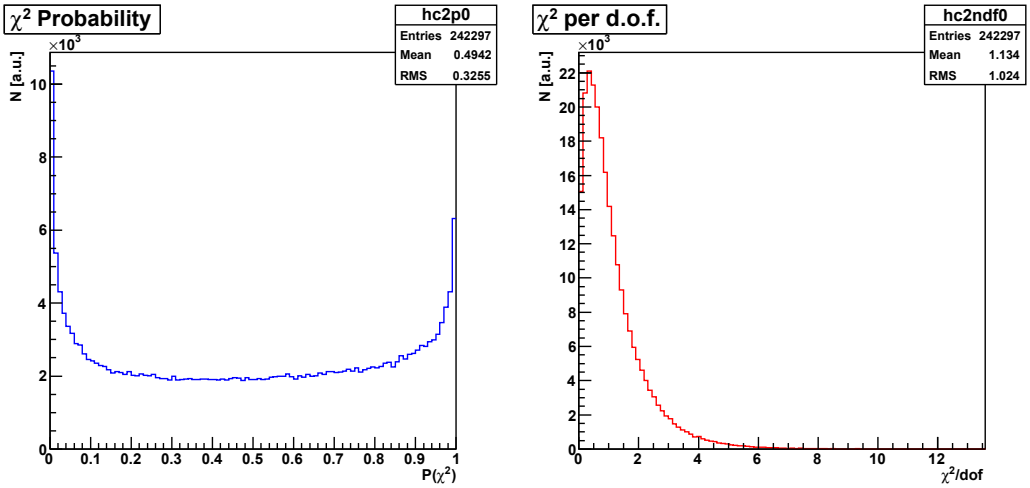

Figure 3.16: The fit quality is checked by a look at the χ^2 distributions. Left: the χ^2-probability shows a flat distribution as expected, with only a slight rise in the side regions. Right: the χ^2 per degrees of freedom has a mean value close to 1.

calibration was performed. Altogether 182728 events could be reconstructed. The angular distributions of reconstructed tracks were already presented in Fig. 3.14. They show the expected behavior. The quality of the reconstruction was checked as presented in the following section.

3.8.3 Fit Quality

As described in Section 3.5.6, the track fit is done using a χ^2-minimization. The quality of the fit can be controlled by inspecting the distribution of χ^2 per degrees of freedom. The mean value of this χ^2-distribution should be close to 1. Also, the χ^2-probability can be used to investigate the fit quality. For a given number of degrees of freedom and a given χ^2, the probability can be calculated, their distribution should be homogeneous between 0 and 1. Fig. 3.16 shows the χ^2-distribution and the χ^2/dof for real data. The χ^2-distribution shows the desired behavior except for the side regions. The excesses at zero and one can be explained by tracks that were reconstructed wrongly. This can be either due to a wrong pattern recognition (excess at zero) or a too good fit on *fake* drift circles, e.g. from δ electrons or cross talk (excess at one). However, the mean value of χ^2/dof shows the expected mean value around 1.

If statistics are high enough, the calculated drift distances to the fitted track should be distributed homogeneously between 0 and the tube radius (18.15 mm). Fig. 3.17 shows this distribution. Besides a small discrepancy for very small drift circles it is in good agreement with the expectation. This can be easily understood by looking again at the TDC count to distance relation. For small drift distances, the TDC count to distance relation rises very steeply, meaning that a small deviation in the drift time has a large effect on the drift radius. Hence, small uncertainties occur in this region. Since no negative drift distance can occur, the drift distance is much likely to be overestimated in this region. This can be recognized by the

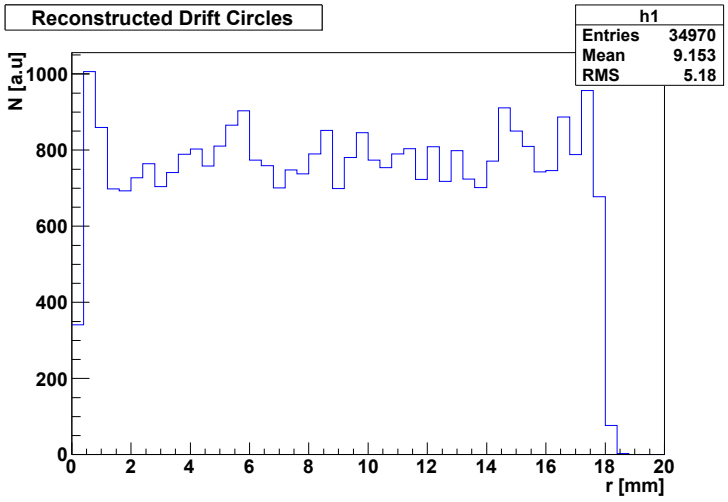

Figure 3.17: Distribution of radii r from reconstructed drift distances. The radii are distributed homogeneously except for the region around the center. This is due to the large uncertainties of the TDC count to distance relation in this region.

small peak in the second bin of the distribution. However, the overall performance is satisfactory.

3.8.4 Spatial and Angular Resolution

Both the spatial and angular resolutions can be determined from the reconstructed data. Fig. 3.18 shows the distribution of residuals from all fitted tracks. The RMS value gives a measure for the lateral resolution σ_r of the detector. It has been found to be $\sigma_r = 270\,\mu\text{m}$. The angular resolution can be determined by comparing tracks reconstructed in each single module. For a perfect reconstruction, the fitted angles α should be identical for all modules. However, comparing the angles for tracks of the same event reconstructed in two modules of the same 2D plane separately shows slight differences. The distribution of $\Delta\alpha$ for real data is shown in Fig. 3.19. A sharp peak around zero is observed. To obtain a measure for the resolution, a Voigtian was fitted to the distribution. A Voigtian is a convolution of a Gaussian and a Breit-Wigner distribution. The σ of the fit is then obtained from the FWHM divided by 2.35. For the CMT, a value of $\sigma_{\text{fit}} = 6.98\,\text{mrad}$ has been found. Since two modules are taken into account, the error of the reconstructed angle is taken into account twice. It is therefore overestimated in the direct comparison. This effect can be compensated for, by dividing σ by $\sqrt{2}$. Consequently the angular resolution σ_α is given by:

$$\sigma_\alpha = \frac{\sigma_{\text{fit}}}{\sqrt{2}} = 4.65\,\text{mrad}.$$

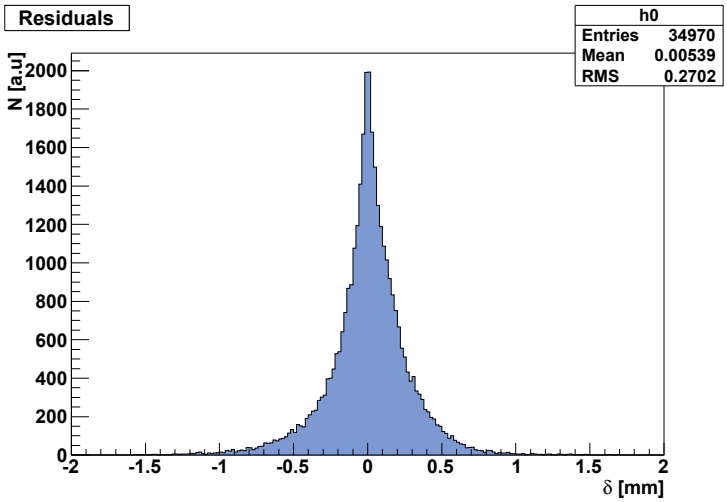

Figure 3.18: Distribution of residuals δ. The RMS gives a measure of the spatial resolution.

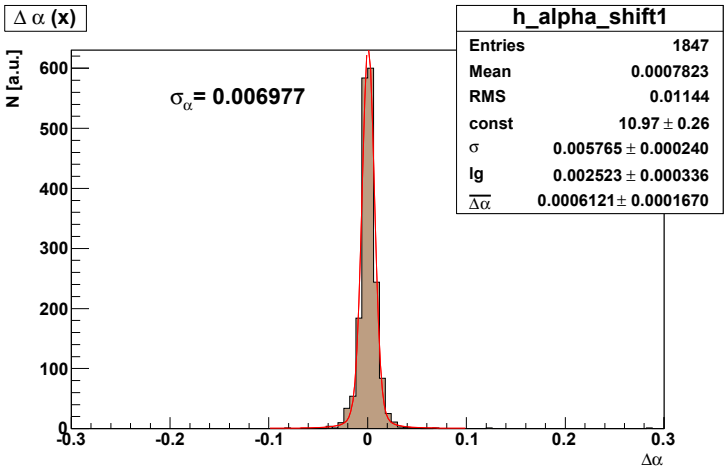

Figure 3.19: Determination of the angular resolution of the CMT. The plot shows the distribution of differences of the Hesse parameter α from a separate reconstruction of two parallel modules. A clear peak around 0 can be seen. The width of the distribution gives a measure of the angular resolution and has been determined by a fit to a Voigtian.

Chapter 4

The Borexino Experiment

The Borexino Experiment was designed for the real time spectroscopic detection of solar neutrinos. Its main goal is the measurement of ^{7}Be neutrino flux, but also ^{8}B, *pep* and CNO solar neutrinos belong to the scientific program. Apart from solar neutrinos, also geo-neutrinos have been observed recently. The detector is located underneath approximately 1400 m of rock overburden ($\approx$ 3800 m.w.e.[1]) in the LNGS underground laboratory in Italy. The detection of neutrinos is done using liquid scintillator and the experiment is surrounded by ultra pure water acting as a Čerenkov muon veto. Detecting low energetic neutrinos at low rates requires a high radio purity of all materials involved—especially the scintillator—which has been achieved for Borexino. This chapter gives an overview of the detection methods of neutrinos in liquid scintillators, especially in Borexino. A description of the detector design is then given. It is followed by a discussion of background sources. Special care is given to the cosmogenic background in the scintillator and how it can be accounted for. In the last section of this chapter the results so far obtained by Borexino are presented.

4.1 Neutrino Detection in Borexino

Borexino uses liquid scintillator for the detection of low energetic neutrinos. The scintillator acts as both target and detection material. Neutrinos react with the scintillator through different processes. Neutrinos—electron type neutrinos ν_e in particular—can be detected through elastic scattering whereas anti-electron-neutrinos can be detected via the inverse β decay. During both processes, energy is deposited in the scintillator which can be detected by the scintillation light. Both processes are described in detail below.

4.1.1 Elastic Scattering in Liquid Scintillator

The elastic scattering of neutrinos on electrons in the scintillator is the dominant process for the detection of solar neutrinos. The scattering process

$$\nu_e + e^- \rightarrow \nu_e + e^- \tag{4.1}$$

[1] m.w.e. meter water equivalent

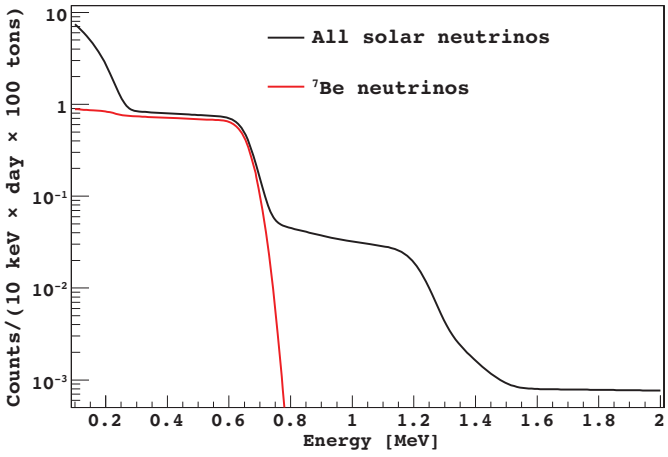

Figure 4.1: Expected spectrum of solar neutrinos in Borexino. Clearly the Compton-like edge from the ^{7}Be neutrinos can be seen at approximately 665 keV. Figure from [67].

leaves a recoil electron which deposits its energy in the scintillator. The resulting light output is observed by photo multipliers. The energy transfer from the neutrino to the electron is similar to that of a photon in a Compton scattering process. Thus, monochromatic neutrinos like the ^{7}Be neutrinos from the Sun (cf. Section 2.3) leave a characteristic shoulder in the energy spectrum. The expected spectrum for solar neutrinos is depicted in Fig. 4.1. Monoenergetic 0.862 MeV ^{7}Be neutrinos from the Sun are expected to show a Compton-like edge in the recoil electron's energy spectrum at 665 keV. As the reaction has no energy threshold, it is particularly well suited for the detection of low energetic neutrinos. The scattering process is sensitive to all neutrino types ν_e, ν_μ, and ν_τ, however, due to the possibility of both a CC and NC reaction, the cross section for electron type neutrinos is approximately six times higher than for other neutrinos which can only interact with ordinary matter by the exchange of a Z boson. Fig. 4.2 shows the Feynman diagrams of the neutrino scattering processes on electrons in the scintillator. As already mentioned above, the energy transfer from the neutrino to the electron is Compton like. Scattered electrons then lose their energy to the scintillator through excitation of its molecules. Under emission of photons, these molecules then de-excite again within a few nanoseconds. The photons' energy typically lies near the ultra violet region. A wavelength shifter is added in small amounts to the scintillator. It absorbs photons from the initial scintillation process but re-emits at a longer wavelength. This assures the scintillation light to travel through the detector without being re-absorbed.

The number of produced photons depends on the energy deposited in the scintillator. Organic scintillators typically produce approximately 10^4 photons per 1 MeV of deposited energy. Hence, the number of photo electrons (p.e.) detected by the PMTs gives a measure of the energy deposited in the scintillator. The number of p.e. can be calibrated to the according energy using radioactive sources of known energy. Once the detector is calibrated, a spectroscopic measurement of the scattered

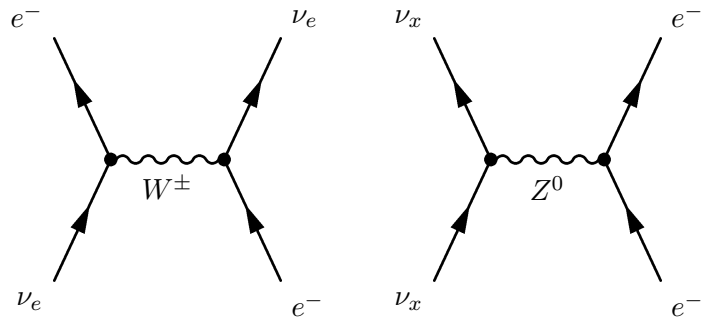

(a) CC elastic scattering (b) NC elastic scattering

Figure 4.2: Elastic scattering of neutrinos in matter. The cross section is six times higher for ν_e than for the other neutrino types due to the CC reaction.

neutrinos is possible.

Elastic scattering of neutrinos is also possible on protons. However, due to the relatively large proton mass, the transferred energy is much smaller than in the electron's case. Nevertheless, this reaction is of interest in the case of high energetic ν_x e.g. from super-nova explosions.

4.1.2 Inverse β Decay

The main reaction channel for anti electron type neutrinos is the inverse β decay on protons:

$$\bar{\nu}_e + p \rightarrow e^+ + n. \tag{4.2}$$

The $\bar{\nu}_e$ is captured by a proton under the emission of both a neutron and a positron. This process can be identified by the coincidence signal from the positron annihilation and the delayed neutron capture. It leaves a distinct signature which can be easily identified: the positron carries away most of the reaction's energy. It annihilates almost immediately thus producing a prompt signal from which the event time and the neutrino's energy can be deduced. The second signal occurs when the free neutron is captured. This typically happens after 250 µs on a free proton and is accompanied by the release of a photon of 2.2 MeV which corresponds to the deuteron's binding energy. This coincidence signal of a distinct energy is a strong indicator of an inverse β decay.

The energy threshold for the reaction can be derived easily using energy conservation by looking at the masses m_x of the particles involved:

$$E_{\nu,\mathrm{min}} = \frac{(m_n + m_e)^2 - m_p^2}{2m_p} = 1.806\,\mathrm{MeV}.$$

Anti electron neutrinos below this threshold cannot be detected. The energy E_{prompt} released in the prompt annihilation of the positron is directly connected to the incoming neutrino's energy: $E_{\mathrm{prompt}} = E_{\bar{\nu}_e} - 0.782\,\mathrm{MeV}$.

4.1.3 Čerenkov Light

Čerenkov detectors are well suited for the detection of high energetic charged particles. Relativistic particles traveling through a medium with refractive index n at a speed faster than the speed of light within this medium ($\beta \geq \frac{c}{n}$) generate light in a conical shape. It is emitted at an angle α

$$\cos\alpha = \frac{1}{\beta n}.$$

Since only particles with high velocities produce Čerenkov radiation, such a detector can only be used for high energetic particles. Applying photo multipliers around the detection volume allows to observe the Čerenkov light. A particle whose track is contained in the target can be identified by a light ring whereas a passing particle produces a disk like shape. Shape and dimensions of these structures can be used to obtain information on the direction and energy of the particle. The Borexino experiment is surrounded by a large water tank acting both as a passive shielding against external background sources as well as a Čerenkov veto for cosmic muons. The signals recorded in this tank are also used for muon tracking. Čerenkov light is not only emitted in the water tank, it also occurs when high energetic particles like cosmic muons cross the scintillator.

4.1.4 Background in Liquid Scintillator Detectors

Elastic scattering and inverse β decay offer excellent detection methods of low energetic neutrinos in liquid scintillators. Unfortunately, their signatures can be mimicked by different sources of background. These originate either from radioactive contaminations within the scintillator or the surrounding materials, or they are caused by external radiation penetrating the detector.

The dominating internal background source is ^{14}C which is intrinsic to the scintillator. ^{14}C decays through a β^- decay and has a half-life of 5730 years. Its natural abundance on earth is of the order of 10^{-12}. The β^- decay has an end point energy of 156.475 keV. Despite the small abundance of ^{14}C, neutrino detection below this threshold is not possible.

The decay of ^{14}C is not the only challenge when building a liquid scintillator detector. Since it is virtually impossible to create a 100% pure scintillator, all background created by natural radioactivity and the abundances of radioactive elements have to be understood and effectively reduced. The main internal background sources besides ^{14}C are ^{238}U, ^{232}Th and ^{40}K as well as ^{222}Rn and its daughters. Furthermore, muons from the cosmic radiation create radionuclides by spallation processes with long half-lives. Despite the Čerenkov muon veto, the decay of these radionclides cannot be simply vetoed since they occur long after the incident particle has passed the detector. Due to the statistic process of radioactive decays, the time after which the decay takes place cannot be directly correlated to the muon. The most prominet example for this cosmogenic background in liquid scintillator is the production of ^{11}C, which is a β^+ emitter with a half-life of approximately 20 minutes. As will be shown in Section 4.3, a high radio purity has been achieved for Borexino. It will also be shown how cosmogenic events can mostly be controlled.

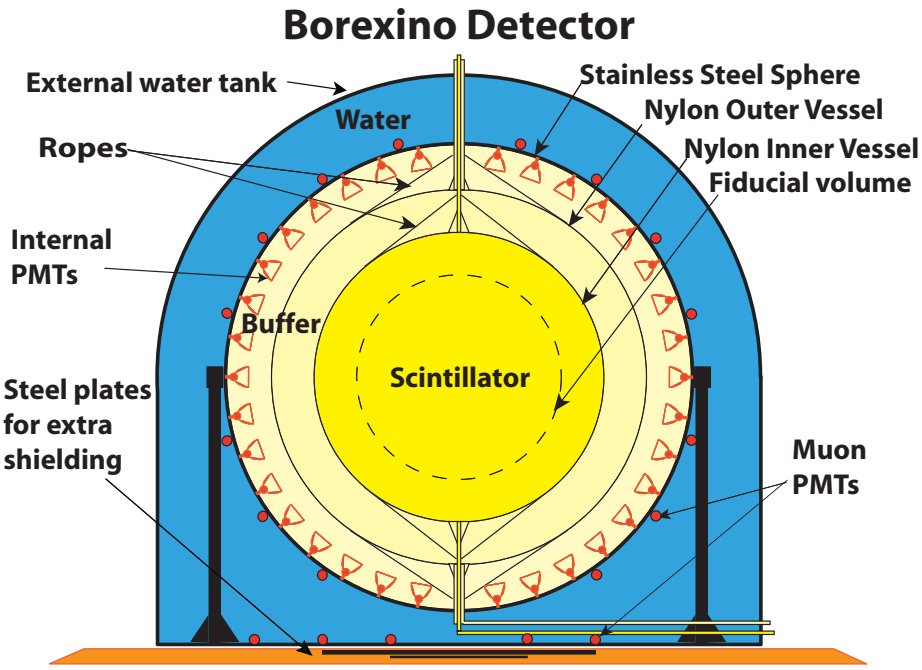

Figure 4.3: Onion-like structure of Borexino (Figure from [68]). The target scintillator is located in the center. It is surrounded by two layers of non scintillating buffer liquid, shielding the target from external background sources. The scintillator and the first buffer layer are each contained in a thin nylon sphere. Both the buffer and the scintillator are located inside a stainless steel sphere (SSS) equipped with 2212 inward facing PMTs to measure the scintillation light. This inner detector is shielded by an external water tank serving as both a passive shielding and an active Čerenkov veto. 208 additional PMTs mounted on the outer SSS and the bottom of this outer detector are able to detect the Čerenkov light.

4.2 The Borexino Detector

The Borexino detector applies the detection methods described above. Located in Hall C of the LNGS underground laboratory between L'Aquila and Teramo in the Abruzzo region in Italy, its central volume hosts 278 tons of liquid scintillator mainly for the detection of solar neutrinos. In this section, an overview of the Borexino detector is given. The setup of the detector, the used scintillator and the radio purity are discussed.

4.2.1 Detector Setup

The Borexino detector is built in an onion-like structure as depicted in Fig. 4.3. Each layer serves as an effective shielding of external radio contaminations. Enclosed in a spherical nylon vessel, the target scintillator is located in the center of the detector. This inner vessel (IV) has a diameter of 8.5 m, is 125 µm thick and contains 278 tons of scintillator.

The IV is surrounded by two concentric layers of buffer liquid. The layers are 2.6 m thick altogether and divided by another nylon vessel at a radius of 5.5 m. The two buffer layers contain 323 and 567 tons of scintillator, respectively. The outer nylon vessel (OV) acts as a barrier for external backgrounds, mainly ^{222}Rn emanated from the PMTs and other external parts of the detector.

Both nylon vessels are attached to a stainless steel sphere (SSS) by nylon ropes. The sphere has a diameter of 13.7 m and separates the inner detector (ID) from the outer detector (OD).

2212 8" ETL-9351 photo multipliers are mounted inside the stainless steel sphere of which 1828 are equipped with light concentrators. This increases not only the total coverage of the active region but also rejects photons coming from the buffer.

The outer detector consists of a tank around the SSS and is filled with 2.4 kilotons of ultra pure water. It acts as a Čerenkov veto for cosmic muons and provides an additional passive shielding. The tank is 16.9 m high and has a radius of 9 m. 208 PMTs of the same type as used for the ID are mounted on the outside on the stainless steel sphere and on the bottom of the tank to detect Čerenkov light produced by cosmic muons.

4.2.2 Scintillator

The scintillator was chosen taking into account both the the required radio purity and optical properties. It consists of the organic scintillator Pseudocumene (PC, 1,2,3-trimethylbenzene) with an admixture of ∼1.5 g/l PPO (2,5-diphenyloxazole) for wavelength shifting. The PC and PPO mixture has a light yield of $\approx 10^4$ photons per MeV of deposited energy and an attenuation length of 8 m. Its emission spectrum has a peak at 360 nm which lies close to the region of maximal efficiency of the PMTs. Altogether a light collection of $\simeq$ 500 photons/MeV is reached with the setup. The scintillator has a good time response and energy resolution. The decay time for the scintillation is approximately 3 nanoseconds and the energy resolution is found to be $\simeq 5\%$ at 1 MeV. The time response is crucial for a position reconstruction of events in the scintillator, as well as for the discrimination between events from α and β

decays which usually show a different time profile of the emitted light in organic scintillators. A detailed description of the scintillator can be found in [68].

High transparency and similar optical properties to those of the scintillator are desired for the Buffer. However, it should not produce a lot of scintillation light by itself. The buffer is also based on PC. This has the advantage that the density of the fluids are equal and no buoyancy forces occur inside the nylon vessels. About 5 g/l of dimethylphtalate (DMP) is added to the PC as a light quencher to prevent gammas emanating from the PMTs from reaching the target and to further suppress scintillation processes in the buffer thus acting as a passive shielding. This way, the outer vessel (OV) allows scintillation light originating inside the target area to travel through without generating a lot of signals itself. The buffer is divided into two parts by the second nylon vessel. This acts as a barrier mainly for radon emmanating from the PMTs.

4.2.3 Radio Purity

A high radio purity is essential for detecting low energetic neutrinos in Borexino. Borexino expects a rate of the order of a few ten counts per day for 100 tons of liquid scintillator from the interaction of sub-MeV solar neutrinos above 200 keV. This corresponds to an equivalent activity of the order of 10^{-9} Bq/kg. Radioactive background within the scintillator mainly occurs from the decays of ^{238}U and ^{232}Th daughters as well as ^{40}K. Also, nitrogen used to remove oxygen from the scintillator is contaminated, mainly with noble gases like ^{222}Rn, ^{39}Ar and ^{85}Kr. The goal was to reduce the abundances of radioactive contaminants to a level where the rate of their decays is well below the expected neutrino rate. Namely, this corresponds to required abundances of $< 10^{-16}$ g/g for ^{238}U and ^{232}Th and $< 10^{-14}$ g/g of ^{40}K within the scintillator. Nitrogen used to flush the detector has to provide a radio purity of 0.36 ppm for Ar and 0.16 ppt for Kr, corresponding to approximately 1 count per day in the detector. This limit is also set for events caused by external γ radiation [68].

The actual cleanliness of the scintillator even surpasses these requirements. The abundances for ^{238}U have been found to be $(1.6 \pm 0.1) \times 10^{-17}$ g/g, those of ^{232}Th have been measured as $(6.8 \pm 1.3) \times 10^{-18}$ g/g [69]. However, even small abundances of radioactive elements have to be considered. Their contribution and ways to treat them are presented in the next section.

4.3 Background

In a low rate experiment like Borexino, a special care has to be given to all sources of background. Background for neutrino events mainly occurs from two sources: natural radioactivity and cosmic radiation. The background signals can disturb the neutrino measurements in two ways: On the one hand, decays with Q values of the order of the neutrinos energy mimic neutrino events and therefore distort the measurement, and on the other hand, if the background events exceed a certain rate, the detector is blinded. The effect of radioactive decays can be minimized by obtaining a high radio purity of all materials involved and by having an effective shielding against all external radiation. The flux from cosmic radiation, especially

muons, is reduced by going deep underground. However, a complete shielding against background is not possible and it has thus to be studied thoroughly. This section gives a brief overview of background sources in Borexino and describes how they can be discriminated. Special care is given to the uncorrelated cosmogenic background induced by muons.

4.3.1 Radioactivity

Natural radioactive elements are intrinsic to both the scintillator and the surrounding materials. The most prominent background source in Borexino is the natural abundance of ^{14}C in organic materials and hence in the scintillator. At the Earth's surface, a ^{14}C has a relative abundance to ^{12}C of approximately 1.2×10^{-12} g/g. However, this concentration is already significantly reduced due to the fact that the scintillator is based on a mineral oil that has been formed underneath the Earth's surface during a long time compared to the ^{14}C half-life of 5730 years. In Borexino a ^{14}C cleanliness of the order of 10^{-18} compared to ^{12}C has been reached, resulting in a rate of 3.5×10^4 counts per day and ton. While decays of ^{14}C limit the detection of neutrinos to energies above the ^{14}C end point energy of ∼156 keV, their number is reduced sufficiently to not constantly blind the detector.

Further intrinsic radioactivity arises mainly from the decay chains of ^{238}U and ^{232}Th, as well as ^{40}K. Special care also has to given to the presence of ^{222}Rn. It is a noble gas formed in the ^{238}U decay chain. In Hall C of the LNGS laboratory, radon activities around 80 Bq/m^3 are measured. It is hence utterly important to prevent any contact between the air and the scintillator. The same is true to prevent a contamination of the scintillator with ^{85}Kr, which has a Q value of 690 keV, a value close to the expected Compton edge from the ^{7}Be neutrinos. Its content in the scintillator can be probed through the rare decay sequence $^{85}\mathrm{Kr} \rightarrow {}^{85}\mathrm{Rb}^* + e^+ + \nu_e$ with the delayed coincidence of $^{85}\mathrm{Rb}^* \rightarrow {}^{85}\mathrm{Rb} + \gamma$. The activity of ^{85}Kr has thus been estimated to be 29 ± 14 counts per day and 100 tons.

4.3.2 Neutrons

Neutrons knocked out of the surrounding materials by cosmic muons are a serious threat to the Borexino measurements. Neutrons created by muons passing next to the detector are particularly critical, because their parent cannot be identified and vetoed. High energy neutrons may travel a distance of a few meters through different materials. Through elastic scattering, the neutron loses its energy to protons and thus leaves a signal in the detector. If it is thermalized within the scintillator, a delayed 2.2 MeV γ will be released from the neutron capture on Hydrogen. This signature can mimic the signal from the inverse β decay.

4.3.3 Cosmogenic Background

The Borexino experiment is well shielded from cosmic radiation by ∼ 3800 m.w.e. of rock. The cosmic muon flux in Hall C of the LNGS is reduced by almost 6 orders of magnitude to $\sim 1.2\,\mu/\mathrm{m}^2/\mathrm{h}$ compared to the flux on the Earth's surface ($\sim 6.5 \times 10^5\,\mu/\mathrm{m}^2/\mathrm{h}$). However, this still corresponds to approximately 4300 muons crossing the detector each day. The mean energy of these muons is about 320 GeV,

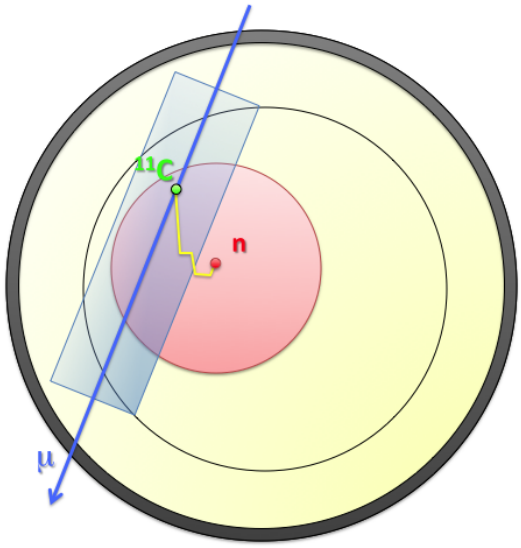

Figure 4.4: Principle of the three fold coincidence for the detection of cosmogenic background (Figure from [70]). If both the muon track and the position of the neutron capture are reconstructed, events within the intersection of a cylinder around the muon track and a sphere around the neutron can be vetoed for a few half-lives of the cosmogenic induced radioisotope.

since the low-energetic part of the cosmic muon spectrum is absorbed on its way through the rock.

Muons crossing the IV of the Borexino detector typically deposit hundreds of MeV of ionization energy in the detector and are thus easily discriminated from the solar neutrino signals. Special care has to be given to muons crossing only the buffer in the ID without passing through the IV. The light produced through both the Čerenkov effect in the buffer and from the remaining scintillation gives a significant signal despite the quenching effect of the DMP. Unfortunately, these signals can mimic the desired neutrino events. It is therefore necessary to effectively tag and veto these muons.

An even larger challenge are muon-induced cosmogenic events caused by spallation. The most prominent process is the knock-out of a neutron from the ^{12}C being one of the main constituents of the scintillator. The remaining ^{11}C decays via a β^+ with a half-life of 20.39 minutes and a Q value of 1982.2 keV. The emitted positron then almost instantly annihilates thus depositing a visible energy between ≈ 1 and 2 MeV in the detector which cannot be correlated to the incident muon anymore. Unfortunately, this signal overlays the energy range of CNO neutrinos and therefore hinders their detection. The expected rate for Borexino is 25 counts per day and dominates the CNO signal by approximately a factor of five [71].

To suppress the cosmogenic background, the so-called three fold coincidence is used [72]. The neutron knocked out by the muons will be captured by a hydrogen atom after a typical time of $\sim 250\,\mu$s, which will then de-exite and release a 2.2 MeV photon. This can be correlated to the crossing muon. Also, the position of the neutron capture can be reconstructed. Since its mean free path is rather short

(typically below 50 cm), the location of the cosmogenic induced carbon nuclei can be found in the intersection of a sphere around the location of the neutron capture and a cylinder around the muon track. Any signal occurring within this region during a few half-lives of the ^{11}C can now be vetoed thus reducing the cosmogenic background. However, it is desirable to keep the excluded region of fiducial volume small, in order to not reduce the overall statistics too much. Therefore, a good muon tracking is needed. Fig. 4.4 shows the schematic principle of the three fold coincidence. For a detailed description see [72].

4.3.4 Muon Identification and Tracking

Muons crossing Borexino are identified using several techniques. Light from the outer detector Čerenkov veto is a strong indicator for muons. Also the inner detector can be used by performing a pulse shape and timing analysis of the PMT signals: muon pulses feature longer rise and decay times than neutrino events of comparable energy. Thus, the outer and inner detector provide two independent and yet redundant tags for cosmic muons.

For the reconstruction of muon tracks, two different algorithms are used. One is based on the data from the outer detector and the other uses the information from the inner detector. A combination of the OD and ID fits is then further used for a third, global tracking. A brief overview of the tracking algorithms is presented here.

The characteristic light patterns created by muons crossing Borexino are used to reconstruct the muon tracks. For the OD tracking, the disk-like shapes from the Čerenkov cone of a crossing muon are identified by the PMTs close to the muon's entry point to the detector and after a time delay also close to the exit point. PMTs close to the entry point show significantly more photons registered than those further away. Also, the Čerenkov light reaches these PMTs earlier. Depending on the inclination of the track, the time profile of the hits corresponds to a circle or an ellipse around the entry point. Once the two clusters of PMTs indicating a crossing muon have been identified, the entry and exit points are determined by the charge barycenters of these clusters. A detailed description of the tracking algorithm is presented in [71].

The inner detector tracking relies mainly on the distinct patterns of the photon arrival times at the PMTs. Due to the high light output from crossing muons, the charge distribution of the PMTs cannot be used for the track reconstruction. A muon crossing the inner detector produces both scintillation and Čerenkov light. The Čerenkov light is emitted as the typical forward bound Čerenkov cone whereas the scintillation light evolves in all directions. First, the entry point is identified by the backward running scintillation light. For a first approximation, the time pattern of the hits registered within the first 5 ns of the event is analyzed. The exit point is then identified by determining the symmetry plane dividing the photon arrival pattern of the PMTs in half. This plane has to go through both the entry and exit point of the tracks, as well as through the center of the SSS, of which two are already known. Having found this plane already allows a rough determination of the azimuth angle of the muon track. To get an even better result, twelve planes perpendicular to the symmetry plane in rising distance from the entry point are investigated. The arrival times at the PMTs in each plane show a minimum around the track's azimuth angle φ when plotted against the azimuth location of the PMT.

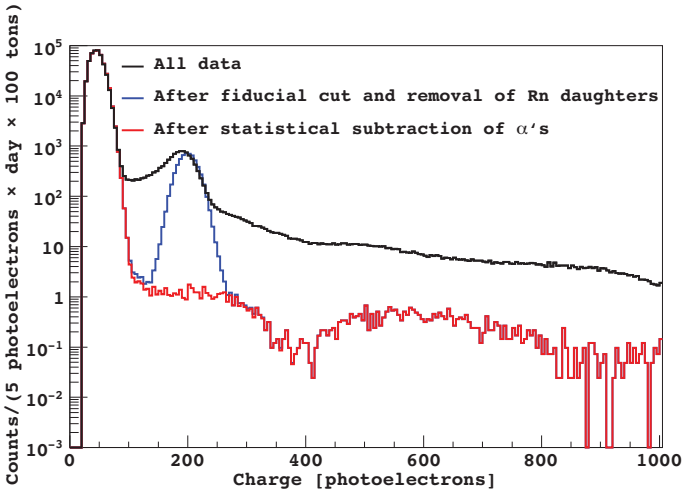

Figure 4.5: Raw photo electron spectrum after 192 days of data taking. The black line shows all data, whereas the blue and red lines show the data after the application of some basic cuts. The Compton like edge from the ^{7}Be neutrinos can be clearly seen around 300 photo electrons. Furthermore the impact of cosmogenic ^{11}C leaves a clear impact in the region between 400 and 800 photo electrons. The peak around 200 photo elecrons is caused by the decay of polonium. Figure from [69]

A fit is done for all twelve planes and the mean value of the obtained minimums is used as φ. For the exit point identification, the arrival times at the PMTs in the symmetry plane in dependence of their polar coordinate are investigated. They show a clear minimum at the entry point and another local minimum at the exit point. Having found both entry and exit point, the polar angle θ can easily be determined. A detailed description of the inner tracking can again be found in [71]. The angular resolution of the muon tracking is estimated to be in the order of a few degrees and the spacial resolution is better than 50 cm. However, to obtain a more profound estimate of the tracking's resolution, one has to know the exact muon coordinates to be able to compare them with the reconstructed values. The compact muon tracker introduced in Chapter 3 is capable of performing this task. It can thus be used to probe the quality of the Borexino muon tracking as will be presented in Chapter 5.

4.4 Borexino Results

The Borexino experiment has been taking data since May 16$^{\text{th}}$ 2007. The successful detection of solar ^{7}Be neutrinos was reported already a little over a year after that. Since then, also solar ^{8}B and geo-neutrinos have been observed. This section briefly summarizes the first Borexino results.

4.4.1 ^{7}Be Neutrinos

The successful detection of the 0.862 MeV ^{7}Be solar neutrinos in Borexino has first been reported in August 2008 [67]. The results are based on 192 online days of data taking. The interaction rate was found to be $49 \pm 3_{\text{stat}} \pm 4_{\text{syst}}$ counts per day and

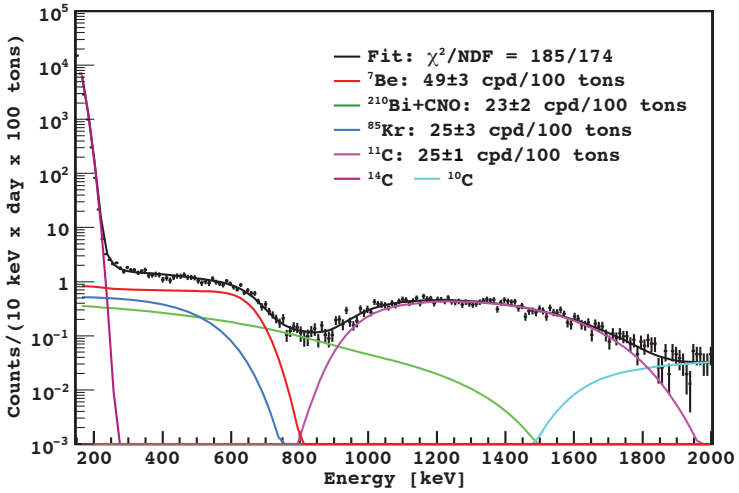

Figure 4.6: Fitted Borexino Data taken from [69]. The black data points already include all relevant cuts. The Figure does not include contributions from ^{214}PB, *pp*, and *pep* neutrinos which are almost negligible. Again, the Compton like edge for the ^{7}Be neutrinos can be clearly seen (red line). The fit result gives a rate of 49 ± 3 counts per day. For the ^{11}C background, a rate of 25 ± 1 is found.

100 tons.

For the analysis, events were chosen by a selection of cuts. A fiducial volume of 78.5 tons was chosen to reject external gamma background. Furthermore, events within 2 ms after a crossing muon were rejected to suppress events from the decay of short living cosmogenic induced radionuclides. Decays due to radon daughters could be removed by vetoing ^{214}Bi–^{214}Po coincidences. Events from the α decay of ^{210}Po could be identified through pulse shape discrimination and were subtracted from the spectrum. The raw photo electron spectrum after these basic cuts is shown in Fig. 4.5. The Compton-like edge from the reaction of ^{7}Be neutrinos is clearly visible around 300 photo-electrons. Below 100 photo electrons, the spectrum is dominated by the decay of ^{14}C. Furthermore, the impact of the β^{+} decay of ^{11}C can be seen in the region between 400 and 800 photo electrons (cf. Section. 4.3.3).

Fig. 4.6 shows the spectral fit of the data. For the ^{7}Be neutrinos, a rate of 49 ± 3 events per day and 100 tons is found. The high metallicity SSM predicts a rate of 74 ± 4 counts per day and 100 tons for no oscillations whereas the MSW-LMA scenario (assuming $\Delta m^2_{12} = 7.6^{-5}\,\mathrm{eV}^2$ and $\sin 2\theta_{12} = 0.87$) reduces this expectation to 48 ± 4 counts per day per 100 tons. Hence, the results confirm the matter enhanced oscillation hypothesis.

To test solar models, the measured neutrino flux is compared to the prediction of the SSM. The measurements also give new constrains to the ratio f_{Be} between the ^{7}Be neutrinos flux predicted by the high metallicity SSM and the measured value, where f is defined as the true solar neutrino flux divided by the corresponding value of the fluxes predicted by the according solar model. For the MSW-LMA oscillation scenario, a value of $f_{\mathrm{Be}} = 1.02 \pm 0.10$ is obtained. The analysis ales gives a constraint for the ratio f_{CNO} for CNO neutrinos of $f_{\mathrm{CNO}} < 3.80$ and a value f_{pp} for *pp* neutrinos of $f_{pp} = 1.005^{+0.008}_{-0.020}$. The constraint on f_{CNO} translates into a CNO contribution of

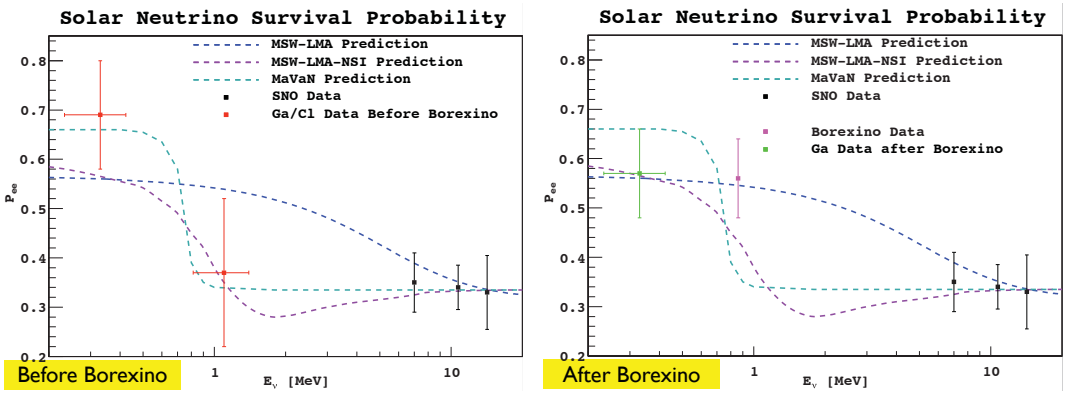

Figure 4.7: Energy dependent survival probability of solar neutrinos for different matter effect mechanisms compared with solar oscillation data before and after the Borexino ^{7}Be measurements. Figures taken form [44]. The Borexino data strongly supports the LMA solution of the MSW effect.

less than 3.3% to the solar luminosity.

Matter Enhanced Oscillations

The survival probability of mono-energetic solar ^{7}Be neutrinos can be used to test the different models of matter enhanced oscillations. Fig. 4.7 shows the predictions of the MSW-LMA, MSW-LMA-NSI, and MaVaN models presented in Section 2.3.3 for oscillations of solar neutrinos. Solar neutrino oscillation experiments before Borexino could not distinguish between the different models. Results from the ^{7}Be neutrino measurements, however now strongly support the LMA solution of the MSW effect.

Day-Night Asymmetry

The ^{7}Be neutrino spectrum has been also investigated for a possible day-night asymmetry. Depending on the model, mass effects in Earth could lead to a regeneration of solar neutrinos oscillated into ν_μ or ν_τ back into ν_e. The neutrino rate would then depend also on the latitude of the detector as well as the time of the day. At night, the Sun would appear brighter in the neutrino light. A preliminary analysis is presented in [73]. Measurements from 422.12 days are presented in Fig. 4.8. The data splits up into 212.87 days and 209.25 nights. The day night asymmetry A_{dn} is defined as

$$A_{dn} = \frac{c_n - c_d}{c_n + c_d},$$

where c_n and c_d are the number of counts during night and day respectively. An average value of $A_{dn} = 0.011 \pm 0.014$ is found, showing no significant day night asymmetry and thus confirming the expectation of the LMA-MSW scenario and excluding the alternate oscillation scenario based on the mass varying model (cf. Section 2.3.3)

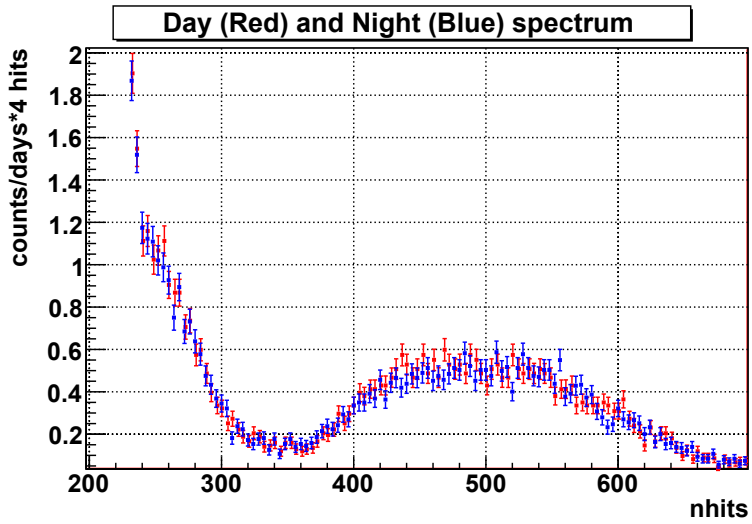

Figure 4.8: Day and night spectra for the energy region outside the ^{210}Po peak. No significant difference between the spectra is observed. Figure from [73].

4.4.2 ^{8}B Neutrinos

Spectroscopic measurements of solar ^{8}B neutrinos have been done previously by Kamiokande [11] and Super-Kamiokande [31] using a water Čerenkov detector and SNO [74] using deuterium as a target, all with an energy threshold of ~ 5 MeV or higher. Recently, the SNO collaboration published an analysis with a threshold of 3.5 MeV [29].

Borexino is the first experiment succeeding in spectroscopic measurements of the ^{8}B neutrino flux using liquid scintillator. All major backgrounds above the 2.614 MeV gamma from the decay of ^{208}Tl could be reduced sufficiently allowing to set the energy threshold for the ^{8}B neutrinos as low as 3 MeV [75]. Taking into account the ^{7}Be neutrino measurements described in the previous section, Borexino is the first experiment where neutrinos from both pp-chain reactions have been investigated simultaneously. Very interestingly, the energy region of those neutrinos covers the transition region from vacuum to matter dominated oscillations in the LMA solution of the MSW effect described in Section 2.2.2, thus providing an excellent method to experimentally challenge this prediction.

Two different analyses were done for the ^{8}B neutrinos, one with a threshold of 3 MeV and another one with a higher threshold at 5 MeV to be able to compare the results with earlier measurements from Super-Kamiokande and SNO. Recent results are based on 488 days of data taking, with a total exposure time after cuts of 345.3 days in a fiducial target volume of 100 tons.

^{8}B neutrinos were selected from data through the application of a set of cuts described in [75]. An interaction rate of $0.217 \pm 0.038_{\mathrm{stat}} \pm 0.008_{\mathrm{syst}}$ counts per day and 100 tons was found for an energy threshold of 3 MeV. Raising this threshold to 5 MeV, $0.134 \pm 0.022_{\mathrm{stat}}\,^{+0.008}_{-0.007\,\mathrm{syst}}$ counts per day and 100 tons remain. Fig. 4.9 shows the ^{8}B neutrino energy spectrum for the selected data. It is consistent with the high metallicity SSM BPS09(GS98) model presented in Section 2.3 in combination

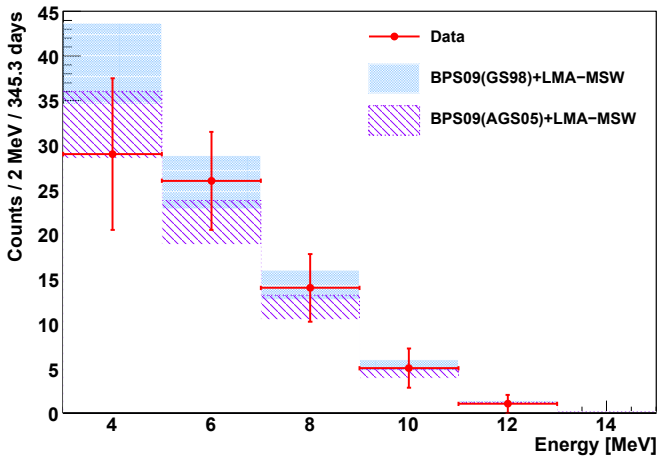

Figure 4.9: ^{8}B neutrino spectrum measured by Borexino. The red dots show the spectrum after data selection and background subtraction. Also shown are the expected values from current SSMs with high (BPS09(GS98)) and low (BPS09(AGS05)) metallicity under the assumption of LMA-MSW oscillations. Figure from [75].

with the prediction of LMA-MSW oscillations assuming $\Delta m^2 = 7.69 \times 10^{-5}\text{eV}^2$ and $\tan^2\theta = 0.45$ also included in the plot.

The ^{8}B neutrino flux derived from the data is found to be $(2.7\pm0.4_{\text{stat}}\pm0.2_{\text{syst}})\times 10^6\,\text{cm}^{-2}\text{s}^{-1}$ above 5 MeV and $(2.4\pm0.4_{\text{stat}}\pm0.1_{\text{syst}})\times10^6\,\text{cm}^{-2}\text{s}^{-1}$ above 3 MeV. This compares to an expected flux predicted by the SSM of $(5.88 \pm 0.65) \times 10^6\,\text{cm}^{-2}\text{s}^{-1}$ with no oscillation, thus confirming solar ν_e disappearance. The average ν_e survival probability $\bar{P}_{ee}$ has been calculated for both energy regions. For a mean energy of 8.9 MeV a value of $P_{ee} = 0.29 \pm 0.10$ for ^{8}B neutrinos is obtained. Comparing this result with the survival probability of the mono energetic 0.862 MeV ^{7}Be neutrinos presented in the previous section allows again to test the matter enhanced oscillation mechanisms of solar neutrinos. Both probabilities are shown in Fig. 4.10 among the earlier results from SNO and the radio chemical experiments. The data confirm the MSW-LMA solution for matter enhanced oscillations of solar neutrinos. However, whereas the MSW-LMA model seems to be favored also in combination with the other solar oscillation experiments, recent analyses including also the KamLAND data see hints for possible non standard interactions [76].

4.4.3 Anti Electron Neutrinos – Geo-Neutrinos

The observation of geo-neutrinos has been first reported by KamLAND in 2005 [49]. Although Borexino is smaller than the KamLAND detector it has the advantage of a significantly lower anti neutrino background from nuclear power plants. Also, the intrinsic radioactive background is much lower and thus a successful observation of geo-neutrinos was reported in 2010 [50].

The results are based on a 252.6 ton year fiducial exposure. Altogether 21 $\bar{\nu}_e$ candidate events could be identified. Anti electron neutrinos have two main sources on Earth: they are produced at nuclear reactors and they are emitted in β^- decays.

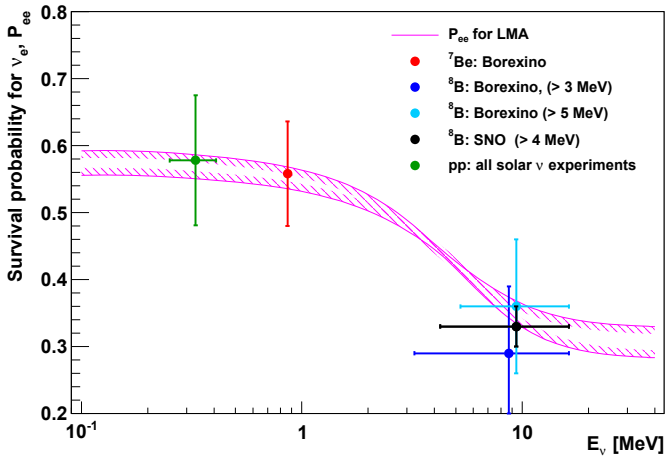

Figure 4.10: Survival probability P_{ee} for different neutrino energies as measured by several solar neutrino experiments. The pink line shows the expected survival probability from the MSW-LMA predictions. The data points cover, very interestingly, the transition area between matter dominated and vacuum dominated neutrino oscillations. Figure from [75].

Very conveniently, there are no near-by nuclear reactors to the LNGS underground laboratory. The mean baseline to distant nuclear reactors is approximately 1000 km. Nevertheless, the contribution of reactor neutrinos is not negligible. The main contribution comes from 194 reactors in Europe, whereas the remaining 245 reactors around the world contribute only 2.5% of the nuclear $\bar{\nu}_e$ flux at Gran Sasso. The expected neutrino signal from nearby reactors has been carefully investigated by a detailed analysis of their power time profiles and nuclear fuel composition.

No significant flux of geo-neutrinos with an energy above 3.272 MeV is expected (cf. Section 2.4.4). This corresponds to a visible energy of approximately 2.6 MeV or 1300 p.e. in Borexino. Reactor neutrinos, however, can easily reach energies up to 8 MeV. In the geo-neutrino window, 5.0±0.3 events from reactors are expected. Since the neutrinos in the energy regime leading to a light yield above 1300 p.e. originate solely from nuclear reactors, this region can be used to confirm the assumptions made for the reactor neutrino flux. The collected data is presented in Fig. 4.11. A fit has been done for the contributions of geo-neutrinos, reactor neutrinos and background to the spectrum. The best estimates are $N_{\text{geo}} = 9.9^{+4.1}_{-3.4}$ and $N_{\text{react}} = 10.7^{+4.3}_{-3.4}$ at 68.3 %C.L., the hypothesis of no geo-neutrinos being observed is rejected at 99.997% C.L. The measurement also rejects the hypothesis of an active geo-reactor in the Earth's core with a power above 3 TW at 95 %C.L.

4.5 *pep* and CNO Neutrinos

The results from the Borexino ^{7}Be and ^{8}B neutrino measurements combined with other solar neutrino experiments show that the LMA-MSW oscillation predictions are in good agreement with the observations. However, the energy region between

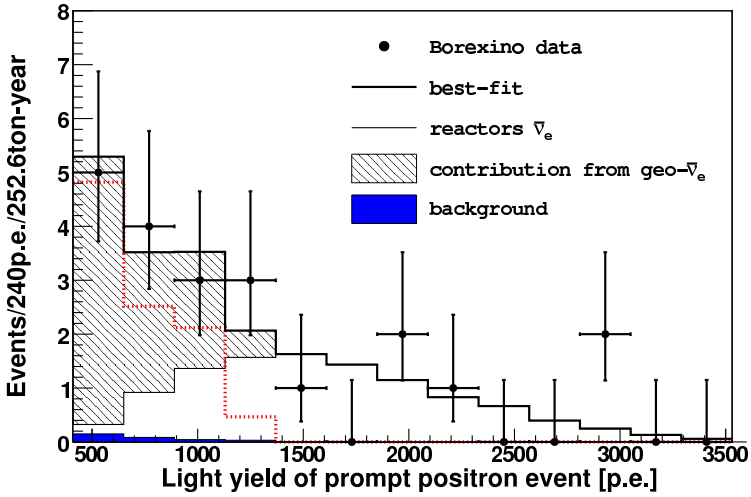

Figure 4.11: Light yield spectrum for the positron prompt events of the $\bar{\nu}_e$ candidates observed in Borexino. Figure taken from [50]. The dotted red line shows the fit for the geo-neutrino contribution.

the ^{7}Be neutrinos of 0.862 MeV and the lower threshold of the ^{8}B measurements of 3 MeV has not yet been thoroughly investigated. This is exactly the region at which the transition between vacuum and matter dominated oscillations occurs. *pep* neutrinos are mono-energetic with an energy of 1.442 MeV. CNO neutrinos can reach energies up to 1.732 MeV. The observation of *pep* and CNO neutrinos could thus be used to probe this region.

The CNO neutrino flux is still one of the major uncertainties in the standard solar models. Measuring it would allow to improve the predictions for the Sun's metallicity Z. Like the ^{7}Be neutrinos, *pep* neutrinos could be easily identified by a Compton-like edge in the energy spectrum. Their flux is directly correlated to the *pp* neutrino flux. Measuring the *pep* neutrino flux would thus allow to draw conclusions on the fundamental *pp* fusion reaction. Besides the impact on soalr physics, measuring the CNO neutrino flux also allows for testing the intemediate energy regime of the transition region of the MSW effect.

The combined flux of *pep* and CNO neutrinos is predicted to be of the order of $7 \times 10^8\,\mathrm{cm}^{-2}\mathrm{s}^{-1}$, almost one order of magnitude below the lower energetic ^{7}Be neutrino flux but more than one order of magnitude above the higher energetic ^{8}B neutrino flux. Neutrinos from these two sources have already successfully been detected, hence it should also be possible to observe *pep* and CNO neutrinos. Unfortunately, the energy region of interest is dominated by the uncorrelated ^{11}C cosmogenic background, caused by cosmic muons passing the detector. The expected rate of ^{11}C events in Borexino is expected to be approximately five times higher than the neutrino signal. It is thus utterly important to find a way to sufficiently suppress this background. It has been shown in Section 4.3.3 that the three fold coincidence is used for this task. It relies on a precise muon tracking to avoid excluding large volumes from the fiducial value. The CMT can perform this kind of measurement, however, the detector is not capable to cover all of Borexino. Nevertheless it can be used to improve the ^{11}C tagging. By comparing results of tracks reconstructed by

the CMT to the Borexino tracking, the quality and uncertainties of the latter can be determined. This allows to identify systematic errors in the Borexino tracking. Also, understanding well the errors of the reconstructed muon tracks allows to keep the volume identified by the three fold coincidence small. To perform this task, the CMT has been installed on top of the Borexino detector. The setup and first results will be presented in the next chapter.

Chapter 5

CMT for Borexino

As described in Chapter 4.3, uncorrelated cosmogenic induced background dominates the energy range between 1 and 2 MeV in Borexino. This is exactly the energy range of CNO and *pep* neutrinos. In order to detect these neutrinos it is thus necessary to understand well the effects of muons crossing the detector and to find an effective method to suppress the background.

Identifying cosmogenic background events is not trivial since the actual background signal is not correlated to the crossing muon. Thus a simple muon veto is insufficient. Instead, a three-fold coincidence of a crossing muon, a neutron capture and the delayed radioactive decay is used to reduce the cosmogenic background. The produced cosmogenic radionuclide is expected to be within the intersection of a cylinder around the initiating muon track and a sphere around the captured neutron. The affected volume can then be taken from the fiducial volume for a time period of a few half-lives [72]. However, with more than 4000 muons crossing the detector each day resulting in approximately 25 ^{11}C decays, this could quickly lead to a large part of the fiducial volume blinded. Therefore the coordinates of the muon track need to be known with a high precision to apply this cut. In Borexino, tracks are reconstructed from the time and pulse shape information from the PMTs when a muon crosses the detector (cf. Section 4.3.4). This method allows to reconstruct tracks with a resolution of approximately 50 cm.

An exact determination of the resolution of the Borexino muon tracking is hence a key prerequisite for keeping the vetoed volume small. The angular resolution has been estimated before by a comparison of the angular muon distribution to the data collected at LNGS by the MACRO detector [70]. However, for an exact determination of the resolution on an event by event basis, the true coordinates of the passing muon have to be known. The CMT presented in Chapter 3 is capable of reconstruction muon tracks with a precision close to their true coordinates. Operating the CMT together next to the Borexino experiment allows to collect a sample of cosmic muons that pass both detectors. This sample can thus be used as a reference for determining the resolution of the Borexino tracking.

This chapter describes the setup of the CMT at the LNGS laboratory. It is now used to sample those cosmic muons crossing both the CMT and Borexino. Thus, some muon tracks will be known with high precision and can then be compared to the Borexino reconstruction allowing to test the quality and the efficiency of the Borexino track reconstruction. Possible systematic errors can be identified and thus

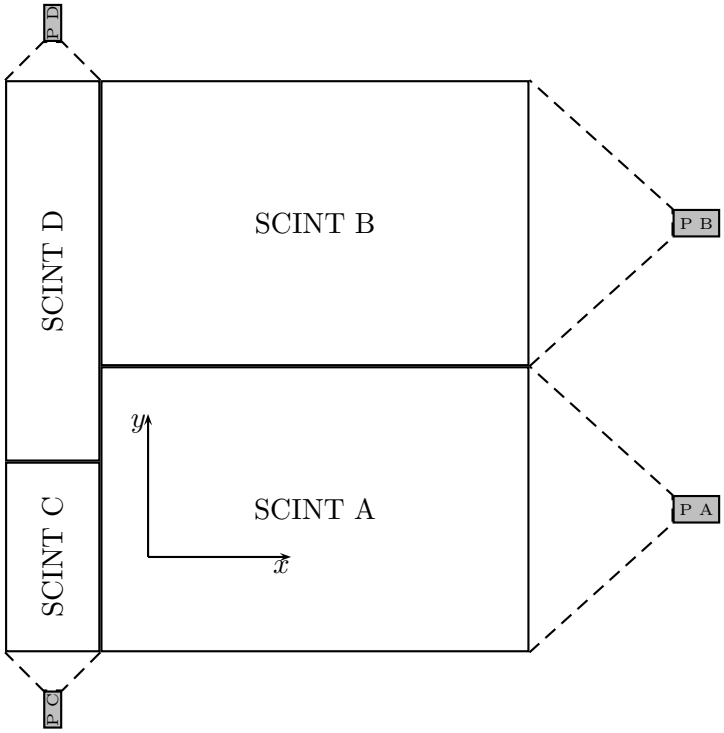

Figure 5.1: Scintillator Setup for the trigger. The detector is triggered by a coincidence signal of two layers of plastic scintillator above the detector. Both layers have the same layout depicted in the figure. They a combined of four single scintillators A,B,C and D with a light concentrator and PMT (PA, PB, PC and PD respectively) attached to each.

the whole reconstruction be improved.

The first part of this chapter describes the modified setup of the CMT for Borexino. It is followed by a brief Monte Carlo study of cosmic events passing both the CMT and Borexino. Furthermore a look at the performance during and after commissioning and some early results of data taking are presented. Finally, a similar analysis using muons produced by the CNGS beam that were reconstructed by the neighboring OPERA detector is done.

5.1 CMT at the Borexino Experiment

For its use at Borexino, the CMT layout has been slightly modified. Instead of four arrays of one drift tube module each, two modules are placed next to each other leaving only one array per stereo angle. This results in a larger effective area, almost by a factor of four, and thus more muon tracks can be sampled. Also the angular acceptance is improved significantly as will be shown in Section 5.1.1. Yet another advantage of this design is the even more compactness of the detector. This setup leaves only four layers of drift tubes in each 2D plane which results in a slight reduction of resolution and efficiency. This effect has been studied and is presented in Section 5.1.2.

The muon tracker has been reassembled in Hamburg in October 2009. All electronics were fitted in one rack. The trigger scintillators previously used do not cover the complete surface area of the new setup, therefore different plastic scintillators are placed next to each other. Altogether, two layers of scintillator with an effective area of $1.1 \times 1.2\,\mathrm{m}^2$ each are placed on top of the detector. Each layer consists of an identical setup of four single scintillators:

- Two $90 \times 60\,\mathrm{cm}^2$ scintillators (A,B) equipped with Valvo XP 2008 UB PMTs operated at $-1850\,\mathrm{V}$.
- One $20 \times 40\,\mathrm{cm}^2$ BC 400 scintillator (C) with attached PMT by BICRON operated at $+900\,\mathrm{V}$.
- One $20 \times 80\,\mathrm{cm}^2$ BC 400 scintillator (D) with attached PMT by BICRON operated at $+900\,\mathrm{V}$.

The lower trigger scintillator is placed at $z = 227\,\mathrm{mm}$ in the CMT reference system, the second layer is placed directly on top of it. The layout of a trigger plane is presented in Fig. 5.1.

The tracker was assembled in Hamburg and then shipped to Gran Sasso in one piece. The same was done for the electronics rack. Before shipment to Italy, all components were tested and calibrated in the laboratory in Hamburg. This had to be done because once the detector was installed at the LNGS, the muon rate would not be sufficient for calibration and other tests. The following tests were done:

- Drift time calibration for Hamburg conditions
- Setup of PMTs (thresholds and HV)
- Wire alignment data taking

The tracker was installed on top of Borexino in November 2009. It is located on the top platform of the detector, approximately 13.6 m from the center of the Borexino sphere. The modified setup is shown in Fig. 5.2. The tracker is operated in its own reference system, a schematic drawing of the CMT in its reference system is shown in Fig. 5.3. The reference system for each 2D plane is similar to that from the original setup. The x and y origin is located in the sixth tube of the lowest tube layer of the first module in the according plane. The $z = 0$ plane is defined by the lowest tube layer of the modules in the $x - z$ plane. A schematic can be seen in Fig. 5.4.

The position of the detector was determined with respect to the Borexino center with a precision of 1 cm. Fig. 5.5 shows a top view of the Borexino water tank and the CMT. The relative coordinates of the Borexino center in the CMT reference frame are presented in Tab. 5.1. The detector is rotated by an angle $\beta = 58.19°$ with respect to the Borexino system.

The trigger signal distributed by the trigger board is also converted to a NIM signal and sent via a 30 m long BNC cable to the Borexino DAQ. In case of a trigger signal coinciding with a Borexino event, a flag is set in the Borexino data, allowing an easy and correct matching of events.

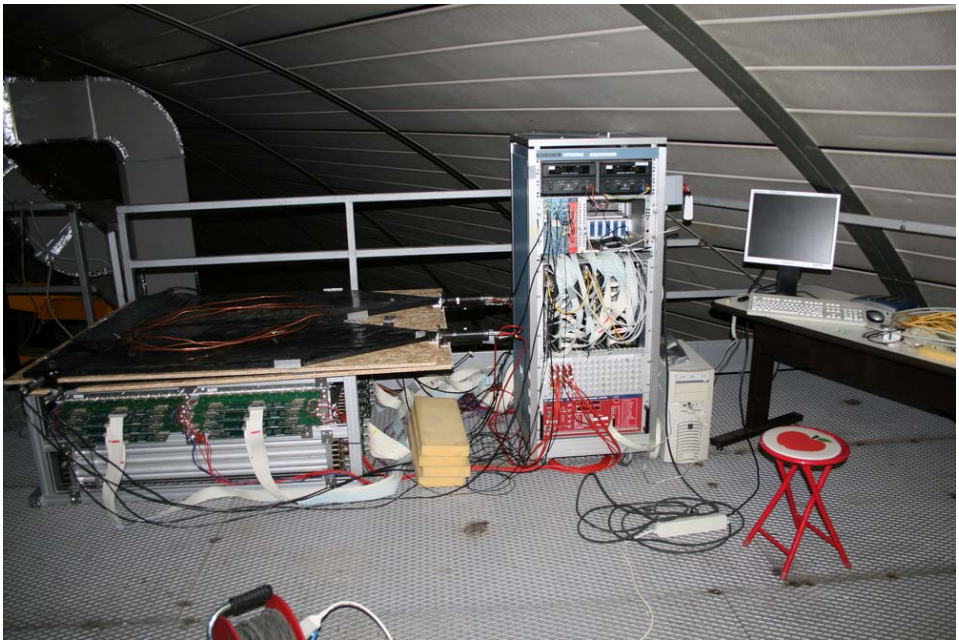

Figure 5.2: The CMT setup on top of Borexino at Gran Sasso

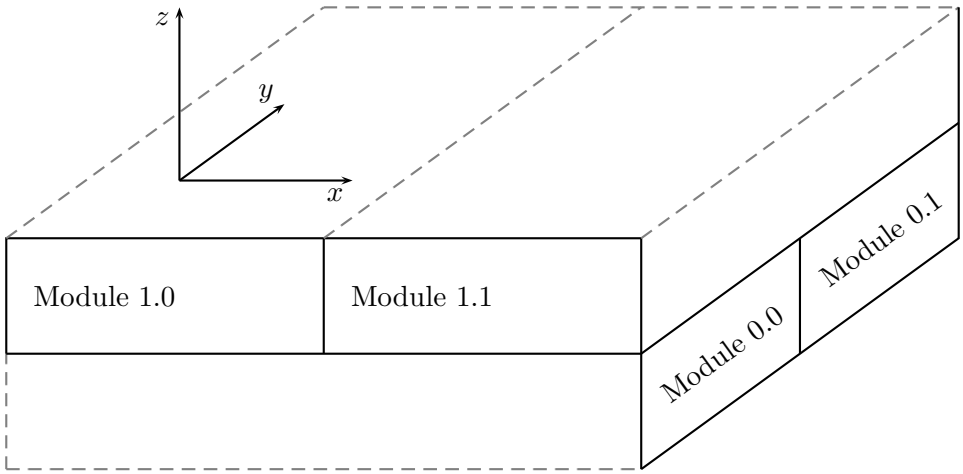

Figure 5.3: Reference system of the CMT. The first number of each module denotes the according TDC whereas the second number stands for the order in which it's connected to the TDC.

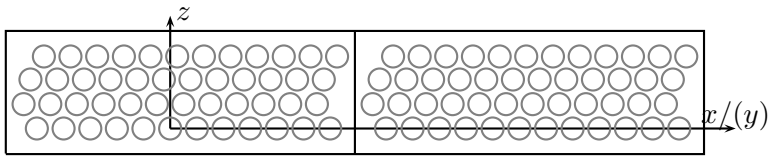

Figure 5.4: 2D front coordinate system for the CMT. For the $x-z$ plane the origin is located as drawn in the sixth tube of the lower layer. To maintain a consistent reference system, the origin is located 194 mm above this reference tube for the $y-z$ plane since the corresponding module are placed underneath the other ones.

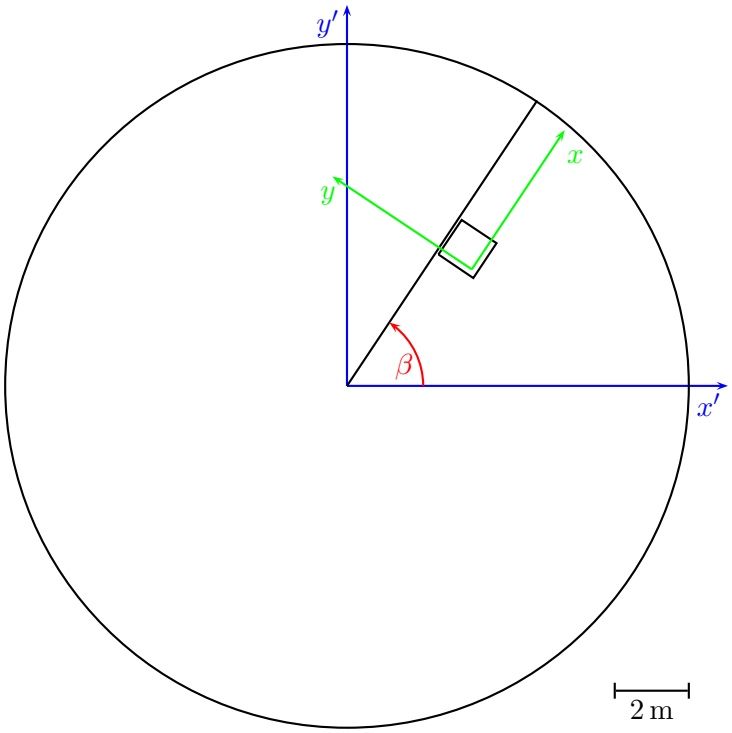

Figure 5.5: Top view: Position of the CMT (square) on top of the Borexino water tank (circle). The coordinate systems of both the CMT (green) and Borexino (blue) are shown. They are rotated at an angle β with respect to each other.

Table 5.1: Relative coordinates of the Borexino center within the CMT reference system.

Value	Shift
Δx	-4532.33 mm
Δy	887.456 mm
Δz	-9244.96 mm
β	58.19°

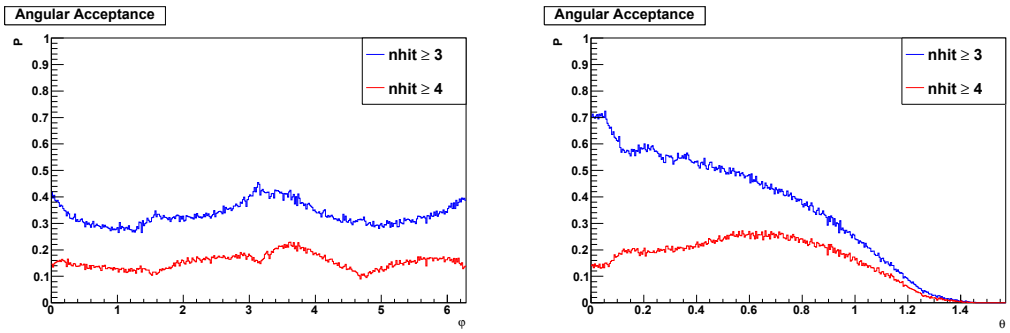

Figure 5.6: Angular acceptance of the CMT for the azimuth angle φ (left) and the polar angle θ (right). The number of events is normalized to events equally distributed in the trigger plane. The red line shows the relative number of events for the requirement of at least four hits per 2D array. The total number of events is significantly enhanced by lowering this to three hits only.

5.1.1 Angular Acceptance of the Modified Setup

To analyze the angular acceptance of the modified setup, a simple simulation has been used. Considering the new geometry of the detector, tracks were randomly generated in the trigger plane. No specific angular distribution was taken into account, both the azimuth and zenith angles of the tracks were generated homogeneously. For each track, the number of hit tubes in each 2D array was determined. Fig. 5.6 shows the probability that a triggered event leaves at least three (four) hits in each 2D array in dependence of the azimuth and polar angle. Fig. 5.7 shows the same results for a direct correlation of the polar and azimuth angle. The modified setup is sensitive to all azimuth angles, the sensitivity only varies a little in dependence of φ. The minimal required number of hits has no significant effect on the acceptance in φ. The total number of events improves significantly by a factor of almost two. However, looking at the polar angle distribution, this improvement mainly occurs for small values θ. The expected effect for real data will be smaller because these events are suppressed in realistic angular distributions due to the solid angle.

5.1.2 Reconstruction with Three Hits Only

To study the effects of a reconstruction with three hits only, a real event sample with four hits per event has been taken as a reference. Each event was modified so that only three hits remained, leaving four different combinations per event. All combinations were reconstructed and the resulting track parameters were compared to the original reconstruction with four hits. The results show that 99.7% of the tracks are also reconstructed with only three hits. However, depending on the quality of the calibration, not all tracks are reconstructed correctly. Fig. 5.8 shows the difference between the Hesse parameter α of both a reconstruction with four and three hits per plane. The distribution shows a clear peak around zero, which can be fitted by a Gaussian. The σ of the fit is found to be 24 mrad. This can be taken as a rough estimate of the angular resolution for the reconstruction with three hits only. This value is approximately five times larger than the resolution found for

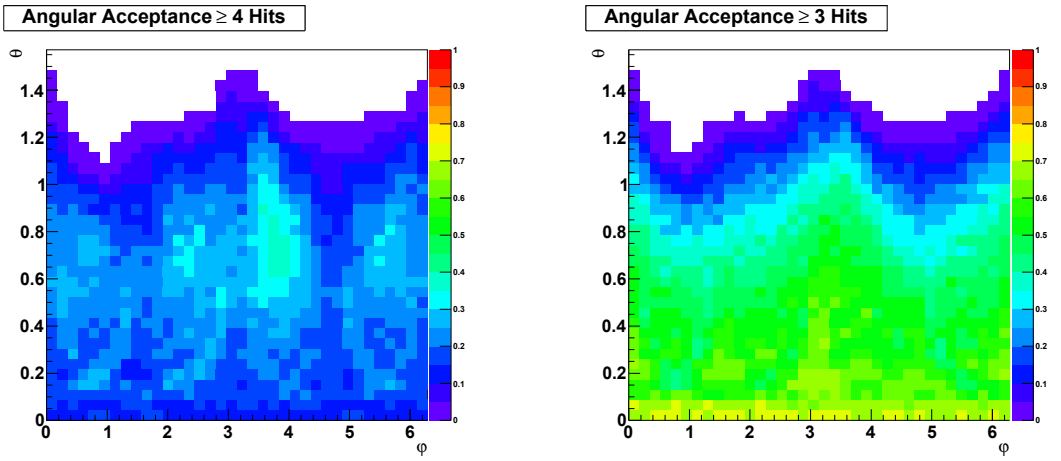

Figure 5.7: Angular acceptance of the CMT. The number of events is normalized to events equally distributed in the trigger plane. The left picture shows the relative number of events requiring at least four hits in each 2D array. In the right figure, this requirement is lowered to three hits.

the original setup. However, it still surpasses the Borexino tracking by far. The data used for the analysis originates from actual data taken at Gran Sasso to obtain realistic results. As will be shown in Section 5.2.1, the calibration for this data still needs some improvement. It is therefore assumed, that the resolution of a reconstruction with three hits only will also improve, once a better calibration can be performed.

5.1.3 Monte Carlo Simulation of Muon Tracks

To estimate the event rate in the CMT for the changed setup, events have been simulated taking into account the reduced muon flux and specific angular distribution inside the LNGS tunnel laboratory. The simulation method is similar to that presented in Section 3.8.1. The major difference is the distribution of θ and φ. This has been measured very precisely by the MARCRO collaboration [77] and the track angles were produced according to their results. Altogether, 1033426 events have been generated. For the simulation, the CMT is assumed to have an efficiency of 100%. For each event both the the number of tubes passed in each CMT plane and the impact parameter towards the Borexino center are calculated. If the impact parameter is below 8 m (the radius of the Borexino water tank), a flag for a common event is set. For the CMT events, it is useful to also apply a cut where at least three or four tubes per plane have to be hit. This resembles the minimal requirement for a track reconstruction.

After the production of Monte Carlo events, the event rates are simply determined by looking at the ratio of events exceeding a minimal number of hits compared to all generated events. Combined with the known muon flux of 1.16 μ/h the rates can be calculated. Results are presented in Tab. 5.2 for events with and without the requirement of the Borexino flag for different requirements for the number of hits in the CMT. Besides the discrimination between events that pass the Borexino or not,

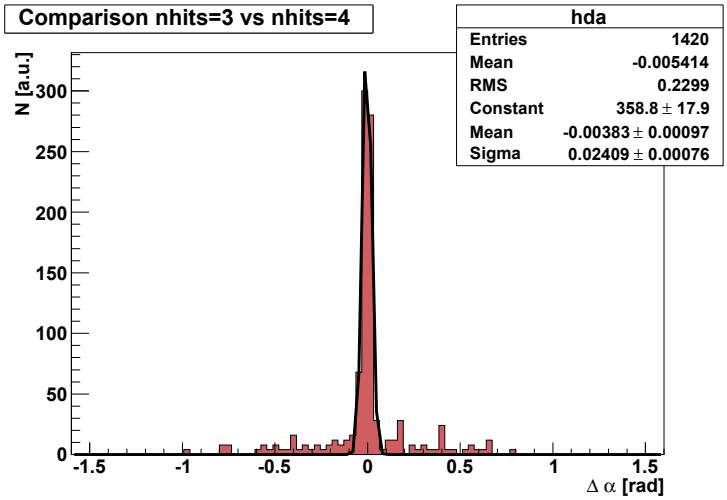

Figure 5.8: Comparison of the angular Hesse parameter α from a track reconstruction with four hits vs. a reconstruction of the same event using only three hits. The plot shows the difference $\Delta\alpha$. A distinct peak around zero is observed showing that a reconstruction only with three hits works.

it has also been investigated how many tracks are expected to cross the Borexino inner detector and inner vessel.

To test the functionality of the detector, the angular distribution of real reconstructed events was compared to those of the Monte Carlo for both events with and without the Borexino flag. Fig. 5.9 shows the comparison for all events analyzed so far by the CMT. Monte Carlo and real data are in good agreement confirming the functionality of the setup at Borexino. A comparable result is obtained using only data of common events with Borexino.

Table 5.2: Expected event rates for the CMT from the Monte Carlo simulation. The first row contains the results for all simulated muons whereas in the second row only muons passing Borexino and finally in the third and fourth row events crossing the inner detector (ID) and inner vessel (IV), respectively, are selected. n_{trigger} is the total number of expected muons per day, n_{events} requires at least a hit in each 2D plane. For the following columns stronger cuts on the minimal number of hits were applied (4 and 3 respectively).

	n_{trigger}/day	n_{events}/day	$n_{\text{events,4}}$/day	$n_{\text{events,3}}$/day
All MC events	27.84	15.6094	5.98253	12.0029
BX CMT flag	19.0998	12.375	4.53726	9.64201
BX ID	11.0443	7.68136	2.7781	6.06117
BX IV	4.33561	3.1374	1.13226	2.48724

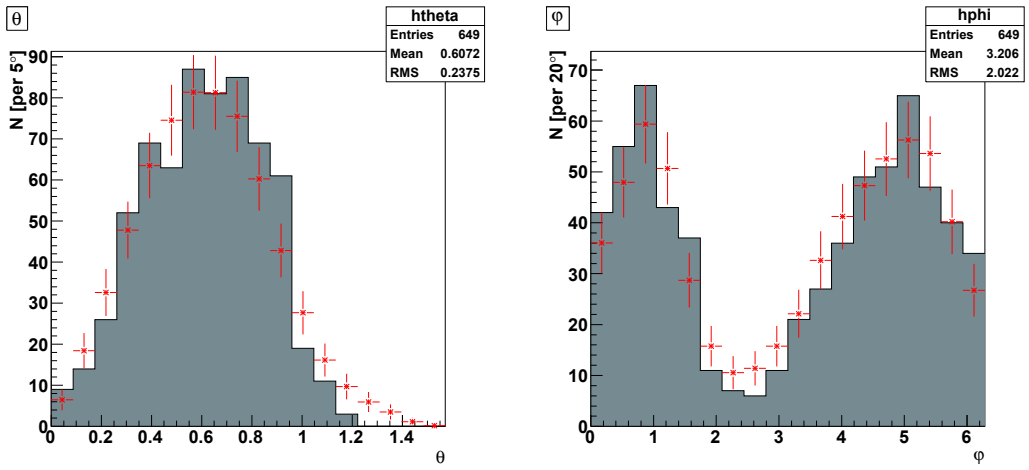

Figure 5.9: Zenith and azimuth angular distributions for events observed by the CMT. The filled area shows the actual data wheres the red crosses show the results from the Monte Carlo simulation.

5.2 Commissioning and Early Results

Although the detector was installed already in November 2009, the commissioning did not start until late January 2010 due to a missing gas supply. Because of the low flux of cosmic muons a check of the detector functionality takes a few days to gather enough statistics. The detector is running at all times, however due to occasional power cuts in the laboratory, there are some discontinuities in the data. After a power cut, data taking has to be resumed manually. In the first weeks of data taking, some of these restarts of the detector unfortunately remained unnoticed for a couple of days. Meanwhile, an automatic email alert system has been set up sending out warning messages whenever there is a restart of the system. However, it is foreseen to connect the CMT to a UPS[1] in the near future to both ensure continuous data taking and to prevent the system from any damage.

Data taking started on January 28$^{\text{th}}$ 2010. The results presented here rely on the data taken until the 6$^{\text{th}}$ of September 2010. An overview of the runs taken during this period is given in Tab. 5.3. A 2D projection of a typical event is depicted in Fig. 5.10 and Fig. 5.11 shows a different event in the 3D display.

5.2.1 A First Look at Events

Due to the small muon rate, the overall number of events is too little for self-calibration. Therefore, a calibration was done in Hamburg before setting up the detector underground. Of course, this calibration suffers from the different ambient conditions in the laboratories in Hamburg and Gran Sasso, the main differences being pressure and temperature. Three attempts of a calibration have been made: First, a reconstruction was done with the original CMT calibration from the test measurements before shipping the detector to Gran Sasso. Second, a calibration obtained by a similar detector setup in Hamburg which uses a gas system to control

[1] UPS: Uninterruptable Power Supply

Table 5.3: Overview of all muon runs taken until November 2010. The name of each run also indicates the starting date of the run. The first number is the day in the year, followed by the local time (in CET and CEST accordingly). The number of events is determined by a basic cut on the number of hits. For each 2D plane, a minimum number of four (three) hits has to be reached, it may not exceed twelve hits.

Run	Duration [s]	Delay [5 ns]	U_{th} [mV]	n_{trigger}	$n_{\text{events,4}}$	$n_{\text{events,3}}$
028_12-22-30	686846	100	50	32630	23	41
036_11-10-29	5675937	100	50	155660	272	392
102_11-08-06	628001	100	50	15911	31	46
118_15-04-24	173764	100	50	3913	9	13
120_21-15-25	3358291	200	100	70620	182	263
173_12-31-34	166847	200	100	2726	3	4
175_12-24-38	948399	200	100	15615	28	51
187_14-05-39	1072826	200	100	12932	36	53
200_04-54-28	191376	200	100	2399	9	14
203_18-49-43	838198	200	100	8881	29	39
214_01-03-07	2542185	200	100	32474	49	98
243_11-23-20	517972	200	100	11215	102	111
253_14-44-50	278867	200	100	6505	15	22
Sum	17079509			371481	788	1647

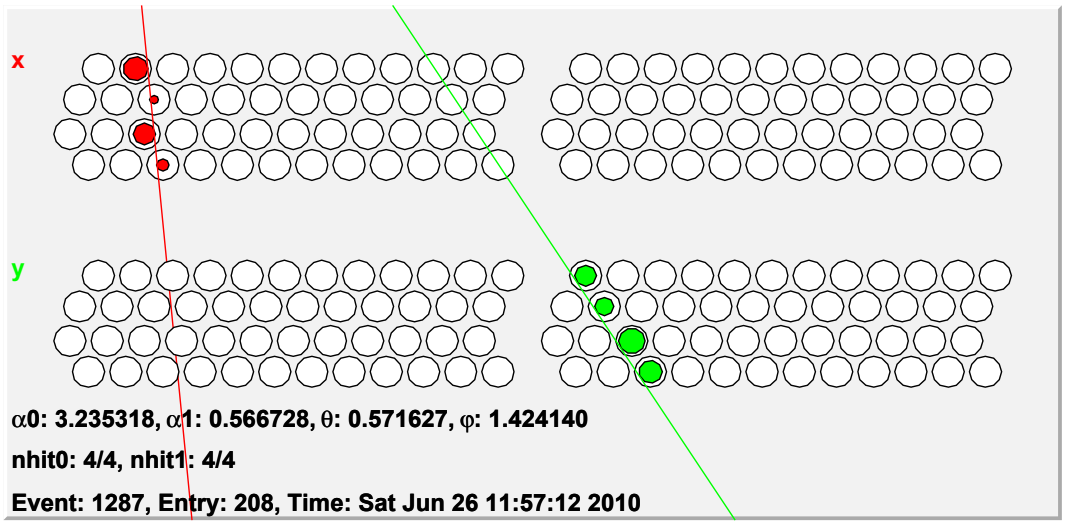

Figure 5.10: Event display of a muon tracked by the CMT on top of Borexino. The cross sections of both 2D planes are projected into a single plane. Red circles indicate the hits in the $x-z$-plane and green circles stand for the $y-z$-plane.

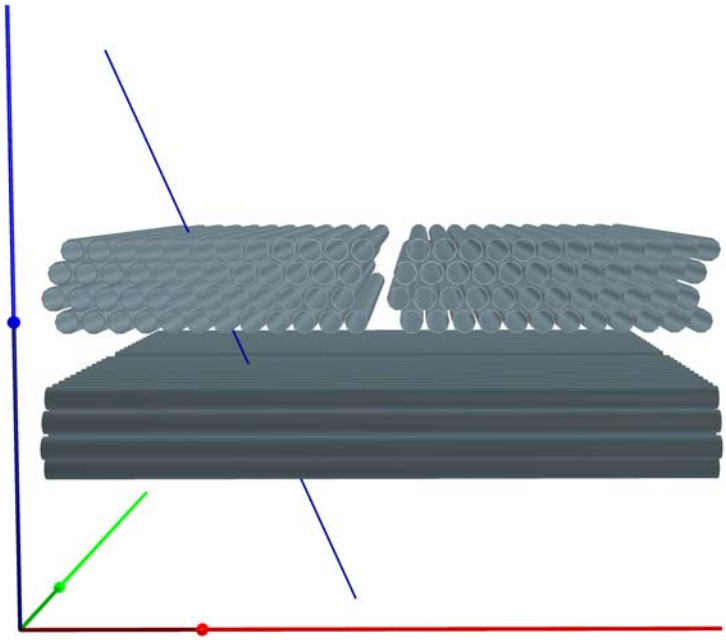

Figure 5.11: 3D event display of a muon tracked by the CMT on top of Borexino. The coordinate system (x: red, y: green, z: blue) is shifted from its actual position.

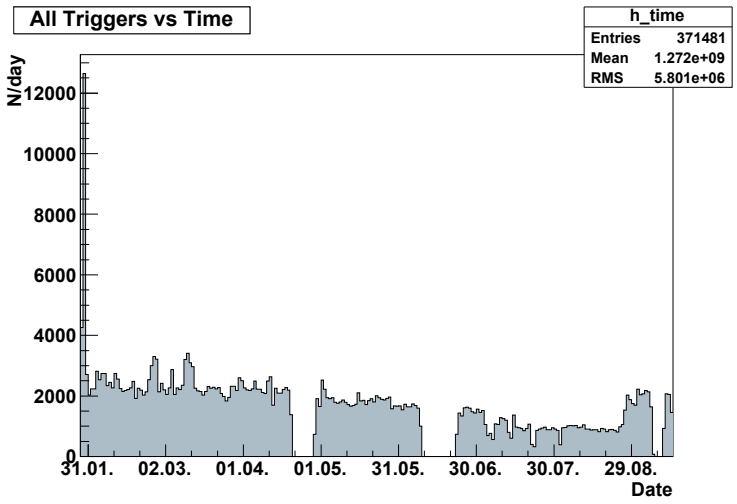

Figure 5.12: Trigger rate per day for the period of data taking. The spike in the beginning is correlated with events where almost all tubes of the detector showed an entry. Although still unexplained, the events are ignored by a noise cut of $n_{\mathrm{hit}} < 48$.

the density of the drift gas has been used. In the latter case, a measurement with ambient conditions similar to those at Gran Sasso has been performed. However, with this method, new systematic errors occur due to the different hardware used. Although it has been tried to account for different delays resulting from different cabling and slow control settings, results were not completely satisfactory. In a third attempt, the actual data from Gran Sasso was taken for a calibration in spite of the low statistics. In all three cases, the resolution and efficiency were well below the expected values from Hamburg conditions. Spatial resolutions around 360 µm were obtained. A worse resolution also leads to a rather large amount of falsely reconstructed tracks, especially for events containing only three hits and additional cross talk or δ electrons. Therefore it has been decided to apply a rather harsh cut on the reconstructed data. The total number of hits may not exceed the number of hits used by the fit by more than one.

5.2.2 Performance

Fig. 5.12 shows the number of triggers distributed by the trigger board each day. The rate started at a constant level of approximately 2000 triggers per day. It then slowly reclined during the summer—an effect which is connected to instabilities of the trigger. However, it suddenly rises again to the prior value in the end of August. During this period, maintenance was done at the detector. It can thus be assumed, that this effect is correlated with the work on the detector. As will be shown in detail later, the trigger system is not working properly and has to be replaced. Thus, this effect is not further studied.

To check the performance of the underground operation the distribution of hits in the single tubes and the number of events per day were investigated. Since the trigger rate is dominated by far from random coincidences of the PMT's dark noise ($\sim$ 1 coincidence per minute), most of the events do not contain any hit tube.

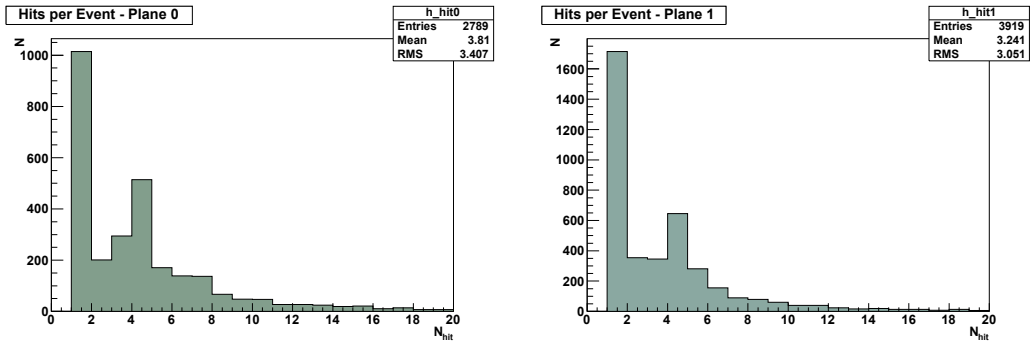

Figure 5.13: Number of hits per event for both 2D planes. Events with no hits were cut from the data. On can clearly identify a peak at four hits per event, which is expected from the layout of the detector. However, the distribution shows also events with more than ten hits. These are caused mainly by noise or multiple muon events.

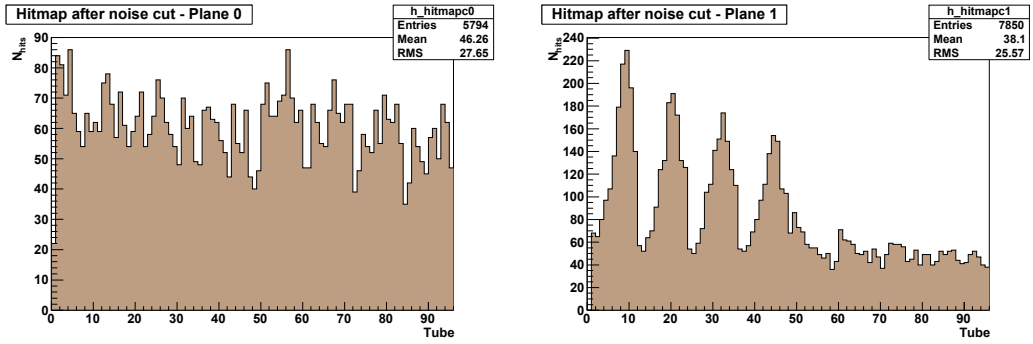

Figure 5.14: Hit map of all tubes in the CMT. The peaks in the $x-z$-plane (plane 1) can be explained by the poor trigger efficiency of trigger scintillators A and B.

Therefore a cut of $n_{\text{hits}} > 0$ is applied for each 2D plane.

The number of hits per event is shown in Fig. 5.13. As expected, a peak at $n_{\text{hit}} = 4$ is observed. However, the distributions show a rather long tail towards larger values. A large number of hits can occur when a track with a steep inclination crosses the detector. However, this cannot explain the extent of the tail in the distribution. By looking at single events, one finds that many of the events in question show fake hits probably occurring from cross talk and also δ electrons. A second cause for large values of n_{hit} are multiple muon events, where there is an expected average of eight hits per event (see also Fig.5.17).

Fig. 5.14 shows the hit maps for both 2D planes. All tubes except tube 0 in module 1.0 seem to be working fine. However, instead of a homogeneous distribution, four distinct peaks can be seen for the same module. These are a hint for a systematic error in the setup. The error source could be identified in a poor efficiency in some of the trigger scintillators, namely scintillators A and B (cf. Fig. 5.1). Due the the segmentation of the trigger plane, the characteristic shapes occur. The (presumably well working) trigger scintillators C and D are the small ones on the left facing the $x-z$-plane. Hence, tubes located at small x show significantly more hits (cf. Fig. C.1 for a channel map of each tube). The peak maximum reduces slightly for each layer of tubes the further they are away from the scintillator, but it also

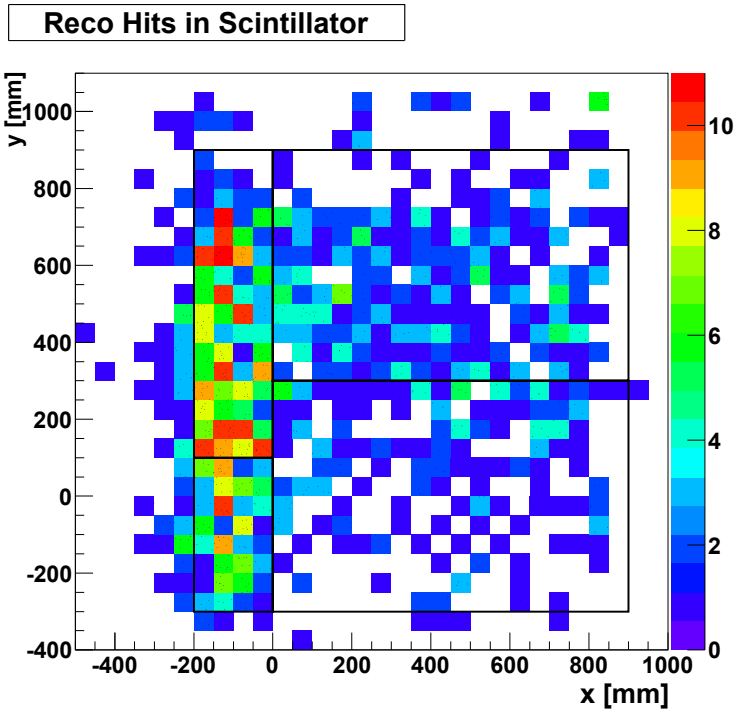

Figure 5.15: Intersection of reconstructed events with the $x-y$-plane at $z = 227\,\text{mm}$. This plane represents the trigger scintillator layer. The single scintillators are represented by the black rectangles (compare Fig. 5.1). Tracks intersect the plane at the black dots. The colored areas depict the number of tracks per $25\,\text{cm}^2$. One can clearly see a lower density at the larger scintillators, especially the lower right one. Also, the tracks are not distributed homogeneously within all scintillators. This leads to the assumption that some of the scintillators are malfunctioning.

smears out which is expected for inclined tracks. The number of hits then show a homogeneous distribution for the second module of the plane. However, the average number of hits of approximately 45 is below the according value of the $y-z$-plane, which has an average of 60 hits per tube. Since the latter plane is further away from the scintillator, less events would actually be expected here. This strengthens the hypothesis of a malfunctioning trigger scintillator. Scintillators C and D are spread homogeneously across the modules of the $y-z$-plane. Although they contribute to only 22% of the trigger surface, they seem to account for the majority of events. Comparing the the peaks of the first module in the hitmap of the $x-z$-plane with the level for the second module, one can estimate a reduction of the trigger rate by roughly a factor of three for the scintillators A and B. An efficiency of only one third of the two larger scintillators (accounting for 78% of the trigger surface) would lead to an overall efficiency of only $\frac{1}{3} \times 0.78 + 0.22 = 0.48$.

The assumption of a poor trigger efficiency can be confirmed by considering reconstructed tracks. The x and y coordinates at the level of the trigger plane ($z = 227\,\text{mm}$) were calculated and drawn in a scatter plot. The result is shown in Fig. 5.15. It shows the distribution of reconstructed tracks in the trigger scintillator plane. One can clearly see that the events are not distributed homogeneously. Obviously

Table 5.4: Comparison of simulated and real events for the 197.68 days of data taking. Values are presented for the requirement of at least 3 and 4 hits as well as a track in Borexino.

	$n_{\text{events},4}$	$n_{\text{events},3}$	$n_{\text{events,BX}}$
Real data	788	1647	392
MC data	1182	2372	897
Ratio	66.7%	69.4%	43.7%

one or more trigger scintillators are not working properly. This can be due to malfunctioning PMTs, broken light guides or a broken scintillator itself. Due to the extremely low muon flux inside the LNGS tunnel, it is hard to find the exact source of error. The smaller scintillators seem to perform much better than the larger ones. This is no surprise, since the latter ones are much older. The trigger efficiency can be deduced from a comparison of simulated and real events. The data presented in Tab. 5.3 corresponds to 197.68 days of data taking. The corresponding rates have been calculated for the simulated data presented in Section 5.1.3 and are compared in Tab. 5.4. Trigger efficiencies of 66.7% and 69.4% are found from data with a least four and three hits, respectively. This values are overestimated, since the number of hits in the real data includes also cross talk and hits from δ electrons as well as certain noise patterns (cf. Fig. E.2 in Appendix E) and only give an upper limit. Therefore, a third comparison has been made with the number of reconstructed events that go through both the CMT and Borexino. In this case, an efficiency of 43.7% is obtained. This value, on the other hand, now underestimates the true efficiency, since the reconstruction still lacks a sufficient calibration and can thus only be taken as a lower limit. Due to the poor trigger performance, it has been decided to completely replace the trigger by a new one as will be described briefly in Section 5.2.3.

5.2.3 Trigger Upgrade

Due to the poor performance of the current trigger system, a trigger update is necessary. It has been decided to use only one large, unsegmented plastic scintillator. To suppress false triggers from PMT dark noise, a coincidence of up to four PMTs will be used, each mounted on one corner of the scintillator. The basic layout of the new trigger is depicted in Fig. 5.16. For the scintillator, a polyvinyltoluene-based plastic has been chosen. The foreseen BC-408 scintillator from Saint Gobain Crystals is $116 \times 120\,\text{cm}^2 \times 2\,\text{cm}$ in dimensions. On each corner, Hamamatsu R8900U photo multipliers will be attached. The PMTs have a squared surface of 23.5 mm side length. At the time of writing, all components have been delivered and are currently prepared for installation. After thorough tests in Hamburg, a setup at Gran Sasso is foreseen for spring 2011.

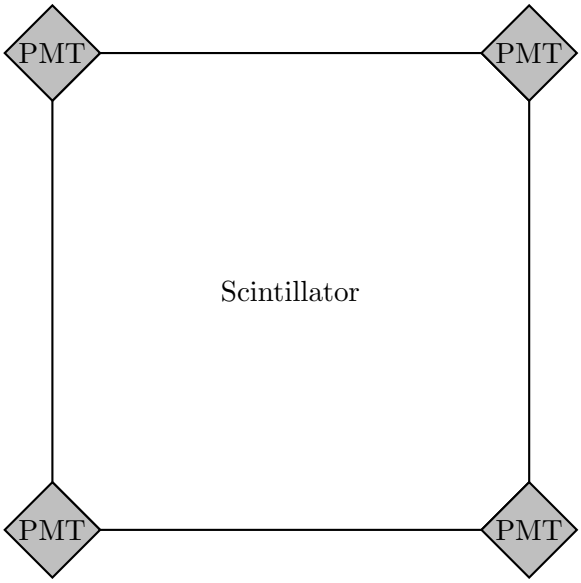

Figure 5.16: Trigger layout after the foreseen trigger update (not to scale).

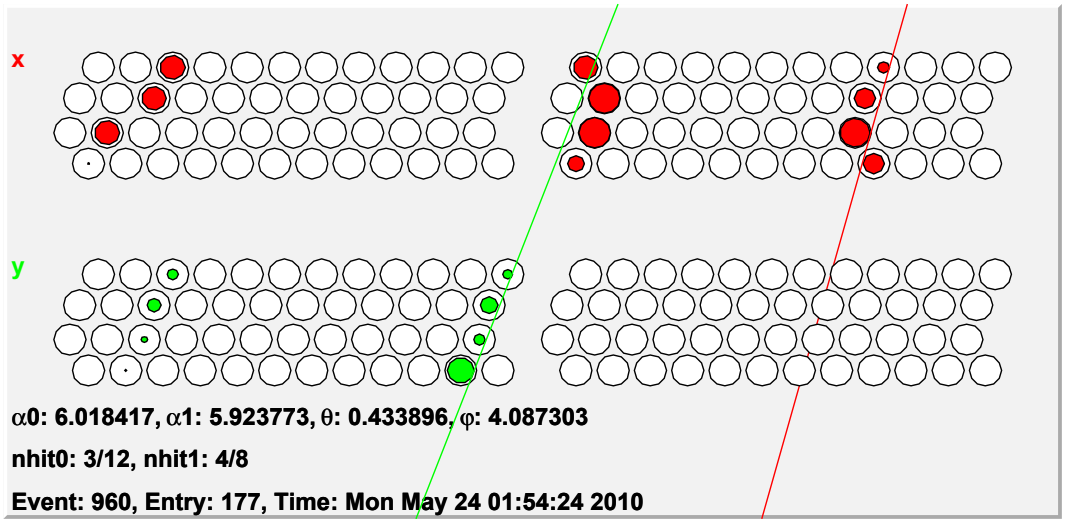

Figure 5.17: A multiple muon event in the CMT. Due to the setup of the detector, a distinct 3D reconstruction is not possible and the event has to be rejected.

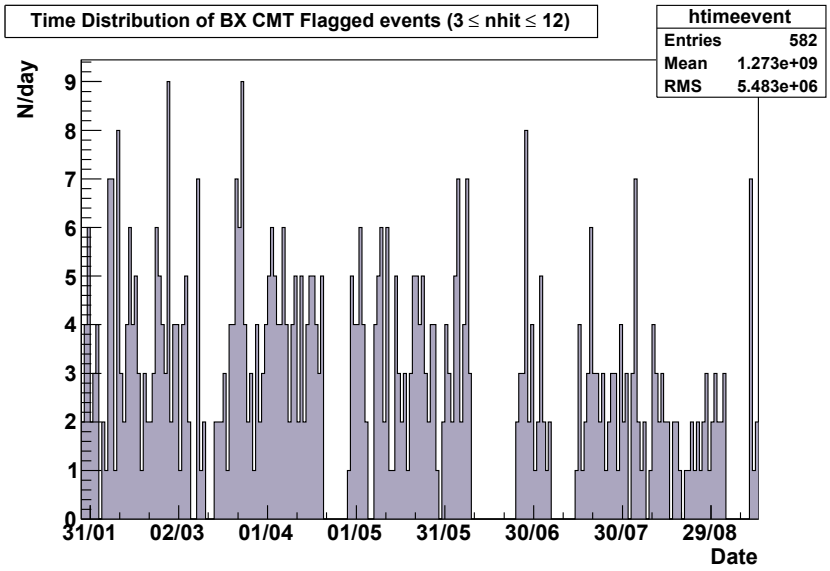

Figure 5.18: Time distribution of common events in Borexino and the CMT. A triggered signal is considered an event, if three or more, but no more than twelve tubes have been hit in each plane. The gaps in the distribution come from periods where the CMT did not take data.

5.3 Common Events with Borexino

Despite the poor trigger efficiency of roughly 50%, some tracks passing both the CMT and Borexino could be reconstructed.

Due to the trigger setup, events are also recorded when the track does not cross the CMT detector or passes only an insufficient number of tubes. To get a first estimate of which occurrences can be considered *true* events, the basic following cut is applied: In each 2D plane, at least three hits have to be recorded. Also, the maximum number of hits must not exceed twelve. The latter cut is mainly used to reduce noise events from the data. Fig. 5.18 shows the distribution of coincidence events over time. It can easily be seen that due to the malfunctioning trigger the daily number of events is well below the expected value of ~ 9.6 events per day from the simulation. Altogether, there are 582 events qualifying for reconstruction. However, the basic event selection based on the number of hits also includes certain noise patterns so that in the end only 392 events could be reconstructed. Using these events, a first analysis of the Borexino muon tracking was performed.

5.3.1 Borexino Data Matching

Borexino and CMT data are matched on an event by event basis using the timestamp of each event. As mentioned before, the CMT trigger signal is also sent to the Borexino DAQ, where a flag is set in case of a common event. From the Borexino data, all events with a CMT flag are selected. For each event, timestamp, run number and event number are extracted into a text file.

The raw CMT data is converted to a `ROOT` file for each run. An iteration over both

the CMT data file and the Borexino text file is now done simultaneously. For each iteration the timestamps $t_{\mathrm{CMT},i}$ and $t_{\mathrm{BX},j}$ for the ith CMT and the jth Borexino event are compared, starting at the first events $i = j = 0$. The event number for the data set with the smaller timestamp is increased for the next iteration. If the two timestamps match within one second, the combined event data is written to file. The timestamps do not necessarily have to be identical, since the CMT timestamp is only taken once per second whereas Borexino uses a GPS timestamp. However, considering the low event rates, requiring a maximum difference of 1 second is sufficient for a correct data matching.

The number of Borexino events with CMT flag does not necessarily match the number of CMT events. A muon might pass the CMT trigger and then bypass the CMT before crossing Borexino, causing a BX CMT flag and an empty (nhits=0) CMT event. On the other hand, tracks that also go through Borexino can occur in the CMT without a corresponding flag in Borexino, e.g. when the Borexino DAQ is offline while the CMT is taking data.

The combined data is written into a new `ROOT` file with the same tree structure of `TData` as described in Section 3.5. However, the tree is extended by two branches `bxrun` and `bxevent`, namely the Borexino run and event number.

The combined data file can now be reconstructed using `cmtrack`. A special parameter tells the program to keep the Borexino event information during the reconstruction and to include it in the output file. Only events that can be fully reconstructed are written to file.

A `ROOT` macro is now used to create a script which can then be launched to process all corresponding Borexino events on the Borexino cluster. Each single event is retrieved from the Borexino data storage and—in a first step—saved to a single file, keeping the specific Borexino data structure (see [78] for details). After all events have been processed, the single files are merged, together with the reconstructed CMT data. Thus, all information for common Borexino and CMT events are gathered in one file which can now easily be used for analysis.

A total number of 392 common events could be reconstructed. Tab. 5.5 shows the number of events for which there was also a muon track reconstructed by one of the Borexino muon tracking algorithms. Typical common events are depicted in Fig 5.19. Most events show a good agreement for the different trackings. However, also differences can be observed. These are mainly seen in events where the Borexino tracking shows ambiguities in the different tracking algorithms. Very interestingly, for some events a parallel track is reconstructed by the CMT with respect to the Borexino tracking. This occurs when two muons from a shower hit the detectors. These muons are correlated and in general point in a similar direction. One hits Borexino, whereas the second one hits the CMT and misses Borexino. A detailed comparison of common events will be presented in the next chapter.

5.4 Comparison of CMT and Borexino Muon Tracks

Once the CMT and Borexino data are matched, a comparison of reconstructed tracks is possible. As described in Section 4.3.4, three methods to reconstruct muon tracks are used in Borexino: tracking with the outer detector only (OD tracking), the inner detector only (ID tracking) and a combined analysis (global tracking). The

Table 5.5: Number of reconstructed events for different coincidence criteria with Borexino.

Criteria	N
BX flag	392
OD track	125
ID track	82
Global track	125

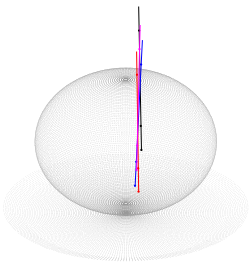

(a) Common Track

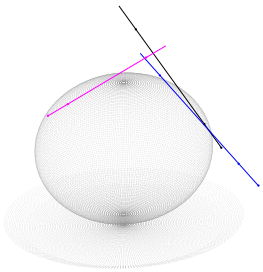

(b) False Tracking

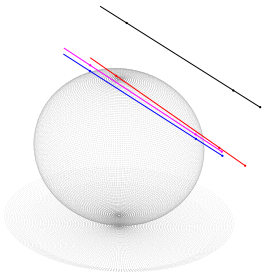

(c) Dimuon Tracking

Figure 5.19: Common event display of Borexino and CMT tracks. The black line is the track as reconstructed by the CMT. The colored lines correspond to the different Borexino trackings (blue: OD tracking, red: ID tracking, pink: global tracking). Figure (a) shows a good agreement between tracks. This is the case for most events. However, events with large difference also occur. They result mainly from errors in the Borexino tracking (Fig. (b)) where one of the trackings reconstructs the right coordinates whereas the other tracking fails or from multi muon events (Fig. (c)), where the CMT sees a parallel track to that reconstructed by Borexino.

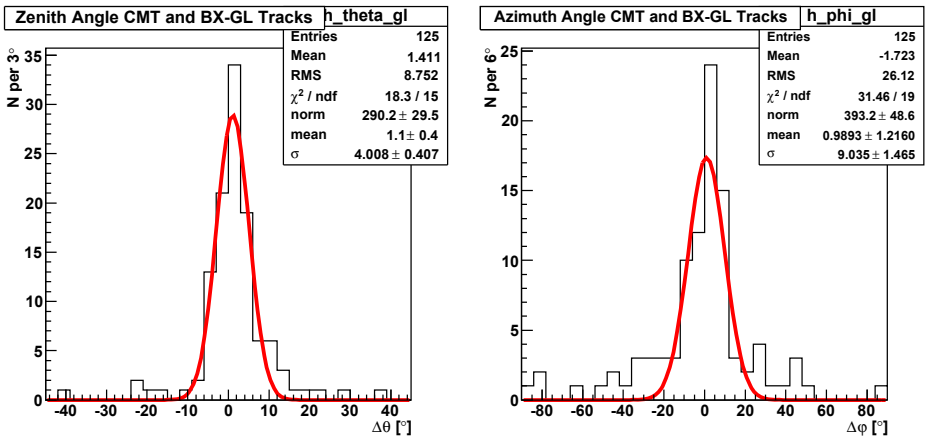

Figure 5.20: Comparison of reconstructed polar and azimuth angles for the CMT and Borexino global tracking.

collected CMT data has been compared to all three tracking methods. Since the CMT resolution exceeds the Borexino resolution by far, the CMT track coordinates are considered to be the *true* track coordinates. Hence, the resolution of the Borexino tracking can be determined by a comparison.

Due to the low trigger efficiency, only 392 common events of the CMT and Borexino remain. The event sample had to be reduced further. Some of the events come from multiple muon hits as depicted in Fig. 5.17, where a 3D reconstruction cannot be done without ambiguities. Therefore these events were not used in the analysis. Also, many events are ignored due to the cut on the number of used hits introduced in Section 5.2.1. However, most of these events can be used once a better calibration is feasible. In addition to the reduction of events due to the CMT data quality, not all events with a BX flag have an according reconstructed muon track in Borexino. But although the overall statistics are rather poor they allow to do a first comparison of the combined data.

For the analysis, both the angular and lateral resolution have been determined. For each common event, track parameters like the polar angle θ and the azimuth angle φ were compared. Fig. 5.20 shows the distribution of $\Delta\theta$ and $\Delta\varphi$ obtained from the differences between the CMT and the Borexino global tracking. A clear peak around 0 can be observed for both distributions. The peaks have been fitted by a Gaussian and the resulting σ gives a measure for the angular resolution. Results for all tracking algorithms are presented in Tab. 5.6. The values mostly range between 3 and 9 degrees.

Instead of looking at the polar and azimuth angles, one can also investigate the intermediate angle α between the tracks $\vec{t}_i$ from the different reconstructions. It is simply given by

$$\begin{aligned} &\vec{t}_{\mathrm{bx}} \cdot \vec{t}_{\mathrm{cmt}} = |\vec{t}_{\mathrm{bx}}||\vec{t}_{\mathrm{cmt}}| \cos\alpha \\ \Leftrightarrow &\alpha = \cos^{-1}\left(\sin\theta_{\mathrm{bx}} \sin\theta_{\mathrm{cmt}} (\cos\varphi_{\mathrm{bx}} \cos\varphi_{\mathrm{cmt}} + \sin\varphi_{\mathrm{bx}} \sin\varphi_{\mathrm{cmt}}) + \cos\theta_{\mathrm{bx}} \cos\theta_{\mathrm{cmt}}\right). \end{aligned}$$

An exemplary plot for the distribution of intermediate angles between the CMT and Borexino global tracking is shown in Fig. 5.21. The values have been weighted by

Table 5.6: Angular and lateral resolutions σ resulting from the track comparison of the CMT to the different Borexino trackings.

	σ_θ [°]	σ_φ [°]	σ_α [°]	σ_x [cm]	σ_y [cm]	σ_I [cm]	$\bar{d}_I$ [cm]
OD	3.0 ± 0.3	9.1 ± 1.3	4.00 ± 0.09	62 ± 4	62 ± 4	50 ± 2	77 ± 12
ID	6.6 ± 1.1	25 ± 5	4.64 ± 0.16	67 ± 6	34 ± 3	48 ± 5	75 ± 9
global	4.0 ± 0.4	9.0 ± 1.5	3.76 ± 0.08	48 ± 3	57 ± 4	47 ± 2	52 ± 7

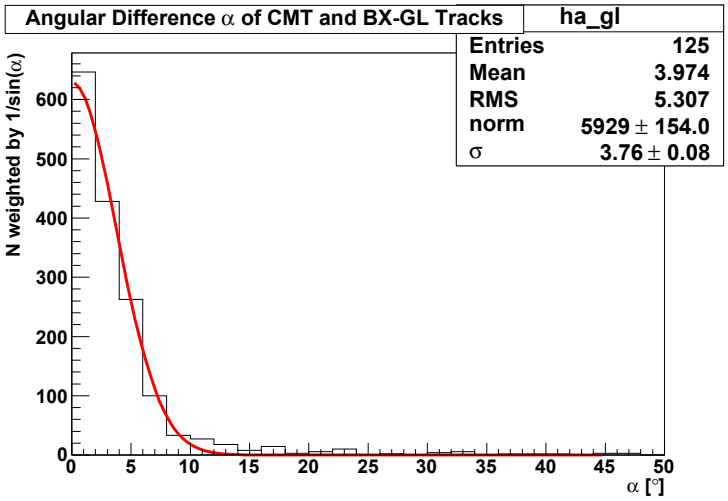

Figure 5.21: Intermediate angle α between muon tracks reconstructed by the CMT and the global Borexino tracking. The entries have been scaled by $1/\sin\alpha$ to account for the solid angle.

$1/\sin\alpha$ to account for the solid angle. The angular resolution has been found to be of the order of 4°. Results for all trackings are also presented in Tab. 5.6.

In the next step the lateral resolution has been determined. Again, different methods were tried. Since the muons in consideration originate from cosmic radiation, it is assumed that all tracks point downwards. For a spatial comparison, the x- and y-coordinates of the track penetrating the $z = 0$ plane are used. They are calculated for both the CMT and Borexino tracking and their difference is histogrammed. The result for the ID tracking is depicted in Fig. 5.22. The distributions were fitted again by a Gaussian with σ being a measure for the resolution. Results are presented in Tab.5.6. This method does not take into account the inclination of the individual tracks. Especially for a large θ, uncertainties in the polar angle have a strong effect on Δx and Δy. Therefore, the impact parameter I has also been investigated to get an absolute measure. I is defined as the distance of the track to the Borexino center. It has been calculated for all trackings and the difference ΔI to the CMT tracking was again histogrammed and fitted by a Gaussian as shown in Fig. 5.23 for the global tracking.

The impact parameter itself only gives an absolute value for the distance if the track to the center of the SSS. Comparing the impact parameters from the different

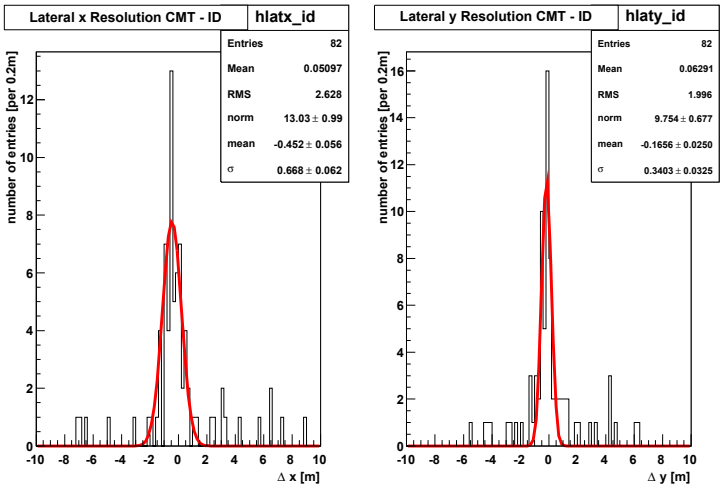

Figure 5.22: Lateral resolution Δx and Δy from the comparison of CMT and ID tracking

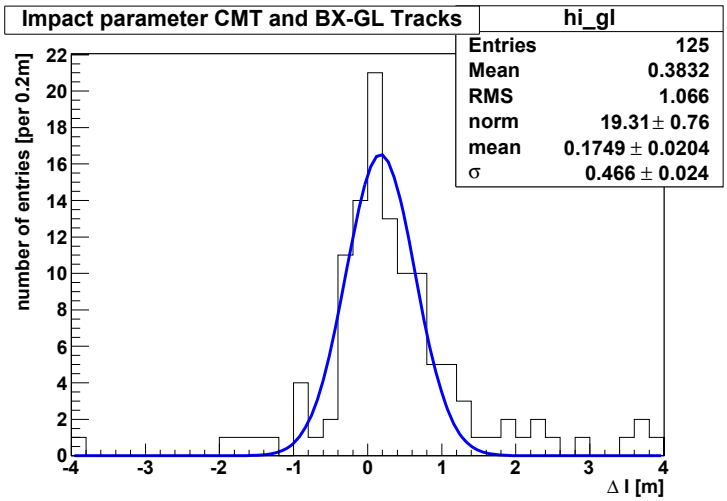

Figure 5.23: Lateral resolution of the impact parameter I from the comparison of CMT and global tracking. The slight shift of the distribution is explained by the fact, that the impact parameter of tracks reconstructed by the CMT can lie outside of the actual Borexino vessel and can thus obtain larger values.

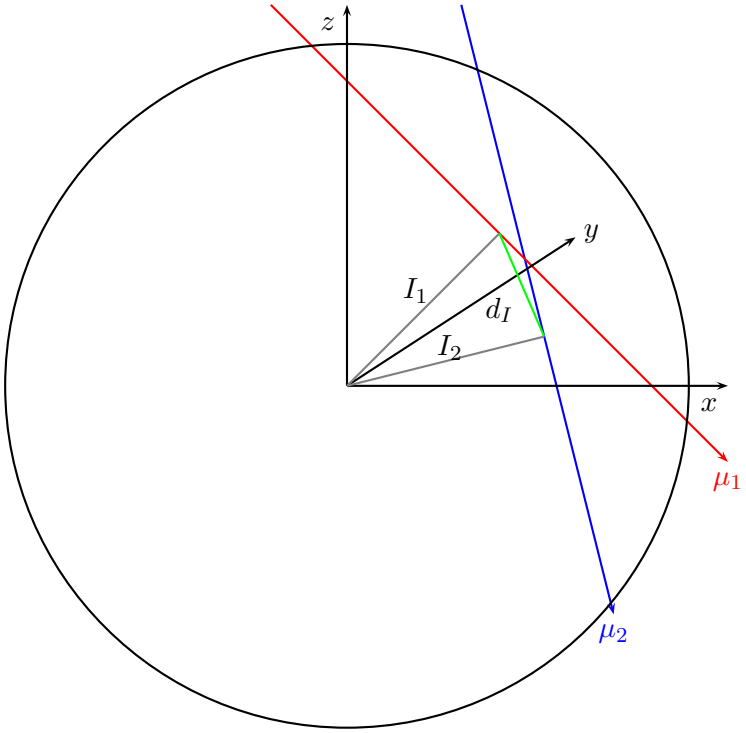

Figure 5.24: Example of relative positions of the reconstruction of a muon track by both the CMT and Borexino in the coordinate system of the SSS. I is the impact parameter of each track. For the determination of the lateral resolution, the distance d_I (green line) between the points closest to the center for each track is calculated.

trackings does not take into account their relative position. To study this effect, the closest point to the center of the SSS of the tracks reconstructed by Borexino and the CMT have been determined as shown in Fig. 5.24 and the distances d_I between them have been calculated. The distribution of d_I is depicted in Fig. 5.25 for the Borexino global tracking. A clear peak can be seen with a mean value of $\bar{d_I}$ giving a measure of the lateral resolution. All methods lead to a lateral resolution around 50 cm with the results using the impact parameter comparison being slightly better and more consistent than the other ones.

5.5 CNGS Rock Muons

The CMT is based on the drift tube technology developed for the OPERA detector. OPERA searches for ν_τ appearance in a ν_μ beam [79]. The CNGS[2] ν_μ-beam is generated as described in Section 2.4.6 at a distance of 732 km from Gran Sasso at CERN, focused on the Hall C where both OPERA and Borexino are located. The beam travels through the Earth before it arrives at Gran Sasso at an inclination of approximately -3.5 ° [80]. Neutrinos in the CNGS beam have a mean energy of 17 GeV. Although the cross section for neutrino interactions is rather small, some

[2]CNGS CERN Neutrinos to Gran Sasso

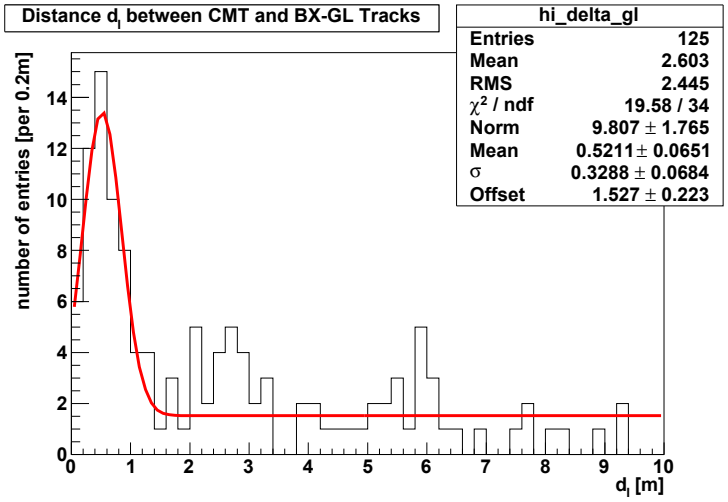

Figure 5.25: Distances d_I between the impact parameter as reconstructed by the CMT and the BX global tracking. A distinct peak can be seen around 0.5 m. This corresponds to the average distance of the tracks and gives a measure for the lateral resolution. Furthermore, a constant offset can be seen, which originates from false reconstructed tracks randomly distributed. The distribution has been fitted with a Gaussian plus a constant offset.

interact with the surrounding rock of the Gran Sasso massive producing muons. Thus it can occur that such a *rock muon* is created in the rock in front of the Borexino detector and then passes both Borexino and OPERA. OPERA reconstructs these tracks with a high precision [58]. These tracks can also be used to test the Borexino muon reconstruction.

The OPERA PT[3] uses the drift tube technology described in Section 3.1. Due to its setup it is only capable of reconstructing 2D tracks. However, the OPERA detector is made out of more than just the PT. Together with information from RPCs[4] and a target tracker based on plastic scintillator strips, a 3D track is reconstructed. For a detailed description of the OPERA detector and the 2D track reconstruction see [58, 79]. One major requirement to reduce background in OPERA is an exact time synchronization with the CNGS. CNGS neutrinos are not produced continuously, but rather in bunches at discrete times. By knowing the exact timing information it is possible to apply a cut on *on-time events* thus reducing most background. Conveniently, the CNGS *"OnTimeStamp"* is also distributed to the Borexino DAQ.

For a combined analysis all reconstructed on-time tracks that entered the OPERA detector from either the front or side have been extracted from the OPERA data. This has been done for the 2008, 2009 and the beginning of the 2010 runs. A collection of CNGS on-time events could be easily extracted also from the Borexino data. Events from both detectors were then matched by the timestamp information similar to the CMT events. Altogether 2291 common events were found.

For the combined analysis all track information was transferred into the Borexino

[3]PT Precision Tracker
[4]RPC resistive plate chamber

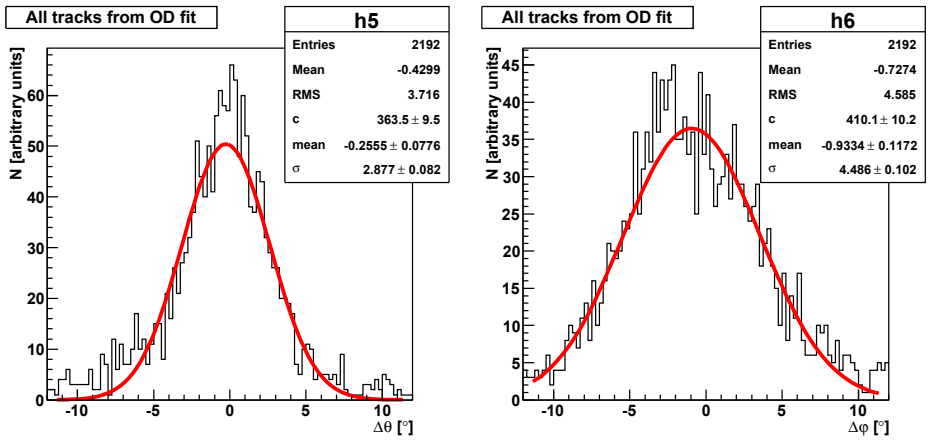

Figure 5.26: Polar and azimuth angle differences for muon tracks reconstructed in both OPERA and Borexino

Table 5.7: Borexino muon tracking resolution determined by the comparison with OPERA rock muons

Angle	σ [°] (OD)	σ [°] (ID)	σ [°] (GL)
θ	2.88 ± 0.08	4.86 ± 0.16	3.01 ± 0.12
φ	4.49 ± 0.10	4.76 ± 0.14	4.11 ± 0.10
α	3.75 ± 0.02	3.70 ± 0.04	2.63 ± 0.02

coordinate system. For a detailed description of the coordinate transformation see Appendix D.

5.5.1 Direct Angular Comparison

For a direct comparison of the tracks reconstructed by Borexino and OPERA for the same muon, the azimuth and polar angles φ and θ are obtained for all trackings. The distribution of differences between the corresponding angles is shown in Fig. 5.26 exemplarily for the OD tracking. Performing a Gaussian fit gives a measure for the angular resolution of the Borexino reconstruction. The results are presented in Tab. 5.7. This shows excellent values for θ, however, the resolution of φ is rather poor. This can be explained by the method how φ is determined in Borexino: muon tracks are determined by their entry and exit points to the detector. Since the detector is spherical, small uncertainties in the determination of these points lead to large uncertainties in φ around the poles. This could be accounted for e.g. by looking at a θ-dependency of σ_φ.

However, another analysis is chosen; the absolute angle α between both tracks $\vec{t}$ is determined. This can be done as follows:

$$\begin{aligned} &\vec{t}_{\mathrm{bx}} \cdot \vec{t}_{\mathrm{op}} = |\vec{t}_{\mathrm{bx}}||\vec{t}_{\mathrm{op}}| \cos\alpha \\ \Leftrightarrow &\alpha = \cos^{-1}\left(\sin\theta_{\mathrm{bx}} \sin\theta_{\mathrm{op}} (\cos\varphi_{\mathrm{bx}} \cos\varphi_{\mathrm{op}} + \sin\varphi_{\mathrm{bx}} \sin\varphi_{\mathrm{op}}) + \cos\theta_{\mathrm{bx}} \cos\theta_{\mathrm{op}}\right) \end{aligned}$$

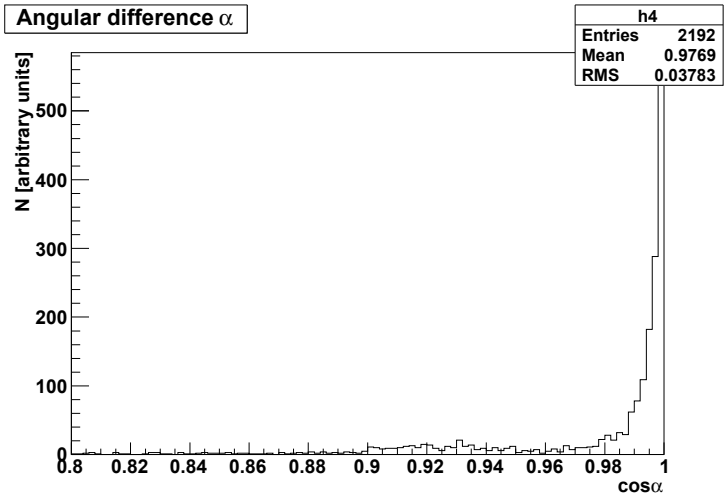

Figure 5.27: Comparison of muon tracks reconstructed by both Borexino and OPERA. The angle α is the angular difference between the muon track as it was reconstructed in the Borexino OD and the Track reconstructed in OPERA.

Fig. 5.27 shows the distribution of $\cos\alpha$. One can clearly see a peak towards $\cos\alpha = 1$, that is for $\alpha = 0$. To obtain an angular resolution, a look at α is necessary. However, due to the the solid angle merely looking at α this would underestimate small angles. Instead, all values of α are weighted by $\frac{1}{\sin\alpha}$ and then histogrammed. The result is shown in Fig. 5.28. Since no reference direction can be determined, α has to be always positive. This distribution can now be fitted by a Gaussian with $\sigma_\alpha = 3.75°$. This is an excellent result for the Borexino track reconstruction and in accordance with the results obtained by the CMT.

5.5.2 Momentum Dependency

The analysis for the angular difference α was repeated several times applying different cuts on the particle's momentum p as measured by OPERA. Interestingly, the resolution improves for high energetic particles. This can be clearly seen in Fig. 5.29, where the distribution of α is shown for different minimal momenta. This can be explained by the multiple scattering of the muons on their way between Borexino and OPERA. Lower energetic particles are effected more by scattering processes than high energetic ones. However, this indicates that the resolution of the Borexino tracking is underestimated in general since the reference muon track as reconstructed by OPERA is not necessarily true within Borexino due to multiple scattering.

5.5.3 Spatial Comparison

Common events from OPERA and Borexino were also analyzed regarding spatial track coordinates. For this a plane within Borexino was chosen as a reference. For convenience the $x = 0$ plane was chosen. This is a disk in the center of the detector. All CNGS muon tracks crossing the detector should hence also cross this plane

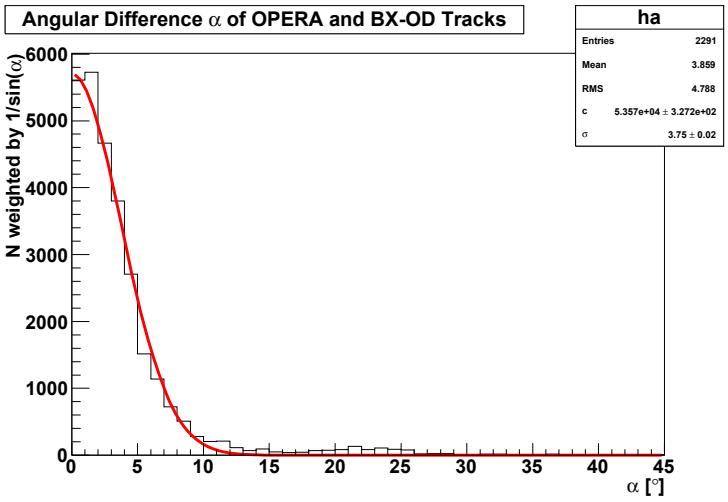

Figure 5.28: Weighted comparison of the angular difference α between OPERA and Borexino OD reconstructed muon tracks.

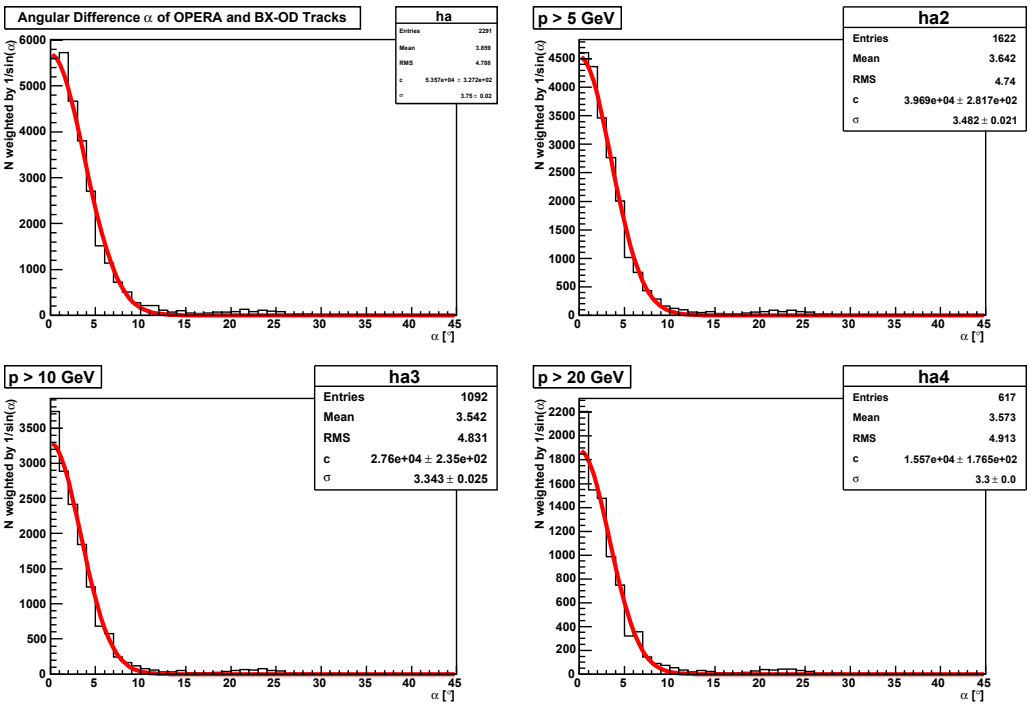

Figure 5.29: Dependency of the angular difference α on the muons momentum p as measured by OPERA

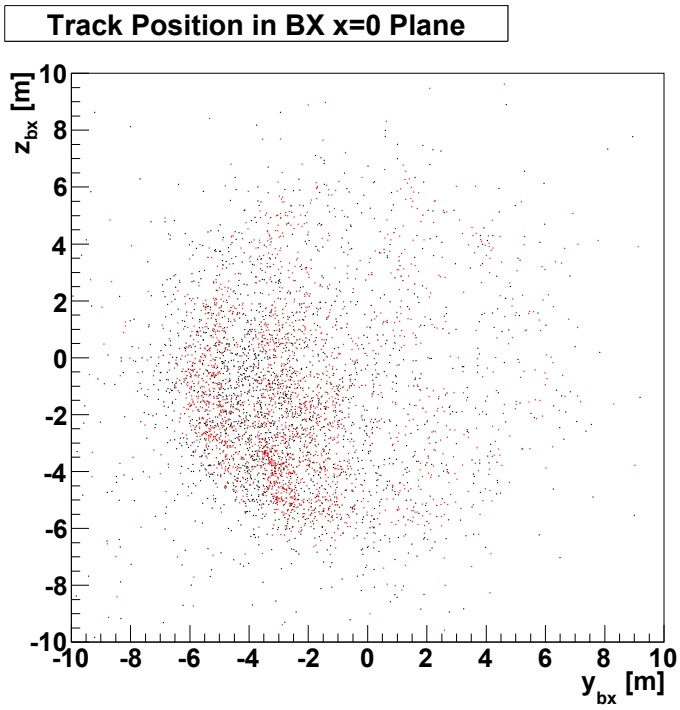

Figure 5.30: Muon track position at the central disk of the Borexino detector ($x = 0$) Black dots mark the reconstruction from OPERA whereas red dots are from the Borexino global fit. One can clearly see the shape of the Borexino sphere as well as the rectangular shape of the OPERA detector in the lower left corner.

Table 5.8: Spatial resolution of the Borexino global muon tracking. The results get better for high energetic muons. Also, taking only IV muons (nhits>7000) improves the resolution.

Value	Cut	σ [m]
Δy	-	0.963
Δz	-	1.125
Δy	$p > 50\,\mathrm{GeV}$	0.513
Δz	$p > 50\,\mathrm{GeV}$	0.828
Δy	$p > 50\,\mathrm{GeV}$, nhits>7000	0.377
Δz	$p > 50\,\mathrm{GeV}$, nhits>7000	0.553

almost perpendicularly. Fig. 5.30 shows the intersections of muons within this plane as reconstructed by both the OPERA detector (black dots) and Borexino (red dots). The depiction resembles a view along the CNGS beam direction. Most muons travel in a direction close to the CNGS beam axis. One can clearly recognize both the Borexino sphere and the shape of the OPERA detector in the *muon light*.

For a more qualitative analysis, the differences of the y and z coordinates for both track reconstructions are taken into account. The distributions of Δy and Δz are shown in Fig. 5.31. Besides the spatial resolution one can also deduce a possible misalignment of both detectors from these values. A shift in y and z simply moves the mean value of the corresponding distributions. Due to the small inclination angle of $\sim 3.5^\circ$ of a typical rock muon track and the large distance of approximately 60 m between the detectors, the method is not sensitive to a possible shift in x. The distribution could be fitted by a Voigtian, i.e. a convolution of a Gaussian and a Breit-Wigner distribution. The spatial resolution is then given by the FWHM/2.35.

An even larger dependency of the muon's momentum can be observed for the spatial resolution as can be seen in Fig. 5.31. The results are much improved by only considering muons that passed the Borexino inner vessel (nhits>7000 in Borexino). All values are summarized in Tab. 5.8. Comparing the results to the values obtained from the CMT analysis shows a good agreement for all trackings.

5.6 Future Analysis

The presented analysis shows the basic functionality of both the CMT and the Borexino tracking. Once the CMT trigger is replaced and enough statistics are gathered for a better calibration, the analysis of common events will improve significantly. It is foreseen to include the CMT data directly in the Borexino reconstruction. Once the CMT yields satisfactory results, further studies on the Borexino tracking can begin. The reason for different results of the three Borexino trackings can be investigated when the true track is known. CMT tracks that go through Borexino without a Borexino track reconstruction can be used to identify why no reconstruction was done and thus improve the Borexino tracking efficiency.

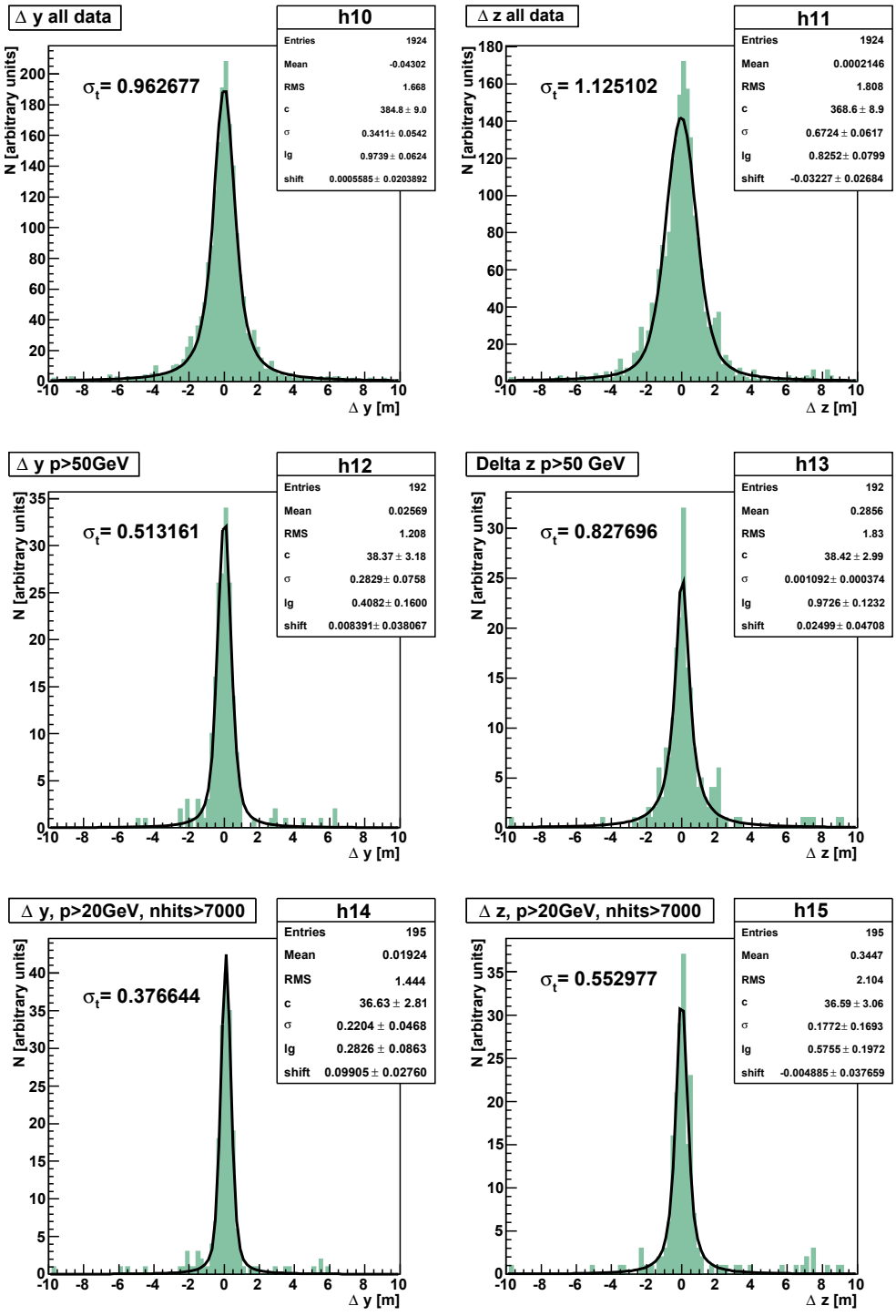

Figure 5.31: Spatial resolution of the Borexino muon reconstruction. The total resolution σ_t is derived from the FWHM

Chapter 6

Summary and Outlook

The spectroscopic real time detection of low energetic ^{7}Be solar neutrinos has recently been achieved for the first time by the Borexino experiment. Together with the measurement of the ^{8}B solar neutrino flux, the borders of the transition region between 1 and 10 MeV of the MSW effect could now be addressed by a single experiment supporting the model of matter enhanced oscillations. The experimental determination of the solar neutrino fluxes resulting from different fusion processes in the Sun allows to test the input parameters of the SSM such as the metallicity or solar composition.

^{7}Be and ^{8}B neutrinos mainly cover the borders of the transition region of the MSW effect. A measurement of the flux of solar neutrinos with intermediate energies around 1 MeV would allow to give further constraints on the different models for solar neutrino oscillations in matter. Whereas the MSW-LMA model seems to be favored by Borexino in combination with the other solar oscillation experiments, recent analyses including also the KamLAND data see hints for possible non standard interactions.

Neutrinos from the *pep* and CNO solar fusion processes cover the intermediate energies in the transition region. Measuring for the first time the flux of CNO neutrinos would also allow for the determination of the contribution of the CNO cycle to the energy production in the Sun. However, in Borexino their energy regime is dominated by the uncorrelated decays of cosmogenic induced ^{11}C nuclei by at least one order of magnitude. To distinguish these decays from the neutrino signal, a precise tracking of the incident muons is necessary. For the Borexino experiment, a sophisticated muon tracking procedure based on the PMT timing information is used.

The compact muon tracker presented in this work exceeds the performance of the Borexino tracking by far and can hence be used to test it. The CMT has been built from drift tube modules formerly used for calibration measurements for the OPERA experiment. A modification of the setup done within this thesis allows for a precise three dimensional reconstruction of muon tracks. An independent slow control software based on Linux has been developed, allowing a remote control of all detector components via a simple terminal connection. A new software package for alignment, calibration, and event processing including 3D track reconstruction has been introduced. With the CMT setup, an angular resolution of 4.65 mrad and a spatial resolution of 270 µm have been reached.

To determine the Borexino tracking resolution, the tracker has been installed on top of the experiment's steel dome at the LNGS underground laboratory. Due to its small size the CMT can merely sample a small fraction of the muons crossing Borexino. Comparing these events with the tracks reconstructed in Borexino yields an angular resolution of approximately 4° and a spatial resolution of approximately 50 cm of the Borexino tracking. A similar analysis was done using reference tracks of CNGS rock muons reconstructed by the OPERA experiment yielding comparable results.

Data taking with the CMT is still ongoing and will improve significantly after a trigger upgrade foreseen for spring 2011. With higher statistics, an improved calibration will be possible. The events common to Borexino and the CMT have been matched manually so far. Once the new trigger is installed and the calibration improved, it is planned to include the CMT data directly into to Borexino data processing. In this way, a comparison of CMT and Borexino tracks becomes much easier and allows for an identification of possible systematic errors in the Borexino tracking.

Appendix A

Slow Control Software

The slow control software developed in this thesis is based on a simple shell script that can be controlled through dialogs. The kernel module for controlling the PEAK USB CAN adapter creates a device `/dev/pcan32` which can be addresses through text messages. The slow control software converts the user input into CAN text messages and sends them to the device. For testing, the device address can be changed to a temporary file; the CAN messages are then stored in the file instead of being sent to the device. CAN responses can also be accessed through the device `/dev/pcan32`. Once the control software is started, a background process watches the device and saves all messages in a temporary file. That way, the slow control software has access to all response messages.

The different slow control settings are managed in environment variables. The different variables used and their default values are presented in Tab. A.1. The values can be modified through the dialogs. To apply the settings to the detector, values have to be sent. The CAN messages are only generated and sent when the *send* option is chosen.

Table A.1: Variables that can be set by the slow control and their default values for the tracker setup.

Variable	Description	Default
CRATE	Crates in use	"0"
SLOT	Slots in use	"1 5"
TPDELAY	Delay for testpulse	'200'
THRESH	Signal threshold in mV	'50'
THR_AMP	Send single threshold to chosen amplifier	0
THR_TUBE	Send single threshold to chosen tube	0
NB_TP	Number of testpulses	'100'
TP_PAUSE	Time between testpulses	'0.01'
TP_ODD	Switch for testpulses on odd channels	"on"
TP_EVEN	Switch for testpulses on even channels	"on"
TRM1	Mask for OTB input channel 1	"on"
TRM2	Mask for OTB input channel 2	"on"
TRM3	Mask for OTB input channel 3	"off"
TRM4	Mask for OTB input channel 4	"off"
TRM5	Mask for OTB input channel 5	"off"
TR_MASK	Corresponding HEX value for OTB mask	3
TRTPM1	Apply OTB testpulse to input channel 1	"on"
TRTPM2	Apply OTB testpulse to input channel 2	"on"
TRTPM3	Apply OTB testpulse to input channel 3	"on"
TRTPM4	Apply OTB testpulse to input channel 4	"on"
TRTPM5	Apply OTB testpulse to input channel 5	"on"
TRTP_MASK	Trigger testpulse mask for input channels (hex)	0x31
TRS0	Select trigger configuration 2/3	"on"
TRS1	Select trigger configuration 3/4	"off"
TRS2	Select trigger configuration 4/5	"off"
TRS3	Select trigger configuration random	"off"
TR_SEL	HEX value for trigger configuration	0
TR_CRATE	Crate of triggerboard	0
TR_DELAY	Delay of trigger in units of 5 ns	200
TR_PULSE	Pulse width of trigger signal	200
TTP_PAUSE	Time between trigger testpulses	'0.01'
NB_TTP	Number of trigger testpulses	'100'

Appendix B

Binary TDC Data

The TDC data has a 32 bit structure. For most values it is sufficient to look at then in hexadecimal mode, which will be used within this chapter unless otherwise mentioned.

A **new cycle** is indicated by two 32 bit sequences. The first indicates the new cycle:

$$\texttt{0x 110d}\ \underbrace{\texttt{xxxx}}_{\text{cyclenumber}}$$

followed by

$$\texttt{0x}\ \underbrace{\texttt{xxxx xxxx}}_{\text{timestamp}}$$

An **event** (without zero suppression) consists of 99 32-bit sequences starting with an event indicator:

$$\texttt{0x 1109}\ \underbrace{\texttt{xxxx}}_{\text{cyclenumber}}$$

followed by

$$\texttt{0x}\ \underbrace{\texttt{xxxx xxxx}}_{\text{timestamp}}$$

After that follows a 32-bit sequence for every channel (hence 96 sequences). These are encoded as follows:

$$\texttt{0x 22}\ \underbrace{\texttt{xx}}_{\text{channel}}\ \underbrace{\texttt{x}}_{\texttt{bbbb}}\ \underbrace{\texttt{xxx}}_{\text{tdcvalue}}$$

where the four unexplained bits can be accounted for hits and width information as follows:

$$\underbrace{\texttt{bb}}_{\text{hit}}\ \underbrace{\texttt{bb}}_{\text{width}}$$

The different values stand for: `00`: hit, `01`: no hit, `10`: OV ROZ and `11`: OV ALU for the hits and `00`: no width, `01`: small, `10`: medium and `11` large for the width

respectively. The channel numbers are values between 1 and 96 in the binary data. During data read out they are decreased by 1, so that the resulting channel number go from 0 to 95. The last channel sequence is followed by

```
0x 4400 0000
```

indicating the end of the event. This is followed either by the next event or a new cycle.

Appendix C

CMT Setup at Gran Sasso

In the Appendix, some schematic drawings for the better understanding of the current CMT setup are presented. Fig. fig:bxcmtmap depicts the channel mapping of the CMT. In Fig. C.2, the rotation of the CMT reference system with respect to the Borexino system is presented.

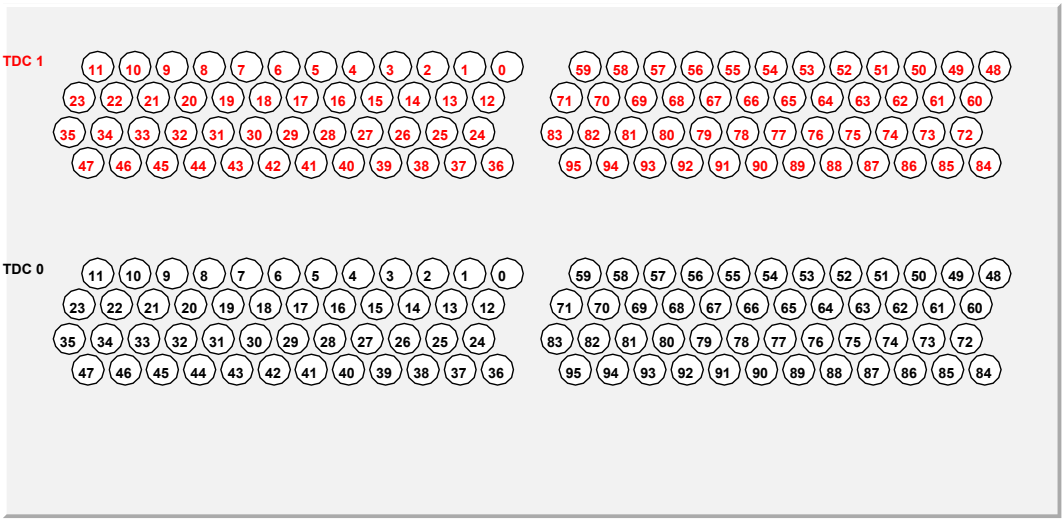

Figure C.1: Channel map for each tube for the current CMT setup.

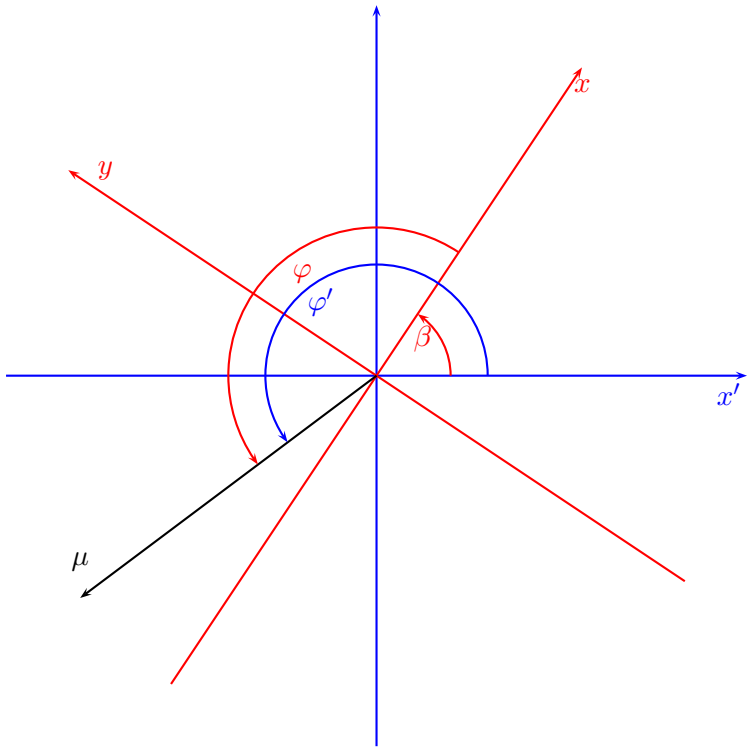

Figure C.2: Relative position of the CMT in the Borexino system. A muon track at an angle φ' in the BX coordinate system (blue) transforms to a muon with angle $\varphi = \varphi' - \beta$ in the CMT reference system.

Appendix D

Comparison of CNGS Tracks in Borexino and OPERA

As described in Section 5.5, a comparison of muons originating from the CNGS beam that have crossed both the Borexino and the OPERA detector has been done. This section summarizes the necessary coordinate transformations for this task.

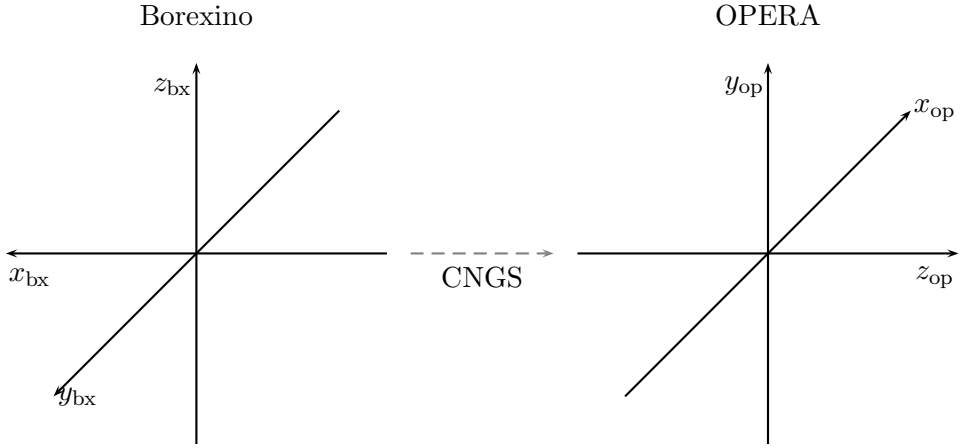

Figure D.1: Relative coordinate systems of Borexino and OPERA

Both the Borexino and OPERA coordinate systems are shown in Fig. D.1. Since the muon tracks are to be compared within Borexino, the Borexino coordinate system is taken as the reference system. Assume, the offset between both detectors is Δx, Δy and Δz in the Borexino system, the transformation is trivial:

$$\begin{aligned} x &= x_{\mathrm{bx}} = \Delta x - z_{\mathrm{op}}, \\ y &= y_{\mathrm{bx}} = \Delta y - x_{\mathrm{op}}, \\ z &= z_{\mathrm{bx}} = \Delta z + y_{\mathrm{op}}. \end{aligned}$$

For each muon track, OPERA provides five parameters: one slope and the according z-intercept for each the $x-z$ and the $y-z$ plane: s_x, $x_{\mathrm{op},0}$, s_y and $y_{\mathrm{op},0}$ respectively as well as the inverse momentum $\frac{1}{p}$. The z-intercept is not given for $z_{\mathrm{op}} = 0$, instead

the z-coordinate $z_{\mathrm{op},0}$ of the first hit in the detector is used. This coordinate is determined by looping over all hits thus finding the smallest z. For each projection in the $x-z$ and $y-z$ plane the following 2D parametrization can be used:

$$\begin{aligned} x_{\mathrm{op}} &= s_x z_{\mathrm{op}} + b_x, \\ y_{\mathrm{op}} &= s_y z_{\mathrm{op}} + b_y. \end{aligned}$$

b_x and b_y can be determined as follows:

$$\begin{aligned} x_{\mathrm{op},0} = s_x z_{\mathrm{op},0} + b_x \Rightarrow b_x = x_{\mathrm{op},0} - s_x z_{\mathrm{op},0} \quad &\Leftrightarrow x_{\mathrm{op}} = s_x z_{\mathrm{op}} + x_{\mathrm{op},0} - s_x z_{\mathrm{op},0}, \\ y_{\mathrm{op},0} = s_y z_{\mathrm{op},0} + b_y \Rightarrow b_y = y_{\mathrm{op},0} - s_y z_{\mathrm{op},0} \quad &\Leftrightarrow y_{\mathrm{op}} = s_y z_{\mathrm{op}} + y_{\mathrm{op},0} - s_y z_{\mathrm{op},0}. \end{aligned}$$

Applying the coordinate transformation, one gets

$$\begin{aligned} \Delta y - y = s_x(\Delta x - x) + x_{\mathrm{op},0} - s_x z_{\mathrm{op},0} \Rightarrow y = s_x x - s_x \Delta x - x_{\mathrm{op},0} + s_x z_{\mathrm{op},0} + \Delta y, \\ -\Delta z + z = s_y(\Delta x - x) + y_{\mathrm{op},0} - s_y z_{\mathrm{op},0} \Rightarrow z = -s_y x + s_y \Delta x + y_{\mathrm{op},0} - s_y z_{\mathrm{op},0} + \Delta z. \end{aligned}$$

In Borexino, the track parametrization

$$\begin{aligned} y &= \alpha + \beta x, \\ z &= \gamma + \delta y \end{aligned}$$

is used. Comparing the parameters leads to

$$\begin{aligned} \alpha &= -s_x \Delta x - x_{\mathrm{op},0} + s_x z_{\mathrm{op},0} + \Delta y, \\ \beta &= s_x, \\ \gamma &= s_y \Delta x + y_{\mathrm{op},0} - s_y z_{\mathrm{op},0} + \Delta z, \\ \delta &= -s_y. \end{aligned}$$

For an easy comparison of tracks, the polar and azimuth angles θ and φ are used. They can easily be obtained:

$$\begin{aligned} \varphi &= \tan^{-1}(\beta), \\ \theta &= \tan^{-1}\left(\frac{1}{\delta \cos\varphi}\right). \end{aligned}$$

One can assume that muons originating from the CNGS beam have a direction close to the beam axis. Using the definition above, the azimuth angle φ can obtain values between $-\frac{\pi}{2}$ and $\frac{\pi}{2}$ which is the angle in the horizontal plane towards the beam direction. For the polar angle, values between 0 and π are realistic. Therefore, θ has to be corrected by π for negative values:

$$\theta = \begin{cases} \tan^{-1}\left(\frac{1}{\delta \cos\varphi}\right) & \text{for } \tan^{-1}\left(\frac{1}{\delta \cos\varphi}\right) \geq 0 \\ \tan^{-1}\left(\frac{1}{\delta \cos\varphi}\right) + \pi & \text{for } \tan^{-1}\left(\frac{1}{\delta \cos\varphi}\right) < 0 \end{cases}$$

Appendix E

Noise Patterns

This appendix gives a short overview of the most common noise events in the CMT. Noise events do not occur very often and most of them can be effectively suppressed by a simple cut on the number of hits. Fig. E.1 shows an event where all active tubes have fired. The signal widths are all either medium or small. Events with 48 hits per module are discarded, so this kind is ignored.

A more dangerous effect occurred for a period of a few days during RUN_243_11-23-20[1]. Similar noise patters where most of the outer right tubes showed a signal would occur approximately one an hour. A typical event is depicted in Fig. E.2. These events cannot be filtered by a cut on the number of events. Also, the hits are all in one column which is likely to mimic a real track. These events can be identified again by the small and medium signal widths. However, a cut on the signal width is not performed to prevent true hits with non large signal width from being removed from the data. With a good calibration, these events are rejected by the fit and are therefore of no threat.

[1] This is already indicated by the large number of events despite the short duration of the run.

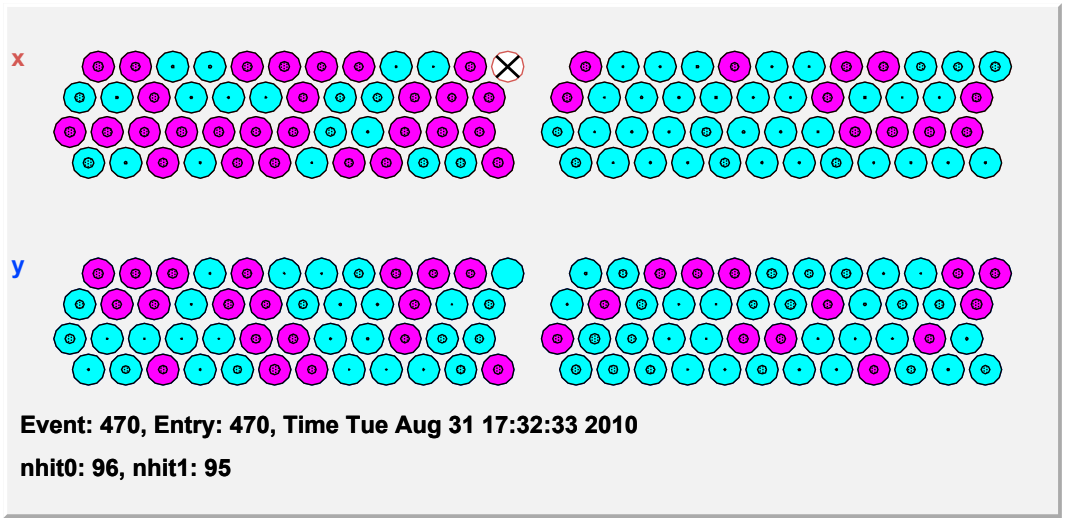

Figure E.1: A typical noise event where all tubes show a signal. The colors indicate the signal width: pink for medium and turquoise for small widths.

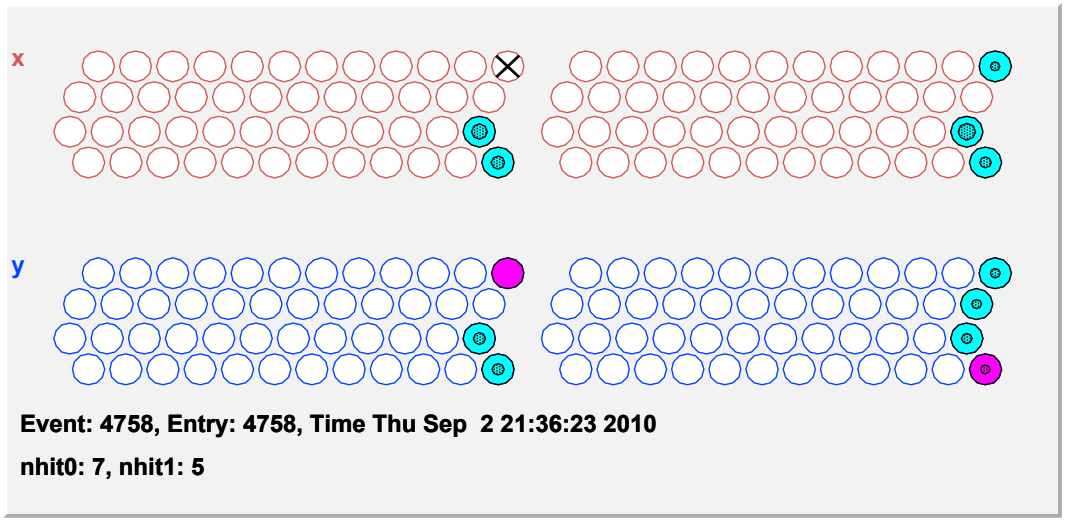

Figure E.2: A typical noise event of RUN_243_11-23-20 where tubes on the right show a signal. The colors indicate the signal width: pink for medium and turquoise for small widths.

Bibliography

[1] W. Pauli. Dear radioactive ladies and gentlemen. *Phys. Today*, 31N9:27, 1978.

[2] Frederick Reines and Clyde L. Cowan. The neutrino. *Nature*, 178:446–449, 1956.

[3] G. Danby et al. Observation of High-Energy Neutrino Reactions and the Existence of Two Kinds of Neutrinos. *Phys. Rev. Lett.*, 9:36–44, 1962.

[4] Martin L. Perl. The New Particles Produced in electron-Positron Annihilation. Presented at Symposium on New Directions in Hadron Spectroscopy, Argonne National Lab., Ill., Jul 7-10, 1975.

[5] R. Rameika. The DONUT experiment: First direct evidence of nu/tau. Prepared for 28th SLAC Summer Institute on Particle Physics: Neutrinos from the Lab, the Sun, and the Cosmos (SSI 2000), Stanford, California, 14-25 Aug 2000.

[6] Precision electroweak measurements on the Z resonance. *Phys. Rept.*, 427:257, `arXiv:hep-ex/0509008`.

[7] Raymond Davis, Jr., Don S. Harmer, and Kenneth C. Hoffman. Search for neutrinos from the sun. *Phys. Rev. Lett.*, 20:1205–1209, 1968.

[8] P. Anselmann et al. Solar neutrinos observed by GALLEX at Gran Sasso. *Phys. Lett.*, B285:376–389, 1992.

[9] M. Altmann et al. Complete results for five years of GNO solar neutrino observations. *Phys. Lett.*, B616:174–190, `arXiv:hep-ex/0504037`.

[10] A. I. Abazov et al. Search for neutrinos from sun using the reaction Ga-71 (electron-neutrino e-) Ge-71. *Phys. Rev. Lett.*, 67:3332–3335, 1991.

[11] K. S. Hirata et al. Observation of B-8 Solar Neutrinos in the Kamiokande-II Detector. *Phys. Rev. Lett.*, 63:16, 1989.

[12] Y. Fukuda et al. Evidence for oscillation of atmospheric neutrinos. *Phys. Rev. Lett.*, 81:1562–1567, `arXiv:hep-ex/9807003`.

[13] Q. R. Ahmad et al. Measurement of the charged current interactions produced by B-8 solar neutrinos at the Sudbury Neutrino Observatory. *Phys. Rev. Lett.*, 87:071301, `arXiv:nucl-ex/0106015`.

[14] Ch. Kraus et al. Final Results from phase II of the Mainz Neutrino Mass Search in Tritium β Decay. *Eur. Phys. J.*, C40:447–468, arXiv:hep-ex/0412056.

[15] V. M. Lobashev et al. Direct search for neutrino mass and anomaly in the tritium beta-spectrum: Status of 'Troitsk neutrino mass' experiment. *Nucl. Phys. Proc. Suppl.*, 91:280–286, 2001.

[16] A. Osipowicz et al. KATRIN: A next generation tritium beta decay experiment with sub-eV sensitivity for the electron neutrino mass. arXiv:hep-ex/0109033.

[17] Ettore Majorana. Theory of the Symmetry of Electrons and Positrons. *Nuovo Cim.*, 14:171–184, 1937.

[18] Stefan. Schönert et al. The GERmanium Detector Array (GERDA) for the search of neutrinoless beta beta decays of Ge-76 at LNGS. *Nucl. Phys. Proc. Suppl.*, 145:242–245, 2005.

[19] C. Arnaboldi et al. CUORE: A cryogenic underground observatory for rare events. *Nucl. Instrum. Meth.*, A518:775–798, arXiv:hep-ex/0212053.

[20] R. Arnold et al. Technical design and performance of the NEMO 3 detector. *Nucl. Instrum. Meth.*, A536:79–122, arXiv:physics/0402115.

[21] B. Pontecorvo. Mesonium and antimesonium. *Sov. Phys. JETP*, 6:429, 1957.

[22] B. Pontecorvo. Neutrino experiments and the question of leptonic-charge conservation. *Sov. Phys. JETP*, 26:984–988, 1968.

[23] Ziro Maki, Masami Nakagawa, and Shoichi Sakata. Remarks on the unified model of elementary particles. *Prog. Theor. Phys.*, 28:870–880, 1962.

[24] Y. Ashie et al. A Measurement of Atmospheric Neutrino Oscillation Parameters by Super-Kamiokande I. *Phys. Rev.*, D71:112005, arXiv:hep-ex/0501064.

[25] P. Adamson et al. Measurement of Neutrino Oscillations with the MINOS Detectors in the NuMI Beam. *Phys. Rev. Lett.*, 101:131802, arXiv:0806.2237.

[26] M. Ambrosio et al. Measurements of atmospheric muon neutrino oscillations, global analysis of the data collected with MACRO detector. *Eur. Phys. J.*, C36:323–339, 2004.

[27] M. H. Ahn et al. Measurement of Neutrino Oscillation by the K2K Experiment. *Phys. Rev.*, D74:072003, arXiv:hep-ex/0606032.

[28] J. Hosaka et al. Three flavor neutrino oscillation analysis of atmospheric neutrinos in Super-Kamiokande. *Phys. Rev.*, D74:032002, arXiv:hep-ex/0604011.

[29] B. Aharmim et al. Low Energy Threshold Analysis of the Phase I and Phase II Data Sets of the Sudbury Neutrino Observatory. *Phys. Rev.*, C81:055504, arXiv:0910.2984.

[30] S. Abe et al. Precision Measurement of Neutrino Oscillation Parameters with KamLAND. *Phys. Rev. Lett.*, 100:221803, arXiv:0801.4589.

[31] J. Hosaka et al. Solar neutrino measurements in Super-Kamiokande-I. *Phys. Rev.*, D73:112001, arXiv:hep-ex/0508053.

[32] M. Apollonio et al. Limits on Neutrino Oscillations from the CHOOZ Experiment. *Phys. Lett.*, B466:415–430, arXiv:hep-ex/9907037.

[33] K Nakamura et al. Review of particle physics. *J. Phys.*, G37:075021, 2010.

[34] L. Wolfenstein. Neutrino oscillations in matter. *Phys. Rev.*, D17:2369–2374, 1978.

[35] Boris Kayser. Neutrino physics. arXiv:hep-ph/0506165.

[36] Esteban Roulet. Mikheyev-Smirnov-Wolfenstein effect with flavor-changing neutrino nteractions. *Phys. Rev.*, D44:935–938, 1991.

[37] Vernon D. Barger, R. J. N. Phillips, and K. Whisnant. Solar neutrino solutions with matter enhanced flavor changing neutral current scattering. *Phys. Rev.*, D44:1629–1643, 1991.

[38] V. Barger, Patrick Huber, and Danny Marfatia. Solar mass-varying neutrino oscillations. *Phys. Rev. Lett.*, 95:211802, arXiv:hep-ph/0502196.

[39] Alexander Friedland, Cecilia Lunardini, and Carlos Pena-Garay. Solar neutrinos as probes of neutrino - matter interactions. *Phys. Lett.*, B594:347, arXiv:hep-ph/0402266.

[40] H. A. Bethe. Energy production in stars. *Phys. Rev.*, 55:434–456, 1939.

[41] Carlos Pena-Garay and Aldo Serenelli. Solar neutrinos and the solar composition problem. arXiv:0811.2424.

[42] John N. Bahcall. Solar neutrinos. I: Theoretical. *Phys. Rev. Lett.*, 12:300–302, 1964.

[43] John N. Bahcall, Aldo M. Serenelli, and Sarbani Basu. New solar opacities, abundances, helioseismology, and neutrino fluxes. *Astrophys. J.*, 621:L85–L88, arXiv:astro-ph/0412440.

[44] Cristiano Galbiati. 192 days of borexino. In *Presented at the Neutrino 2008 conference in Christchurch, New Zeland*, 2008.

[45] E. Aslanides et al. A deep sea telescope for high energy neutrinos. arXiv:astro-ph/9907432.

[46] J. Ahrens et al. IceCube: The next generation neutrino telescope at the South Pole. *Nucl. Phys. Proc. Suppl.*, 118:388–395, arXiv:astro-ph/0209556.

[47] Gernot Eder. Terrestrial neutrinos. *Nuclear Physics*, 78(3):657 – 662, 1966.

[48] G. Marx. Geophysics by neutrinos. *Czechoslovak Journal of Physics*, 19:1471–1479, 1969. 10.1007/BF01698889.

[49] T. Araki et al. Experimental investigation of geologically produced antineutrinos with KamLAND. *Nature*, 436:499–503, 2005.

[50] G. Bellini et al. Observation of Geo-Neutrinos. *Phys. Lett.*, B687:299–304, arXiv:1003.0284.

[51] Gianni Fiorentini, Marcello Lissia, and Fabio Mantovani. Geo-neutrinos and Earth's interior. *Phys. Rept.*, 453:117–172, arXiv:0707.3203.

[52] F. Ardellier et al. Letter of intent for double-CHOOZ: A search for the mixing angle theta(13). arXiv:hep-ex/0405032.

[53] Edda Gschwendtner. CERN neutrinos to Gran Sasso (CNGS): First beam. Prepared for 2006 IEEE Nuclear Science Symposium (NSS), Medical Imaging Conference (MIC) and 15th International Room Temperature Semiconductor Detector Workshop, San Diego, California, 29 Oct - 4 Nov 2006.

[54] D. Drakoulakos et al. Proposal to perform a high-statistics neutrino scattering experiment using a fine-grained detector in the NuMI beam. arXiv:hep-ex/0405002.

[55] Y. Itow et al. The JHF-Kamioka neutrino project. arXiv:hep-ex/0106019.

[56] Claude Amsler et al. Review of particle physics. *Phys. Lett.*, B667:1, 2008.

[57] F. Sauli. Principles of Operation of Multiwire Proportional and Drift Chambers. CERN-77-09.

[58] R. Zimmermann et al. The precision tracker of the OPERA detector. *Nucl. Instrum. Meth.*, A555:435–450, 2005.

[59] P. Reviersma. The l3 wire - amplifier. 1986. NH19-6112.

[60] R. van Staa J. Schütt. *OSUB OPERA Supportboard*. Universität Hamburg, Institut für Experimentalphysik, February 2006.

[61] R. van Staa J. Schütt. *OTB OPERA Triggerboard*. Universität Hamburg, Institut für Experimentalphysik, March 2006.

[62] Klaus Hitschler Peak System-Technik GmbH. *PCAN-driver for Linux*, 2007.

[63] MSC Vertriebs GmbH. *Benutzerhandbuch DES OPERA*, 2004. in German.

[64] C. Girerd. *OPERA TDC controller board Test Acquisition Tools Getting started Manual*, 2006.

[65] I.N. Bronstein, K.A. Semendjajew, G. Musiol, and H. Mühlig. *Taschenbuch der Mathematik*. Verlag Harry Deutsch, Thun und Frankfurt am Main, 5 edition, 2001.

[66] R. K. Bock, (Ed.), K. Bos, (Ed.), S. Brandt, (Ed.), J. Myrheim, (Ed.), and M. Regler, (Ed.). FORMULAE AND METHODS IN EXPERIMENTAL DATA EVALUATION WITH EMPHASIS ON HIGH-ENERGY PHYSICS. VOL. 3: ARTICLES ON STATISTICAL AND NUMERICAL METHODS. Petit Lancy, Switzerland: Eps (1984) Nonconsec. Pag.

[67] C. Arpesella et al. First real time detection of Be7 solar neutrinos by Borexino. *Phys. Lett.*, B658:101–108, arXiv:0708.2251.

[68] G. Alimonti et al. The Borexino detector at the Laboratori Nazionali del Gran Sasso. *Nucl. Instrum. Meth.*, A600:568–593, arXiv:0806.2400.

[69] C. Arpesella et al. Direct Measurement of the Be-7 Solar Neutrino Flux with 192 Days of Borexino Data. *Phys. Rev. Lett.*, 101:091302, arXiv:0805.3843.

[70] M. Wurm. *Cosmic Background Discrimination for Rare Neutrino Event Search in Borexino and LENA*. PhD thesis, TU München, 2009.

[71] G. Bellini et al. Muon and Cosmogenic Neutron Detection in Borexino. 2011.

[72] Cristiano Galbiati et al. Cosmogenic C-11 production and sensitivity of organic scintillator detectors to pep and CNO neutrinos. *Phys. Rev.*, C71:055805, arXiv:hep-ph/0411002.

[73] M. Pallavicini and for the Borexino Collaboration. Solar neutrino results from Borexino and main future perspectives. arXiv:0910.3367.

[74] B. Aharmim et al. Measurement of the nu/e and total B-8 solar neutrino fluxes with the Sudbury Neutrino Observatory phase I data set. *Phys. Rev.*, C75:045502, arXiv:nucl-ex/0610020.

[75] G. Bellini et al. Measurement of the solar 8B neutrino rate with a liquid scintillator target and 3 MeV energy threshold in the Borexino detector. *Phys. Rev.*, D82:033006, arXiv:0808.2868.

[76] Antonio Palazzo. Hint of non-standard MSW dynamics in solar neutrino conversion. arXiv:1101.3875.

[77] S. P. Ahlen et al. Study of penetrating cosmic ray muons and search for large scale anisotropies at the Gran Sasso Laboratory. *Phys. Lett.*, B249:149–156, 1990.

[78] Borexino Coll. *Echidna Documentation*.

[79] R. Acquafredda et al. The OPERA experiment in the CERN to Gran Sasso neutrino beam. *JINST*, 4:P04018, 2009.

[80] M. Guler et al. OPERA: An appearance experiment to search for $\nu_\mu \leftrightarrow \nu_\tau$ oscillations in the CNGS beam. Experimental proposal. CERN-SPSC-2000-028.

Danksagung

Ich bedanke mich bei allen Menschen, die mich bei der Anfertigung dieser Arbeit unterstützt haben.

Besonderer Dank gilt Caren Hagner für die Möglichkeit, diese Doktorarbeit anzufertigen. Ihre Begeisterung für die Neutrinophysik war stets ermutigend und inspirierend. Die Mitarbeit in ihrer Forschungsgruppe ist ein ganz besonders großes Vergnügen.

Weiterer Dank gebührt Walter Schmidt-Parzefall, für die wertvollen Diskussionen und die vielen Hinweise zu dieser Arbeit und zu den generellen Methoden der Teilchenphysik.

Ein großer Dank gilt auch allen weiteren Hamburger Kollegen der Forschungsgruppe Neutrinophysik. In den letzten Jahren haben wir viel Zeit zusammen verbracht, nicht nur im Büro sondern auch privat. Die vielen Reisen nach Italien werden mir in guter Erinnerung bleiben (Mmh... lecker Pizza/Arrosticini/Tiramisu/etc.!). Rückblickend auf die letzten Jahre fallen mir viele denkwürdige Begebenheiten ein, die hier nicht alle erwähnt werden können. Um nur ein paar zu nennen, bedanke ich mich bei Joachim Ebert für seine Konstruktionsarbeiten, sowie fürs Erledigen aller Verwaltungsangelegenheiten, bei Björn Wonsak für all die Dokumentationen, mit denen er uns die Welt erklärt hat, bei Christoph „Klaus“ Göllnitz für ein immer offenes Ohr (nicht nur beim Feierabendbier), viele Weihnachtsüberraschungen und unsere *gemeinsame* Zeit in Erice, bei Torben Ferber für die Hilfe mit den Rock-Myonen, bei Martin Hierholzer für die gemeinsame Zeit im Büro, bei Jan Lenkeit für die vielen Plaudereien und unsere Vulkanreisen, bei Christian „Ernie“ Oldorf und Nadine Heidrich für die Teestunden und Schokolade, bei Annika Hollnagel für die reibungslose Versorgung mit Vitaminen und Bällen, bei Jan „Horsti“ Timm für das Ausleihen des ADCs samt Messschaltung und bei Hans-Jürgen Ohmacht fürs Montieren und Installieren. Nicht vergessen werden dürfen an dieser Stelle unsere $\boldsymbol{\nu}$-Kekse (die genauso aussehen, wie hier gedruckt!), welche Ernie, Jan und Klaus die letzten zwei Jahre mit mir gebacken haben! Ein Dank für die schöne Zeit geht natürlich auch an alle Diplomanden und sonstige Studenten, die mir im Laufe der Zeit hier über den Weg gelaufen sind.
Hervorheben möchte ich unsere ehemaligen Mitarbeiter Ole Roß und Benjamin Janutta, ohne deren Lockversuche mit Chicken Wings ich vielleicht gar nicht in dieser Gruppe gelandet wäre.
Für die vielen hilfreichen Korrekturen und Kommentare zu dieser Arbeit danke ich

Jan Lenkeit und Björn Wonsak sowie Björn Opitz.
Michael Wurm danke ich für die nette Zusammenarbeit bei unserer gemeinsamen Analyse und die freundliche Herberge in München. Ihm und Timo Lewke gilt weiterer Dank dafür mir beizubringen, wie man eine Borexino Schicht erfolgreich bewerkstelligt.
Ich danke der DFG, die meine Arbeit und mich im Rahmen des SFB 676 *Particles, Strings, and the Early Universe* die letzten Jahre finanziert hat.

Ich möchte all meinen Freunden danken, die mich nicht vergessen haben, obwohl ich mich die letzten Monate kaum bei ihnen gemeldet habe. Insbesondere sind jene zu erwähnen, die mich über weite Strecken meines Studiums begleitet haben:
Erik Butz, u.a. für französische Gastfreundschaft, die CERN Besichtigung, Whisky-Abende, die Querung des Furkapasses und alle unsere anderen Radtouren.
Herr Björn Opitz, u.a. für die vielen Ausflüge mit James Bond und Steve Zissou, die netten Abende bei uns, bei euch oder irgendwo dazwischen und alle unsere Nordseestrandtouren.
Maik Brachmann, u.a. für die Autofahrt nach Lappland, die vielen Kinobesuche und alle unsere Kneipentouren.

Meinen Eltern danke ich für ihre uneingeschränkte Unterstützung. Ohne sie wäre diese Arbeit nicht möglich gewesen.

Ich danke Susanne für ihr Verständnis, ihre Unterstützung, Geduld und Liebe.